Spin-Orbit Torques and Galvanomagnetic Effects Generated by the 3D Topological Insulator HgTe

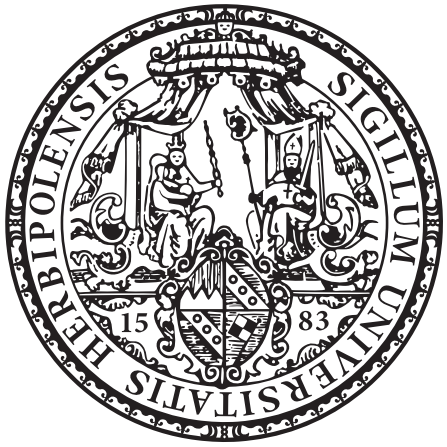

Dissertation zur Erlangung des naturwissenschaftlichen Doktorgrades der Julius-Maximilians-Universität Würzburg

vorgelegt von

Graciely Elias dos Santos

aus Curitiba / Brasilien

Würzburg, 2020

Eingereicht am: .....
bei der Fakultät für Physik und Astronomie

1. Gutachter: Prof. Dr. Laurens W. Molenkamp
2. Gutachter: Prof. Dr. Friedrich Reinert
3. Gutachter: .....
der Dissertation

Vorsitzende(r): .....

1. Prüfer: Prof. Dr. Laurens W. Molenkamp
2. Prüfer: Prof. Dr. Friedrich Reinert
3. Prüfer: Prof. Dr. Björn Trauzettel
im Promotionskolloquium

Tag des Promotionskolloquiums: .....

Doktorurkunde ausgehändigt am: .....

Para minha família

Keep Ithaca always in your mind.
Arriving there is what you are destined for.
But don't hurry the journey at all.
Better if it lasts for years,
So you're old by the time you reach the island,
Wealthy with all you have gained on the way
And not expecting Ithaca to make you rich.

Ithaca gave you the beautiful journey.
Without her you'd never have set out.
She has nothing more to give you now.
And if you find her poor, Ithaca won't have deceived you.
Wise as you have become, after so much experience,
You'll have understood by then what these Ithacas mean.

Constantine P. Cavafy

Contents

1

Introduction

"There is plenty of room at the bottom"

Richard Feynman

1.1. Background: a brief section for parents

In the past few years, humanity has witnessed a series of technological advances, from powerful electronic devices to self-driven cars. Computers, tablets, and smartphones are becoming smaller and performing better, thus, changing drastically the way we work and live. Such progress is due to a series of advances made in several fields, such as materials science, physics, chemistry, engineering and new hot topics such as machine learning and artificial intelligence [1]. The heart of every electronic device is the transistor, which allows data to be generated, manipulated and detected in a series of "on" and "off" electronic signals, i.e., a representation of the bits "0" and "1".

While the first processor introduced by Intel in 1971 contained only 2300 transistors, modern processors can exceed a few dozen billion transistors [2]. On the one hand, downscaling the size of transistors brings several advantages, e.g., increasing computing efficiency and storage capacity due to the density of the high transistors. On the other hand, downscaling transistors also lead to high current densities, heat dissipation, gate leakages and, therefore, decrease the

1

device's performance. The biggest challenge of the semiconductor industry is to find a compromise between achieving higher performances and accommodate the limitations of downscaling such devices. Finding new materials, techniques and technologies to enable the efficient downscaling of the transistor is currently a hot topic in both industrial and academic environments. It is also the long-term goal of the investigations I performed in this thesis.

1.2. From spintronics...

The majority of today's modern devices still use the electron charge to store and transport information. However, each electron also possesses a small magnetic moment, the spin, which is a quantum mechanical property. The field of spintronics, which takes advantage of both the charge and the spin of an electron, is considered a promising avenue for successful generation, manipulation and detection of electric signals in modern devices [3]. Spin-based electronic building-blocks are expected to operate faster and dissipate less heat when compared to conventional charge-based electronic devices. One of the most important discoveries in the field of spintronics was undoubtfully the discovery of the giant magnetoresistance (GMR) effect by Peter Grünberg [4] and Albert Fert [5] in 1988, which rendered them the Physics Nobel prize in 2007. The GMR effect is realized in a device known as a spin-valve, consisting of two ferromagnetic layers (FM) separated by a normal layer (NM). The magnetoresistance of such a device depends on the relative angle of the magnetization $\vec{M}$ between the magnetic layers. When the two ferromagnets are parallel (P) to each other, the spin-valve exhibits a lower resistance in comparison when the two ferromagnetic layers are aligned anti-parallel (AP) to each other. The different resistances for the AP and P states rely on the fact that spin-polarized electrons have different scattering rates inside the ferromagnets and at the FM/NM interface and, if the conduction electrons have the same spin orientation as the ferromagnet, the electrons will experience less scattering.

A similar change in the magnetoresistance can also be observed if the normal layer between the two ferromagnets is a thin insulator, in a device geometry known as magnetic tunnel junction (MTJ). The change in the resistance in the MTJ is called tunneling magnetoresistance (TMR) [6, 7]. The electron transport across the tunnel barrier happens in the tunneling regime and the tunneling probability is proportional to the density of states (DoS) of both ferromagnets, which is spin-dependent. Thus, the electrons have different tunneling probabilities for P and AP states, leading to a change in resistance. The TMR is usually higher than the GMR effect and it can reach hundreds of percent [8]. This high change of resistance allows for better sensitivity allowing the utilization of magnetic tunnel junctions as reading head of hard drive disks [9].

In 1996 Slonczewski [10] and Berger [11] predicted the existence of the spin-transfer torque (STT), where the flux of angular momentum, known as a spin current, can be transferred from

one ferromagnetic layer to another and exert a torque on the magnetization. This spin torque can lead to magnetization precession [12] and even switching of the magnetization of the FM layer [13]. This effect is schematically depicted in Fig. 1.1a for a MTJ device. The yellow color represents the electrical contacts and blue and red represent the reference and recording ferromagnetic layers, respectively. The recording and reference layers are separated by a spacer, depicted in black. The initial magnetization of both layers is controlled by an external magnetic field. In Fig. 1.1a, one of the ferromagnetic layers (reference layer) of the MTJ or GMR device is used as a spin polarizer, thus generating the spin current (depicted in grey and flowing from top to bottom contacts). Then, STT provides a mechanism to "write" information in the recording layer, i.e., by rotating its magnetization from, e.g., 0 (original orientation) to 180 degrees (final orientation). In the snapshot shown in Fig. 1.1a, the magnetization is about 2/3 of the way to being switched (see the red and purple big arrows in the recording layer). In terms of functionality, one could consider the magnetization oriented, say, at 0 degrees as the bit 0, while the magnetization at 180 degrees would be the bit 1. Finally, the information - here, if both recording and reference layers are AP or P to each other - can be "read" by measuring the device's resistance via the TMR or GMR effect.

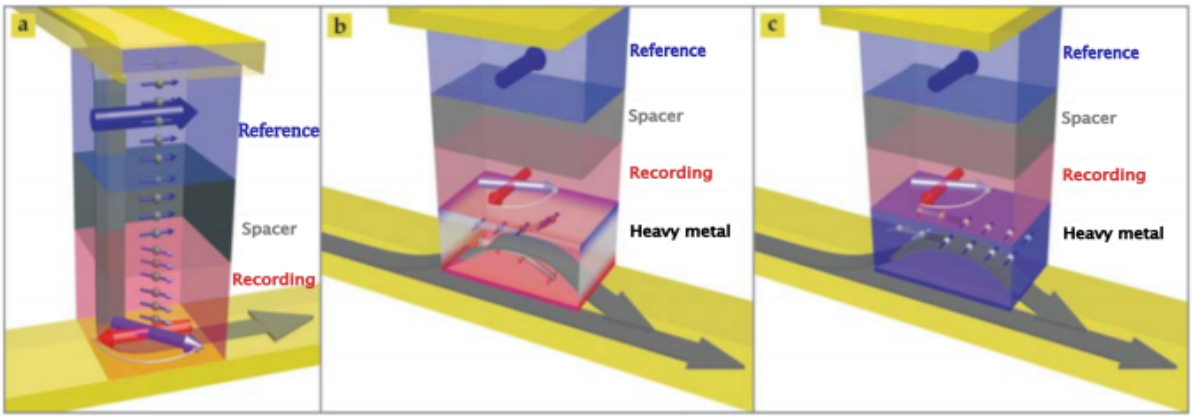

Figure 1.1: Schematic representations of STT and spin-orbit torque. Here, yellow represents the electrical contacts and blue and red represent the reference and recording layers, respectively. (a) In the STT case, a current of spin-polarized electrons (grey arrow) flows from the reference ferromagnet through the spacer layer into the recording ferromagnetic layer. Inside the recording magnet, the flowing electrons' spin aligns with the magnetization (large purple arrow in the recording layer). This alignment results in a torque on the recording ferromagnet that causes the magnetization to switch from its original orientation (large red arrow). For the SOT mechanism, which can be driven either by the SHE or iSGE, b) shows the SHE version. As current flows along the contact and the nonmagnetic metal layer, a spin current is generated which then flows into the recording ferromagnet and switches its magnetization. c) In the iSGE version, electrons become spin-polarized at the interface of a nonmagnetic metal and the recording ferromagnet, thus switch its magnetization via exchange coupling. Figure taken from reference [14]

STTs in MTJs have been used to develop non-volatile random access memories (MRAM) [15] and the magnetic domain wall racetrack memory [16]. These MRAMs are produced on an industrial scale and are easily embedded in CMOS technology. Although such devices offer numerous possibilities of technological applications, the information transfer and processing in

such architectures still rely on electrons carrying spin information. In this case, sharing the read and write current paths in STT-MRAMs require high writing currents, which is not energy efficient and cause reliability issues due to barrier (insulating material) damage. Moreover, optimization of the spin polarization across the MTJ and stabilization of the reference layer magnetization results in complex stacking structures involving more than 10 different layers [17]. Additionally, one of the major drawbacks of the STT scheme is the requirement of an additional magnet to create spin-polarized currents.

1.3. ... to spin-orbitronics

In 2009, a promising alternative to spin-transfer torque emerged. This effect, named spin-orbit torque (SOT), arises due to the flow of an electric current in a material system lacking inversion symmetry, leading to the transfer of orbital angular momentum from the lattice to the spin system via spin-orbit (SOC) and exchange coupling [17–21]. This effect also involves the manipulation of charge and spin, however, this spin torque is fundamentally different from the STT, because the spin polarizer (reference layer) is no longer a ferromagnet, but a material with strong SO coupling.

Take as an example the device shown in Fig. 1.1b. The configuration of the reference and recording layers is the same as described in Fig. 1.1a, however, now, a heavy metal layer was added below the recording layer and the current no longer flows vertically, but rather parallel to the device layers (grey arrows). SOTs can be driven either by the spin Hall (SHE) or the inverse spin galvanic (iSGE) effect.

In the example depicted in Fig. 1.1b, spin-orbit torques are generated via the spin Hall effect, which has its origin on the asymmetric spin scattering in the bulk of a non-magnetic metal with strong spin-orbit coupling [22, 23]. In this case, a pure spin current is generated in the heavy metal (such as Pt or Ta), and its orientation is transverse to the direction of the applied electrical current, as schematically depicted in Fig. 1.1b. This spin current can be absorbed by the magnetization of the adjacent ferromagnet (recording layer) and exert a torque on it. Then, the information can be, again, read by the TMR or GMR effects. The spin accumulation generated by the SHE proved to be extremely efficient to trigger ferromagnetic resonance (FMR) precession [24, 25] and, at large currents, it can fully switch the magnetization of a ferromagnet [26, 27].

Using SOC to generate and manipulate the spin degree of freedom of paramagnetic materials led to the baptism of a field inside the spintronics community: the spin-orbitronics. The main advantage of SOT over STT is that the electrical current does not flow through the whole device structure. Moreover, since the spin polarization generated in the reference layer is coupled to the current direction, the reference magnetization can be engineered to be misaligned with the

recording magnetization. This approach allows not only to decouple the write and read current paths (thus, improving the endurance of the device), but also allows faster torques [28, 29].

Spin-polarized currents can also be generated in systems lacking an inversion symmetry center. In this case, the flow of charge current parallel to such an interface gives rise to a non-equilibrium spin density, whose angular momentum can be transferred to the magnetization of an adjacent magnetic layer (similarly to the case depicted in Fig. 1.1b), thus exerting a torque on its magnetization [18]. The mechanism of generating spin densities via charge currents is known as Rashba-Edelstein effect [30] or inverse spin galvanic effect (iSGE) [31] and in this thesis, both terms will be used interchangeably.

The figure of merit of SHE-based SOT devices is the so-called *charge-to-spin* conversion efficiency (spin Hall angle), which assesses how much of the charge current is converted into angular momentum. In order to achieve efficient magnetization manipulation, one of the key challenges for the progress of this field is to identify materials that exhibit large spin-orbit torque efficiencies.

The discovery of topological insulators about 13 years ago was not only an important event in the field of condensed matter physics, but also in the spintronics field [32, 33]. Three-dimensional topological insulators (3D TI) are a class of materials that have an energy bandgap like a normal insulator, but also have conducting/gapless surface states resulting from the inversion of the conduction and valence bands due to strong SOC [32–34]. These surface states show a linear energy dispersion (sketched in Fig. 1.2a), which can be described by a time-reversal invariant Dirac Hamiltonian. An important consequence of the time-reversal invariance of the Hamiltonian is the topological protection of the so-called topological surface states (TSS): as, it can be seen in Fig. 1.2b, the spin and the momentum of the carriers in the TSS are coupled perpendicularly to each other (spin-momentum locking), meaning that, similarly to the SHE, the direction of the carrier's motion uniquely determines its spin direction and vice-versa [33–36].

In 2008, the experimental discovery of 3D topological insulators in $Bi_{1-x}Sb_x$ [37] rose this class of materials as good candidates for electrical generation of spin-polarized currents. When an electrical current flows through the TSS, due to the rigid locking between momentum and spin, an imbalance of carriers also leads to an imbalance of spins, i.e., to the generation of a spin-polarized current via iSGE [30, 38]. What makes the spin current generated by topological insulators special is that the robustness of the spin-momentum locking against impurity scattering enables metallic transport without significant spin relaxation or, in other words, the spin information is maintained even after a large number of scattering events [14, 38].

The exotic properties of topological insulators led to several theoretical predictions on how to take advantage of this robust spin-polarized current to manipulate the magnetization of ferromagnets [3, 38, 40] and build electronic devices based on them. In 2014, it was shown that Bi_2Se_3 is very efficient to generate spin-orbit torques in adjacent ferromagnets [41]. From the physics point of

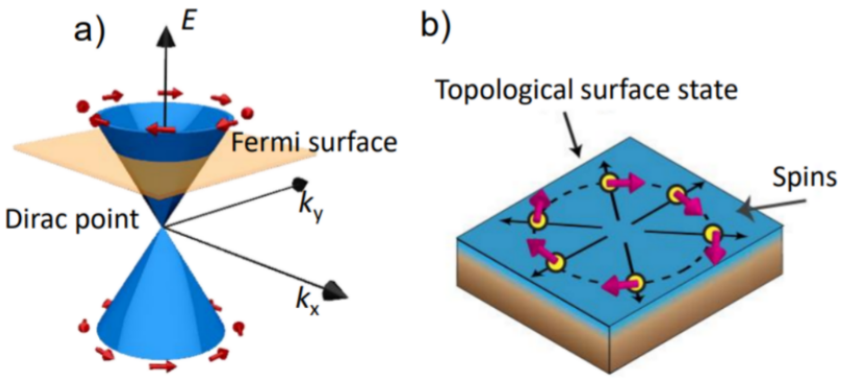

Figure 1.2: a) Schematics of Dirac cone of the TSS, where the Dirac point and spin-momentum locking in momentum space is shown. b) Illustration of the spin-momentum locking of the carriers in the TSS in real space. Figure taken from [39]

view, since the spin-polarized current is generated on the surface of the TI, angular information is transferred via exchange interaction: from the itinerant carrier spins to the localized magnetic moments of the ferromagnet, as schematically depicted in Fig. 1.1c.

Although the vast majority of 3D TIs are part of the Bi-family and several efforts have been made in growing different alloys, e.g., BiSbTeSe [42, 43], these systems are yet not ideal topological insulators because the bulk of these materials is not fully insulating. Thus, the exotic electrical properties that are supposed to emerge from the topological surface states are polluted by parallel bulk conductivity and, therefore, this contribution decreases the efficiencies generation of spin currents in topological insulators. However, in 2011 it was first demonstrated that tensile strained 3D HgTe is a 3D topological insulator [44]. In these systems, magnetoelectrical transport is dominated by the topological surface states [45] and insights about their topological nature were provided by proximitizing 3D TI HgTe with superconductors [46]. These investigations make the 3D TI HgTe a promising, if not an ideal, candidate to explore the effect of the topological properties in the generation of spin-torques in ferromagnetic materials.

Several attempts to demonstrate spin-orbit torques generated by Bi-based topological insulators were reported in the literature (see Fig. 3.17 in Chap. 3 for a graphic overview). However, the contradiction in some of these results, combined with experimental techniques that do not allow for a direct assessment of how efficiently a topological insulator material system can generate spin-transfer torques, leaves open questions that this thesis aims to carefully answer.

1.4. This thesis

The utmost purpose of this Ph.D. thesis is to experimentally assess the suitability of the 3D TI HgTe system for spintronics applications. Moreover, since spin-torque experiments involve the application of electrical currents and in-plane magnetic fields in the 3D TI HgTe, this thesis also aims to carefully understand how the magnetoresistance response of this material system is affected by the application of magnetic fields in its plane. The outline of this thesis is organized as follows:

chapter 2 introduces the spin-orbit coupling and its consequences to semiconductors. The chapter also introduces the concept of topological insulators, the band structure of HgTe and how the topological insulator phase can be realized and characterized experimentally. The second part of the chapter provides a brief review of the characterization of ferromagnetic materials and the basic concepts of spin-transfer torques. **Chapter 3** presents the mathematical description of spin-orbit torques, along with the figures of merit to address the eligibility of the 3D TI HgTe to generate torques in an adjacent ferromagnet. Additionally, the device fabrication and experimental setup is described in detail, along with a discussion and critical review of the experimental results. The last part of the chapter discusses the perspectives on the SOT-FMR measurements using topological insulators as spin-current generators. In **chapter 4**, the magnetoresistance of the 3D TI HgTe will be studied in the presence of an in-plane magnetic field, followed by band structure calculations attempting to explain the PHE and MR oscillation results. Finally, results are summarized in **chapter 5**.

1

References

[1] S. Samavedam, "Five trends that will shape the future semiconductor technology landscape." https://www.imec-int.com/en/articles/five-trends-will-shape-future-semiconductor-technology-landscape (accessed on 12.12.2020), jul 2020.

[2] M. Lapedus, "5/3nm Wars Begin." https://semiengineering.com/5-3nm-wars-begin/ (accessed on 16.12.20), jan 2020.

[3] D. Pesin and A. H. MacDonald, "Spintronics and pseudospintronics in graphene and topological insulators," *Nature Materials*, vol. 11, pp. 409–416, 2012.

[4] G. Binasch, P. Grünberg, F. Saurenbach, and W. Zinn, "Enhanced magnetoresistance in layered magnetic structures with antiferromagnetic interlayer exchange," *Physical Review B*, vol. 39, no. 7, pp. 4828–4830, 1989.

[5] M. N. Baibich, J. M. Broto, A. Fert, F. N. Van Dau, F. Petroff, P. Etienne, G. Creuzet, A. Friederich, and J. Chazelas, "Giant magnetoresistance of (001)Fe/(001)Cr magnetic superlattices," *Physical Review Letters*, vol. 61, no. 21, pp. 2472–2475, 1988.

[6] M. Julliere, "Tunneling between ferromagnetic films," *Physics Letters A*, vol. 54A, no. 3, pp. 225–226, 1975.

[7] J. S. Moodera, L. R. Kinder, T. M. Wong, and R. Meservey, "Large magnetoresistance at room temperature in ferromagnetic thin film tunnel junctions," *Physical Review Letters*, vol. 74, no. 16, pp. 3273–3276, 1995.

[8] F. Bonell, T. Hauet, S. Andrieu, F. Bertran, P. Le Fèvre, L. Calmels, A. Tejeda, F. Montaigne, B. Warot-Fonrose, B. Belhadji, A. Nicolaou, and A. Taleb-Ibrahimi, "Spin-polarized electron tunneling in bcc FeCo/MgO/FeCo(001) magnetic tunnel junctions," *Physical Review Letters*, vol. 108, no. 176602, pp. 1–5, 2012.

[9] R. Wood, "Future hard disk drive systems," *Journal of Magnetism and Magnetic Materials*, vol. 321, pp. 555–561, 2009.

[10] J. C. Slonczewski, "Current-driven excitation of magnetic multilayers," *Journal of Magnetism and Magnetic Materials*, vol. 159, pp. L1–L7, 1996.

[11] L. Berger, "Emission of spin waves by a magnetic multilayer traversed by a current," *Physical Review B*, vol. 54, no. 13, pp. 9353–9358, 1996.

[12] S. I. Kiselev, J. C. Sankey, I. N. Krivorotov, N. C. Emley, R. J. Schoelkopf, R. A. Buhrman, and D. C. Ralph, "Microwave oscillations of a nanomagnet driven by a spin-polarized current," *Nature*, vol. 425, pp. 380–383, 2003.

[13] J. A. Katine, F. J. Albert, R. A. Buhrman, E. B. Myers, and D. C. Ralph, "Current-driven magnetization reversal and spin-wave excitations in Co/Cu/Co pillars," *Physical Review Letters*, vol. 84, no. 14, pp. 3149–3152, 2000.

[14] A. Manchon, J. Železný, I. M. Miron, T. Jungwirth, J. Sinova, A. Thiaville, K. Garello, and

P. Gambardella, "Current-induced spin-orbit torques in ferromagnetic and antiferromagnetic systems," *Reviews of Modern Physics*, vol. 91, no. 035004, 2019.

[15] A. D. Kent and D. C. Worledge, "A new spin on magnetic memories," *Nature Nanotechnology*, vol. 10, pp. 187–191, 2015.

[16] S. S. P. Parkin, M. Hayashi, and L. Thomas, "Magnetic Domain-Wall Racetrack Memory," *Science*, vol. 320, no. 5873, pp. 190–194, 2008.

[17] P. Gambardella and I. M. Miron, "Current-induced spin-orbit torques," *Philosophical Transactions of the Royal Society A: Mathematical, Physical and Engineering Sciences*, vol. 369, pp. 3175–3197, 2011.

[18] A. Manchon and S. Zhang, "Theory of nonequilibrium intrinsic spin torque in a single nanomagnet," *Physical Review B*, vol. 78, no. 212405, pp. 1–4, 2008.

[19] A. Manchon and S. Zhang, "Theory of spin torque due to spin-orbit coupling," *Physical Review B*, vol. 79, no. 094422, pp. 1–9, 2009.

[20] A. Matos-Abiague and R. L. Rodríguez-Suárez, "Spin-orbit coupling mediated spin torque in a single ferromagnetic layer," *Physical Review B*, vol. 80, no. 094424, pp. 1–6, 2009.

[21] I. M. Miron, K. Garello, G. Gaudin, P. J. Zermatten, M. V. Costache, S. Auffret, S. Bandiera, B. Rodmacq, A. Schuhl, and P. Gambardella, "Perpendicular switching of a single ferromagnetic layer induced by in-plane current injection," *Nature*, vol. 476, pp. 189–193, 2011.

[22] M. I. Dyakonov and V. I. Perel, "Current-induced spin orientation of electrons in semiconductors," *Physics Letters A*, vol. 35A, no. 6, pp. 459–460, 1971.

[23] J. E. Hirsch, "Spin Hall Effect," *Physical Review Letters*, vol. 83, no. 9, pp. 1834–1837, 1999.

[24] L. Liu, T. Moriyama, D. C. Ralph, and R. A. Buhrman, "Spin-torque ferromagnetic resonance induced by the spin Hall effect," *Physical Review Letters*, vol. 106, no. 036601, pp. 1–4, 2011.

[25] L. Liu, C. F. Pai, D. C. Ralph, and R. A. Buhrman, "Magnetic oscillations driven by the spin hall effect in 3-terminal magnetic tunnel junction devices," *Physical Review Letters*, vol. 109, no. 186602, pp. 1–5, 2012.

[26] L. Liu, C. F. Pai, Y. Li, H. W. Tseng, D. C. Ralph, and R. A. Buhrman, "Spin-torque switching with the giant spin hall effect of tantalum," *Science*, vol. 336, no. 6081, pp. 555–558, 2012.

[27] S. Fukami, T. Anekawa, C. Zhang, and H. Ohno, "A spin-orbit torque switching scheme with collinear magnetic easy axis and current configuration," *Nature Nanotechnology*, vol. 11, pp. 621–625, 2016.

[28] K. Garello, C. O. Avci, I. M. Miron, M. Baumgartner, A. Ghosh, S. Auffret, O. Boulle, G. Gaudin, and P. Gambardella, "Ultrafast magnetization switching by spin-orbit torques," *Applied Physics Letters*, vol. 105, no. 212402, pp. 1–6, 2014.

[29] S. V. Aradhya, G. E. Rowlands, J. Oh, D. C. Ralph, and R. A. Buhrman, "Nanosecond-Timescale Low Energy Switching of In-Plane Magnetic Tunnel Junctions through Dynamic Oersted-Field-Assisted Spin Hall Effect," *Nano Letters*, vol. 16, pp. 5987–5992, 2016.

[30] V. M. Edelstein, "Spin polarization of conduction electrons induced by electric current in two-dimensional asymmetric electron systems," *Solid State Communications*, vol. 73, no. 3, pp. 233–235, 1990.

[31] V. V. Bel'kov and S. D. Ganichev, "Magneto-gyrotropic effects in semiconductor quantum wells," *Semiconductor Science and Technology*, vol. 23, no. 114003, pp. 1–11, 2008.

[32] M. Z. Hasan and C. L. Kane, "Colloquium: Topological insulators," *Reviews of Modern Physics*, vol. 82, no. 3045, 2010.

[33] X. L. Qi and S. C. Zhang, "Topological insulators and superconductors," *Reviews of Modern Physics*, vol. 83, no. 1057, 2011.

[34] L. Fu, C. L. Kane, and E. J. Mele, "Topological insulators in three dimensions," *Physical Review Letters*, vol. 98, no. 106803, pp. 1–4, 2007.

[35] J. E. Moore and L. Balents, "Topological invariants of time-reversal-invariant band structures," *Physical Review B*, vol. 75, no. 121306(R), pp. 1–4, 2007.

[36] R. Roy, "Topological phases and the quantum spin Hall effect in three dimensions," *Physical Review B*, vol. 79, no. 195322, pp. 1–5, 2009.

[37] D. Hsieh, D. Qian, L. Wray, Y. Xia, Y. S. Hor, R. J. Cava, and M. Z. Hasan, "A topological Dirac insulator in a quantum spin Hall phase," *Nature*, vol. 452, pp. 970–974, 2008.

[38] I. Garate and M. Franz, "Inverse spin-galvanic effect in the interface between a topological insulator and a ferromagnet," *Physical Review Letters*, vol. 104, no. 146802, pp. 1–4, 2010.

[39] Y. Wang, R. Ramaswamy, and H. Yang, "FMR-related phenomena in spintronic devices," *Journal of Physics D: Applied Physics*, vol. 51, jun 2018.

[40] T. Yokoyama, J. Zang, and N. Nagaosa, "Theoretical study of the dynamics of magnetization on the topological surface," *Physical Review B*, vol. 81, no. 241410(R), pp. 1–4, 2010.

[41] A. R. Mellnik, J. S. Lee, A. Richardella, J. L. Grab, P. J. Mintun, M. H. Fischer, A. Vaezi, A. Manchon, E. A. Kim, N. Samarth, and D. C. Ralph, "Spin-transfer torque generated by a topological insulator," *Nature*, vol. 511, pp. 449–451, 2014.

[42] Y. Xu, I. Miotkowski, C. Liu, J. Tian, H. Nam, N. Alidoust, J. Hu, C. K. Shih, M. Z. Hasan, and Y. P. Chen, "Observation of topological surface state quantum Hall effect in an intrinsic three-dimensional topological insulator," *Nature Physics*, vol. 10, pp. 956–963, 2014.

[43] R. Yoshimi, A. Tsukazaki, Y. Kozuka, J. Falson, K. S. Takahashi, J. G. Checkelsky, N. Nagaosa, M. Kawasaki, and Y. Tokura, "Quantum Hall effect on top and bottom surface states of topological insulator $(Bi_{1-x}Sb_x)_2$ Te_3 films," *Nature Communications*, vol. 6, no. 6627, pp. 1–6, 2015.

[44] C. Brüne, C. X. Liu, E. G. Novik, E. M. Hankiewicz, H. Buhmann, Y. L. Chen, X. L. Qi, Z. X. Shen, S. C. Zhang, and L. W. Molenkamp, "Quantum Hall effect from the topological surface states of strained bulk HgTe," *Physical Review Letters*, vol. 106, no. 126803, pp. 1–4, 2011.

[45] C. Brüne, C. Thienel, M. Stuiber, J. Böttcher, H. Buhmann, E. G. Novik, C. X. Liu, E. M. Hankiewicz, and L. W. Molenkamp, "Dirac-screening stabilized surface-state transport in a topological insulator," *Physical Review X*, vol. 4, no. 041045, pp. 1–6, 2014.

[46] J. Wiedenmann, E. Bocquillon, R. S. Deacon, S. Hartinger, O. Herrmann, T. M. Klapwijk, L. Maier, C. Ames, C. Brüne, C. Gould, A. Oiwa, K. Ishibashi, S. Tarucha, H. Buhmann, and L. W. Molenkamp, "4π-periodic Josephson supercurrent in HgTe-based topological Josephson junctions," *Nature Communications*, vol. 7, no. 10303, 2016.

2

Fundamental concepts

Spin-orbit coupling (SOC) is a key ingredient in the investigations described in this thesis. This interaction between the charge and the spin of the electron plays an essential role in the spin-splitting of semiconductor heterostructures [1, 2], in the anisotropy in the magnetoresistance of ferromagnet materials [3], in the origin of topological insulators [4, 5] and in the spin-orbit torques (SOTs) generated by them in ferromagnetic materials [6]. This chapter is organized in two parts. The first part deals with key concepts of SOC and with the properties of HgTe, the material system of interest in this thesis. The first section aims to briefly introduce the concept of SOC, followed by its manifestation in semiconductor materials, where the Rashba and Dresselhaus effects will be discussed. Then, the reader will be introduced to the concept of topological insulators and, specifically to the 3D TI HgTe. A discussion of the band structure of this material and how it can be engineered into a topological insulator will be provided, followed by experimental evidences of its band structure. The second part of this chapter introduces concepts of ferromagnetism, how ferromagnets can be characterized with magnetotransport and ferromagnetic resonance measurements and, finally, how spin-transfer torques can be qualitatively and quantitatively described.

2.1. Spin-orbit coupling

Spin-orbit coupling (SOC) is an interaction between charge and spin of an electron. From special relativity, an electron moving with velocity v in an electric field E experiences a magnetic field $\vec{B} = -\frac{1}{c}(\vec{v} \times \vec{E})$ in its reference frame, where c is the speed of the light. This motion produces a magnetic field at the location of the electron, which couples and it couples with the electron spin as $\vec{\sigma} \times \vec{B}$, where $\vec{\sigma} = (\sigma_x, \sigma_y, \sigma_z)$ and σ_x, σ_y and σ_z are the Pauli matrices [7]. In other words, the spin-orbit coupling is the interaction of the magnetic moment (spin) of the electron with the *effective* magnetic field the electrons experience due to their orbital motion around the nucleus. Assuming a radially symmetric potential V, the spin-orbit Hamiltonian for a non-relativistic electron in vacuum can be written as

$$H_{SO,vac} = \lambda_{vac}\sigma \cdot (\vec{k} \times \nabla V) \tag{2.1}$$

Here, $\lambda_{vac} = -\hbar^2/4{m_0}^2c^2 \approx 3.7 \times 10^{-6}\text{Å}^2$, $\hbar$, c, m_0 and $\vec{k}$ are the Planck's constant, the speed of light, the electron mass and the electron momentum, respectively [7, 8].

In solids, Rashba and Dresselhaus effects are manifestations of spin-orbit coupling [8]. SOC also plays a significant role in the inverse Edelstein [9] and spin Hall [10] effects (where spin-polarized currents can be generated in the absence of external magnetic fields) and it is the key ingredient to understand topological insulators and the quantum spin-Hall effect [4, 5]. In spintronics, spin-orbit coupling is at the core of power-efficient devices based on the spin degree of freedom [6].

The following sections present a short review of the consequences of the spin-orbit coupling that will be relevant for the investigations performed in this thesis.

2.2. Consequences of SOC in semiconductors

In semiconductors, in the absence of magnetic field, spin degeneracy of electrons and holes is a combined effect of the inversion symmetry in space and time, given by the relationship $E_\uparrow(\vec{k}) = E_\downarrow(\vec{k})$, where "↑" and "↓" denotes up and down spins, respectively, and $\vec{k}$ the wave vector for single electrons/holes. However, if carriers move through an inversion-asymmetric potential, the spin degeneracy is broken even in the absence of an external magnetic field. For this scenario, one obtains two energy dispersion branches, namely $E_\uparrow(\vec{k})$ and $E_\downarrow(\vec{k})$. In heterostructures and quasi-2D quantum wells, the spin degeneracy can be removed via a bulk inversion asymmetry (BIA) of the underlying crystal or via a structural inversion asymmetry (SIA) of the confinement potential.

Dresselhaus has shown that spin degeneracy is removed in crystals lacking an inversion symmetry center, such as the zinc blende structure [1]. While a diamond structure is a face-centered cubic (fcc) lattice with a basis consisting of two atoms of the same type, the zincblende structure can be seen as a diamond lattice, but with the two different atoms forming the basis of the fcc lattice. Since HgTe crystallizes into a fcc lattice, the effects of the SOC in this type of structure will be discussed in Sec. 2.3. Moreover, in 1960, Rashba demonstrated that an asymmetry in the carrier confining potential also removes the spin-degeneracy leading to a spin splitting linear in k [11, 12].

One way to qualitatively visualize how electrons "feel" the asymmetry in the spatial environment is to look into the envelope function approximation (EFA), which in simple terms, is a slowly varying modulation of the Bloch functions that oscillate rapidly in the lattice-periodic scale [8, 13]. This is a valid approximation when the spatial scale at which the wave function varies is larger than the lattice period. In the EFA, one can say that the potential variation is so slow that the electrons feel just a macroscopic average of the crystalline lattice. For the case of SIA spin splitting, the Bloch part feels the atomic fields while the envelope function feels the macroscopic environment. Thus, structural inversion asymmetry (SIA) spin splitting can be obtained only if there is both a macroscopic electric field and a microscopic electric field originating from the atomic cores. On the other hand, bulk inversion asymmetry (BIA) spin splitting depends only on microscopic electric fields [7, 8].

The inversion symmetry transforms the wave vector from $\vec{k}$ to $-\vec{k}$, leaving spin orientation invariant. If both inversion and time-reversal symmetries are present in the crystal, the dispersion relations are degenerate, i.e., $E_\uparrow(\vec{k}) = E_\downarrow(\vec{k})$. One of the strongest manifestations of the SO interaction is the lifting of the six-fold degeneracy of the valence band at $k = 0$, where the two-fold branch (with total angular momentum $J = \frac{1}{2}$) is lowered energetically. In GaAs the *spin-orbit split-off* energy of Γ_7 is $\Delta \approx 340$ meV [8]. The case of HgTe and CdTe will be discussed in Sec. 2.3.

2.2.1. Dresselhaus spin-orbit coupling

In crystals lacking an inversion center (such as GaAs, InSb, CdTe and HgTe zincblende structures), $E_\uparrow(\vec{k}) = E_\downarrow(\vec{k})$ is lifted. The bulk inversion asymmetry (BIA) changes the dispersion relation in a way that, in systems where time-reversal symmetry is preserved, i.e., in the absence of magnetic field, only the relation $E_\uparrow(\vec{k}) = E_\downarrow(-\vec{k})$ is valid. For nanostructures such as strongly confined two-dimensional electron gases (2DEGs) or quantum wells (QW) grown in the (001)-direction, the leading order effect of BIA is derived from a bulk Dresselhaus Hamiltonian [1] (see Eq. 3.29 in Ref. [7]) by taking the expectation value in the z direction and keeping only terms linear in k. Therefore, the Dresselhaus contribution can be expressed via the following Hamiltonian [1, 8]:

$$H_D = \beta(\sigma_x k_x - \sigma_y k_y) \tag{2.2}$$

2

Here, the parameter β represents the strength of the Dresselhaus spin-splitting, given in units of eV m. This equation corresponds to the interaction of an effective $k-$dependent magnetic field (named here as SO field) with the electron spin. Thus, the Hamiltonian for a 2DEG can be written as [8]

$$H_{SO} = H_0 + H_D = \frac{\hbar^2 k^2}{2m} + \beta(\sigma_x k_x - \sigma_y k_y) \tag{2.3}$$

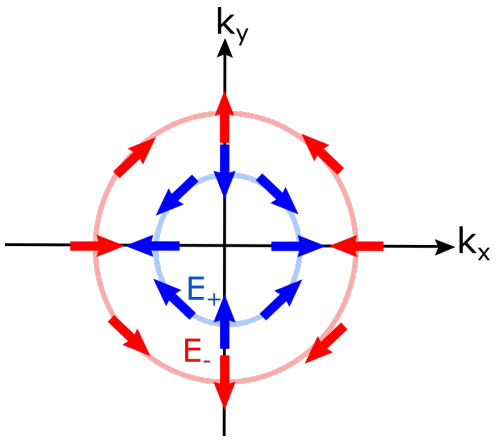

Figure 2.1: Fermi contours derived from Eq. (2.3). The blue and red circles represent the inner (E_+) and outer (E_-) bands, respectively. Here, the arrows represent the orientation of the SO-induced field as a function of momentum k, where k_x corresponds to the [100] crystal direction.

The spin polarization representing the Hamiltonian in Eq. (2.3) are depicted in Fig. 2.1. Here, the blue and red lines and arrows represent the respective inner and outer bands and the orientation of the effective SO field. The inner and outer bands are now on labeled as E_+ and E_-, respectively.

2.2.2. Rashba-Bychkov spin-orbit coupling

Another way to lift the degeneracy of the energy bands is through a structural inversion symmetry breaking. As an example, we take an asymmetric quantum well, lacking an inversion center in the growth direction. In asymmetric barriers, an electron with charge $-e$ experiences a "tilted" energy potential V associated with an electric field $\vec{E} = -\nabla V$ oriented along the growth direction. In this way, electrons propagating in this electric field experience in their own reference frame an *effective* magnetic field B_{eff} given by

$$\vec{B}_{eff} = -\frac{1}{c^2}\vec{v} \times \vec{E} \tag{2.4}$$

with c being the speed of light. This magnetic field is oriented perpendicularly to the direction of propagation and to the electric field E. As shown by Vasko [14] and Bychkov and Rashba [2], the term described above leads to an energy splitting between spin-up and spin-down electrons, similar to the spin-orbit contribution in atoms.

For two-dimensional electron gases with electric fields along the z direction (for instance, a top gate electrode), the effective magnetic field B_{eff} is both perpendicular to the carrier velocity and the electric field (see Eq. (2.4)). This SO-induced magnetic field will couple to the electron spins and, therefore, the spins of the carriers are coupled perpendicularly to its momentum. The Rashba Hamiltonian can be written as [2]

$$H_{SO} = H_0 + H_R = \frac{\hbar^2 k^2}{2m} + \alpha \vec{e}_z \cdot (\sigma_x k_y - \sigma_y k_x) \tag{2.5}$$

where $\vec{e}_z$ is the unit vector in the z-direction, i.e., in the growth direction.

The energy splitting between the E_+ (blue) and E_- (red) bands is illustrated in Fig. 2.2a. In this figure, E_0 represents the degenerated energy bands in the absence of SOC. The respective Fermi contours at the Fermi energy, E_F, along with the orientation of the effective magnetic field (spins), is shown in Fig. 2.2b.

The parameter α is the Rashba parameter, a quantity that gives the strength of the spin-orbit coupling and is often determined experimentally by the analysis of the Shubnikov-de Haas oscillations of the resistance in an applied magnetic field.

The first experimental observations of Rashba spin-splitting were reported in III-V 2D heterostructures [15, 16] via magnetotransport measurements and for the surface state of Au(111) via angle-resolved photoelectron spectroscopy (ARPES) [17], followed by subsequent investigations of the effect [18, 19]. Spin splittings were also observed for other materials and the typical values for the α parameter are 0.67×10^{-11} eV m in InAlAs/InGaAs structures [20]. ARPES measurements also show that for topological insulator systems such as Bi_2Se_3 [21], the Rashba parameter reaches values of about 4×10^{-10} eV m, which is two orders of magnitude larger than in typical III-V two-dimensional structures [15, 16]. For crystals formed by atoms with large atomic numbers, the electrons experience not only the asymmetric confining potential from the quantum well but also significative potential gradients due to the electron orbitals. For this reason, the Rashba effect is particularly strong for these material systems. In HgTe the Rashba parameter was reported to be of around 2×10^{-11} eV m [22].

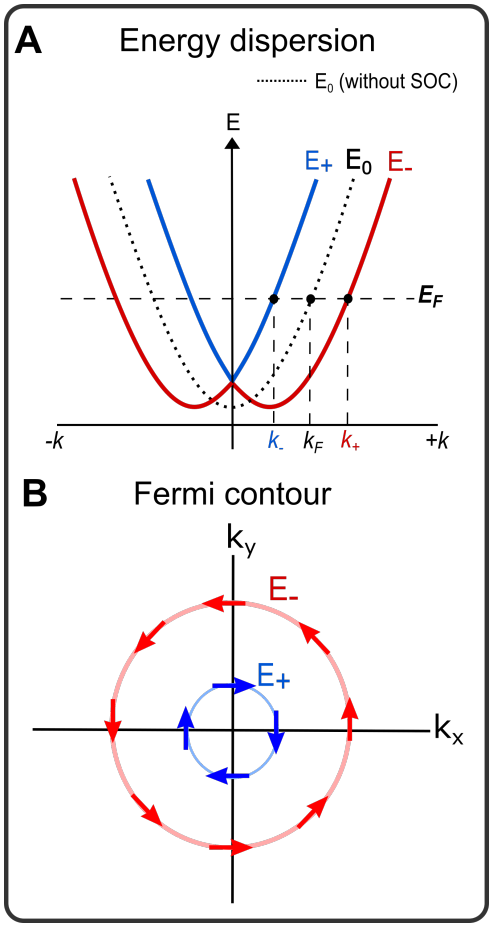

Figure 2.2: a) Schematic energy dispersion of a 2D free-electron gas induced by Rashba spin–orbit coupling. The blue and red lines represent both inner (E_+) and outer (E_-) bands. Here, E_0 represents the degenerated energy bands, in the absence of SOC. b) Fermi contours at E_F for the energy dispersion shown in a). The arrows represent the orientation of the SO-induced field as a function of momentum k.

Both Dresselhaus and Rashba SO couplings generate a "spin-momentum locking" of the electron spin to its linear momentum and lift the spin degeneracy of the energy bands. Both Rashba and Dresselhaus spin-orbit effects will be discussed in more depth in Chap. 4 in order to study anisotropies in the magnetoresistance of HgTe in the presence of in-plane magnetic fields.

2.2.3. Edelstein or inverse spin galvanic effect

One of the most striking consequences of the locking between momentum and spin is that an applied electric field can induce not only an electric current but also a spin polarization. This effect was suggested by Ivchenko and Pikus in 1978 [23] and further investigated in more detail in the framework of the Rashba SO effect in a 2DEG [9, 24].

For a given Fermi energy where the inner and outer energy bands are occupied, the carrier distribution is modified by an external electric field E and by scattering events. The electric field accelerates the carriers in the direction of the field, thus, displacing the Fermi surface from its equilibrium, as schematically depicted in Figs. 2.3a and 2.3b. This displacement is mathematically described as $\delta k_{\pm} = \frac{-eE\tau_{\pm}}{\hbar}$ (where $\pm$ correspond to inner and outer energy bands, respectively), resulting in an unequal occupation of $+k$ and $-k$ states in the presence of an electric field [7]. Since in a Rashba system the spin and momentum of the carriers are locked to each other, a *non-equilibrium* unequal occupation of carriers will also produce a non-zero spin density. According to Edelstein, [9], the spin-orbit energy can be considered as the Zeeman energy of the electron spins in the induced magnetic field and generate spin-polarization.

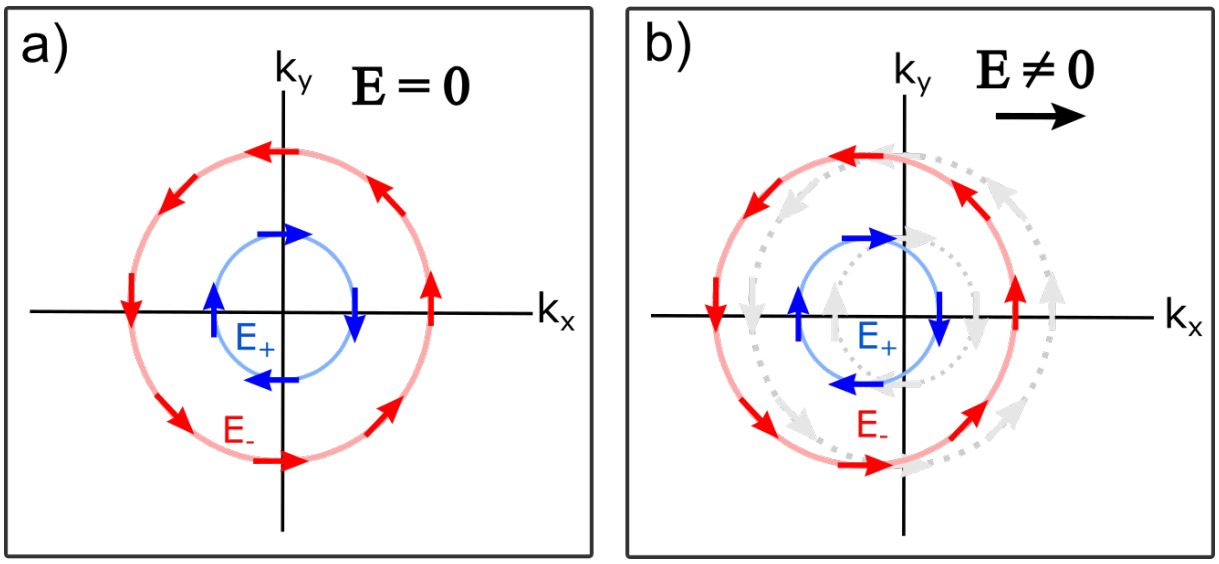

Figure 2.3: Fermi contours and spin texture (arrows) of a 2DEG with Rashba SO coupling in the absence a) and b) in the presence of an external electric field E. The carriers - here electrons - are accelerated in the direction of the field causing a shift of the Fermi contours in k-space. The gray lines correspond to the equilibrium transport, while the blue and red correspond to the inner (E_+) and outer (E_-) energy subbands, respectively. In the presence of an electric field, the two Fermi contours partially compensate each other and a finite spin polarization oriented in y-direction is created.

In the Rashba system, for an electric field applied in the x- direction ($\vec{E} = E\hat{x}$), the spin accumulation $\delta\hat{\sigma}$ is [25]:

2

$$\langle \delta\hat{\sigma} \rangle \approx -\frac{m\alpha}{e\hbar E_F} j\, \hat{y} \tag{2.6}$$

where j is the charge current density. The Edelstein effect is an important ingredient in the generation of spin-polarized currents in topological insulators. Chapter 3 will show that an electric field applied in the surface states of 3D TI HgTe can generate a spin polarization that can be transferred to an adjacent ferromagnetic thin film, thus, applying torque on its magnetization.

2.2.4. Topological Insulators

Before we describe the role of SOC in topological insulators, it is instructive to first understand the quantum Hall effect (QHE), which is a key signature of topology in two-dimensional systems. This effect was first demonstrated in 1980 by Klaus von Klitzing [26], where he showed that the Hall conductance of a two-dimensional electron gas at very low temperatures exhibits a staircase sequence of Hall plateaus at a strong magnetic field applied perpendicular to the 2DEG. The values of the Hall conductance are integer multiples of the conductance quantum, e^2/h, which depends exclusively on fundamental constants of nature and its precision is independent of sample impurity, geometry or different electron concentrations. This precision was explained in terms of topological invariants known as Chern numbers [27]. In simple terms, the Chern number is an integer and is topological in the sense that it is invariant under small deformations of the Hamiltonian [28]. Therefore, the preciseness of the Hall plateaus can be related to the topological robustness of the Chern numbers. There are several considerations made to arrive at this conclusion and the reader is referred to reference [28] and references therein for a didactical explanation.

In 2005, Kane and Mele predicted the existence of a new state of matter which is protected by topology, the *Quantum Spin Hall* insulator state in graphene [29, 30]. This state was predicted to consist of two counterpropagating edge states with opposite spin polarization and, in contrast to the QH state, no magnetic field is needed to create these edge states. However, an experimental observation of the effect is not possible, since the energy scales at which the effect would be observable are small, given that carbon is a very light element and, therefore, the SOC on it is also small. Shortly after Kane and Mele's work, Bernevig, Hughes and Zhang predicted that this state of matter could be observed in other material systems, including HgTe quantum wells [31]. HgTe is special because both Hg and Te are heavy atoms, which leads to strong SOC, so that relativistic corrections to the positions of the energy levels become relevant.

As it will be discussed in detail in Sec. 2.3.1, the combination of SOC and the heavy masses

of HgTe lead to an inversion of the band structure of this material system. In simple terms, in a trivial band structure, the conduction band (CB) is energetically above the valence band (VB), resulting in a positive energy gap (see Fig. 2.5b for an example). For the case of HgTe, the corrections mentioned above lead to a non-trivial band structure, where the VB is energetically above the CB, i.e., its band structure is inverted (see Fig. 2.5a for an example). This inversion of the energy bands also implies a change of the band topology in the system. Combined with quantum confinement, HgTe (quantum wells) host a topologically non-trivial state, which gives to the quantum spin Hall effect (QSHE). This effect was first observed in 2007 in HgTe/(Hg,Cd)Te quantum wells with a critical thickness $d > 6.3$ nanometers, where it was demonstrated that the conductance in this system exhibited the value of $G = 2e^2/h$ [32].

The discovery of the QSHE paved the way for the prediction of three-dimensional topological insulators (3D TIs) [33–35]. Topological insulators are quantum materials that have a band gap like a normal insulator, however, they also possess topologically protected conducting surface states resulting from the band inversion. These states are protected by the time-reversal symmetry and nonmagnetic impurities or any other time-reversal invariant local perturbations cannot cause elastic backscattering, making the conductance of these states very robust.

For the case of three-dimensional topological insulators, first discovered in 2008 in $Bi_{1-x}Sb_x$ [36], the electrical conduction happens at the surfaces of the material, while the bulk remains insulating, i.e. an energy gap between the CB and the VB. As it will be seen in the next section, 3D TIs can exist because of the strong mass-velocity correction combined with strong SOC, which causes the band ordering in some materials to invert [37]. At the boundary between a material with band inversion and a material with normal/trivial band order, the energy bands have to connect at the interface, leading to the formation of states at the boundary (surface) between the two materials. These surface states have a linear dispersion at $k \approx 0$ - known as Dirac cone - and cross each other in the so-called Dirac point (see Fig. 3.1a for an example). These states can be mathematically described by the Dirac Hamiltonian [4]:

$$H_{surf} = -i\hbar v_F \vec{\sigma} \cdot \vec{\nabla} \tag{2.7}$$

where v_F is the Fermi velocity of the TSS [4]. Since these topological surface states (TSS) are a consequence of band inversion, they can only be destroyed if the band structure is strongly modified, e.g. lifting the band inversion or closing the insulating bulk gap.

Similarly to Rashba systems discussed in Sec. 2.2.2, time-reversal symmetry of the surface Hamiltonian imposes that electrons with opposite momenta ($\vec{k}$ and $-\vec{k}$) have opposite spin. However, this spin-momentum locking is fundamentally different from Rashba systems: since TSS are a consequence of band inversion, elastic backscattering without spin flipping is suppressed, making these states robust against magnetic disorder [4, 5].

Although topological insulators were first discovered in $Bi_{1-x}Sb_x$, strained HgTe was also found to be a strong topological insulator [38, 39]. The next section will explore the band structure of HgTe and its properties.

2.3. The Mighty HgTe

In In the previous sections, we have introduced the spin-orbit interaction and argued that it is an important ingredient for the existence of topological insulators. HgTe is an unique and versatile material system with strong SOC, which allows for the observation of different phases of matter, such as Weyl semimetals [40] and topological insulators [32, 38, 39]. This section focuses on the band structure of HgTe and how the topological insulator phase can be achieved.

2.3.1. Band inversion of HgTe

Since the 3D topological insulator HgTe is usually interfaced with CdTe, in this section we will introduce relativistic corrections to the Hamiltonian describing HgTe and CdTe and show that they differ drastically from each other. These corrections are significant for atoms with large atomic number and, therefore, crucial for the understanding of the band evolution of HgTe and CdTe. This section does not aim to give a detailed theoretical derivation of these corrections but its goal is to qualitatively describe the most important terms leading to the band inversion of HgTe. For the more interested reader, references [8, 37, 41] and references within provide a detailed explanation of the following qualitative discussion.

As mentioned in the previous section, HgTe and CdTe bulk materials possess a zincblende lattice structure. Also, II-VI compounds (the case of HgTe and CdTe) are direct gap semiconductors, i.e., the extreme of both conduction and valence bands are located at the Γ point ($k = 0$). The top of the valence band is composed by p-symmetric atomic orbitals and is six-fold degenerate, while the conduction band is composed out of s-states and is two-fold degenerate (two spin states). The Hamiltonian describing these bands without any relativistic correction will be generally called H_{nr}.

As shown in Figs. 2.4a and 2.4b, the energy levels of CdTe and HgTe derived from the non-relativistic Hamiltonian H_{nr} are the same. The first correction to be included to the non-relativistic term H_{nr} is the Darwin term, H_D. This correction smears the effective potential felt by the electron and changes its potential energy. This term is relevant for the orbitals only and, therefore, does not have a significant impact in the energy band alignment of both compounds, as sketched in Figs. 2.4a and 2.4b (yellow column) [37].

However, when the mass-velocity correction (H_{mv}) term is taken into account, the band structure of HgTe changes drastically in comparison to CdTe. This term shifts both the conduction and

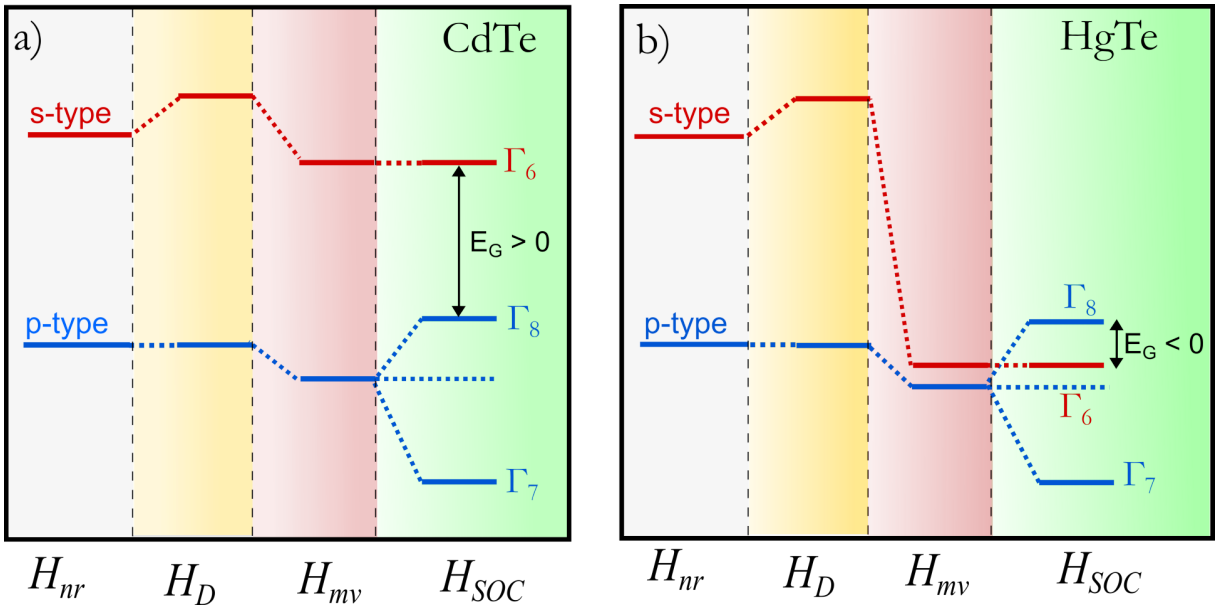

Figure 2.4: Relativistic corrections to the energy levels at the Γ point for: a) CdTe and b) HgTe. Here, H_{nr} represent the non-relativistic Hamiltonian, followed by the Darwin H_D, mass-velocity H_{mv} and spin-orbit coupling H_{SOC}, relativistic corrections, respectively. Figure adapted from [37].

valence bands of both components toward lower energies due to the difference in the atomic masses of Cd and Hg. The effect is not the same for *s*- and *p*-symmetric electrons and the impact of the mass-velocity correction is about five times larger for *s* electrons in comparison to *p* electrons [37]. Since the atomic mass of Hg is higher than Cd [1], this correction is starkest for the HgTe compound, lowering its conduction band (*s*-states) towards lower energies in comparison to the CdTe compound (red column in Figs. 2.4a 2.4b).

Finally, the spin-orbit coupling term H_{SOC} breaks the six-fold degeneracy of the valence band into Γ_7 (two-fold degenerate) and Γ_8 (four-fold degenerate) bands. For CdTe, this splitting leads to a positive energy gap ($E_G > 0$), however, in HgTe this correction leads to the inversion between the Γ_6 and the Γ_8 bands and, consequently, to a negative energy gap ($E_G < 0$). This situation is illustrated in the green columns of Figs. 2.4a and 2.4b.

After understanding the origin of the band inversion in HgTe, one needs to be able to calculate the band structure of these compounds. The next section will introduce the Kane Hamiltonian and show how parameters such as the energy gaps of HgTe and CdTe can be calculated.

2.3.2. The Kane Hamiltonian

Several of the subtleties of HgTe band structure and the derivation of the surface states are obtained by the self-consistent $k \cdot p$ calculations based on the Kane Hamiltonian and the envelope function approximation [13, 42]. The underlying idea is to use perturbation theory near one

[1] $M_{Hg} = 200.6$ u and $M_{Cd} = 112.4$ u [37]

energy extremum (usually $k = 0$) to approximate the band structure in the neighborhood. In other words, the $k \cdot p$ method allows for the calculation of an effective band structure in the vicinity of the Γ point ($k = 0$) in the reciprocal space. In order to properly discuss its results, this section aims to introduce the most relevant derivations and features of the Kane Hamiltonian. A detailed derivation of the $k \cdot p$ method can be found in [8, 41].

Elliot [43] and Dresselhaus [44] pointed out that the SO coupling may also have important contributions in the energy levels of the bulk semiconductors. In order to approximate the band structure of the zinc blende crystals, 8-band $k \cdot p$ are considered. Since time-reversal symmetry is preserved, these bands are doubly degenerate.

At $k = 0$, the conduction band, often dubbed as Γ_6, has s-like orbital character ($l = 0$) and total angular momentum $j = \frac{1}{2}$. The valence band has p-like character ($l = 1$) and splits in six degenerated subbands: Γ_8 ($j = \frac{3}{2}$) and the Γ_7 ($j = \frac{1}{2}$). The SO interaction splits the Γ_8 and the Γ_7 bands by an energy Δ. For HgTe, the spin spin-splitting is $\Delta_{HgTe} = 1.08$ eV while for CdTe $\Delta_{CdTe} = 0.91$ eV [41, 45]. The four Γ_8 bands remain degenerate at the Γ point and are often dubbed as heavy-hole (HH, $m_j = \pm\frac{3}{2}$) and light-hole (LH, $m_j = \pm\frac{1}{2}$). As an example, the described bands are illustrated in Fig. 2.5b for the band structure of CdTe.

Since the splitting of the Γ_7 band is far away in energy, it is appropriate to treat the coupling of this band perturbatively in a 6×6 Kane model. Most of the HgTe properties can be qualitatively described via the 6×6 Hamiltonian, apart from a renormalization of the band parameters for both Γ_6 and Γ_8 bands [8]. Because of their symmetry, these bands can be written as a combination of $|S\rangle$ (s-like orbital) and $|X\rangle$, $|Y\rangle$, and $|Z\rangle$ (p-like orbitals). The energy gap at $k = 0$ between the Γ_6 and Γ_8 bands is given by $E_G = E_c - E_v$, where where E_c is the energy of the Γ_6 band at $k = 0$ and E_v that of Γ_8.

Thus, the six-component basis of orbitals can be written as:

$$
\begin{aligned}
|\Gamma_6; +\frac{1}{2}\rangle &= |j = \frac{1}{2}; m_j = \frac{1}{2}\rangle = |S; \uparrow\rangle = S\uparrow, \\
|\Gamma_6; -\frac{1}{2}\rangle &= |j = \frac{1}{2}; m_j = -\frac{1}{2}\rangle = |S; \downarrow\rangle = S\downarrow, \\
|\Gamma_8; +\frac{3}{2}\rangle &= |j = \frac{3}{2}; m_j = \frac{3}{2}\rangle = |HH; \uparrow\rangle = \frac{1}{\sqrt{2}}(X + iY)\uparrow, \\
|\Gamma_8; +\frac{1}{2}\rangle &= |j = \frac{3}{2}; m_j = \frac{1}{2}\rangle = |LH; \uparrow\rangle = \frac{1}{\sqrt{6}}\left[(X + iY)\downarrow -2Z\uparrow\right], \\
|\Gamma_8; -\frac{1}{2}\rangle &= |j = \frac{3}{2}; m_j = -\frac{1}{2}\rangle = |LH; \downarrow\rangle = \frac{1}{\sqrt{6}}\left[(X - iY)\uparrow +2Z\downarrow\right], \\
|\Gamma_8; -\frac{3}{2}\rangle &= |j = \frac{3}{2}; m_j = -\frac{3}{2}\rangle = |HH; \downarrow\rangle = \frac{1}{\sqrt{2}}(X - iY)\downarrow
\end{aligned}
$$

For a heterostructure grown along the z-direction, the 6×6 Hamiltonian is given by [46]

$$H_{Kane} = \begin{pmatrix} T & 0 & -\frac{1}{\sqrt{2}}Pk_+ & \sqrt{\frac{2}{3}}Pk_z & \frac{1}{\sqrt{6}}Pk_- & 0 \\ 0 & T & 0 & -\frac{1}{\sqrt{6}}Pk_+ & \sqrt{\frac{2}{3}}Pk_z & \frac{1}{\sqrt{2}}Pk_+ \\ -\frac{1}{\sqrt{2}}Pk_- & 0 & U+V & -S_- & R & 0 \\ \sqrt{\frac{2}{3}}Pk_z & -\frac{1}{\sqrt{6}}Pk_- & -S_-^\dagger & U-V & C & R \\ \frac{1}{\sqrt{6}}Pk_+ & \sqrt{\frac{2}{3}}Pk_z & R^\dagger & C^\dagger & U-V & S_+^\dagger \\ 0 & \frac{1}{\sqrt{2}}Pk_- & 0 & R^\dagger & S_+ & U+V \end{pmatrix} \tag{2.8}$$

where:

$$\begin{aligned} k_\parallel^2 &= k_x^2 + k_y^2, k_\pm = k_x \pm ik_y, k_z = -i\frac{\partial}{\partial z} \\ T &= E_c + \frac{\hbar^2}{2m_0}\left[(2F+1)\,k_\parallel^2 + k_z\,(2F+1)\,k_z\right], \\ U &= E_v - \frac{\hbar^2}{2m_0}\left(\gamma_1 k_\parallel^2 + k_z\gamma_1 k_z\right), \\ V &= -\frac{\hbar^2}{2m_0}\left(\gamma_2 k_\parallel^2 - 2k_z\gamma_2 k_z\right), \\ R &= -\frac{\hbar^2}{2m_0}\left(\sqrt{3}\mu k_+^2 - \sqrt{3}\gamma k_-^2\right), \\ S_\pm &= -\frac{\hbar^2}{2m_0}\sqrt{3}k_\pm\left(\{\gamma_3, k_z\} + [\kappa, k_z]\right), \\ C &= \frac{\hbar^2}{m_0}k_-\,[\kappa, k_z]\,. \end{aligned}$$

with Luttinger parameters γ_1, γ_2, γ_3, κ and F characterizing the coupling between the bands, $\mu = (\gamma_3 - \gamma_2)/2$ and $\gamma = (\gamma_3 + \gamma_2)/2$. Here, $[A, B] = AB - BA$, $\{A, B\} = AB + BA$ and $E_P = 2m_0P^2/\hbar$. The parameter P describes the coupling between conduction and valence bands. The band structure parameters for HgTe and CdTe at $T = 0$ K are listed in Table 2.1.

	E_G (eV)	E_P (eV)	γ_1	γ_2	γ_3	κ	F
HgTe	-0.303	18.8	4.1	0.5	1.3	-0.4	0
CdTe	1.606	18.8	1.47	-0.28	0.03	-1.31	-0.09

Table 2.1: Energy band gap (E_G), coupling between $\Gamma_6 - \Gamma_8$ (E_P) and Luttinger parameters. Taken from Ref. [46].

The 6×6 Hamiltonian can be used to calculate the band structure of HgTe, whose energy bandgap is negative, meaning that the Γ_6 and the Γ_8 bands are inverted with respect to each other. The inversion between Γ_6 and Γ_8 bands is a necessary condition to obtain topological surface states. The inversion happens between Γ_6 and all of Γ_8. The $\Gamma_{8,LH}$ are the relevant bands

for the surface or edge states. It should, however, be reminded that unstrained bulk HgTe is a semi-metal and that the topological *insulator* phase can only be achieved by opening the band gap between the HH and LH bands that touch each other at the Γ point. As further discussed in reference [40], HgTe is an extremely versatile material system, where different topological phases can be obtained by via an ingenious strain engineering described in detail in [38, 39, 47].

A schematics of the relevant bands of HgTe and CdTe around the Γ point is shown in Figs. 2.5a and 2.5b, respectively.

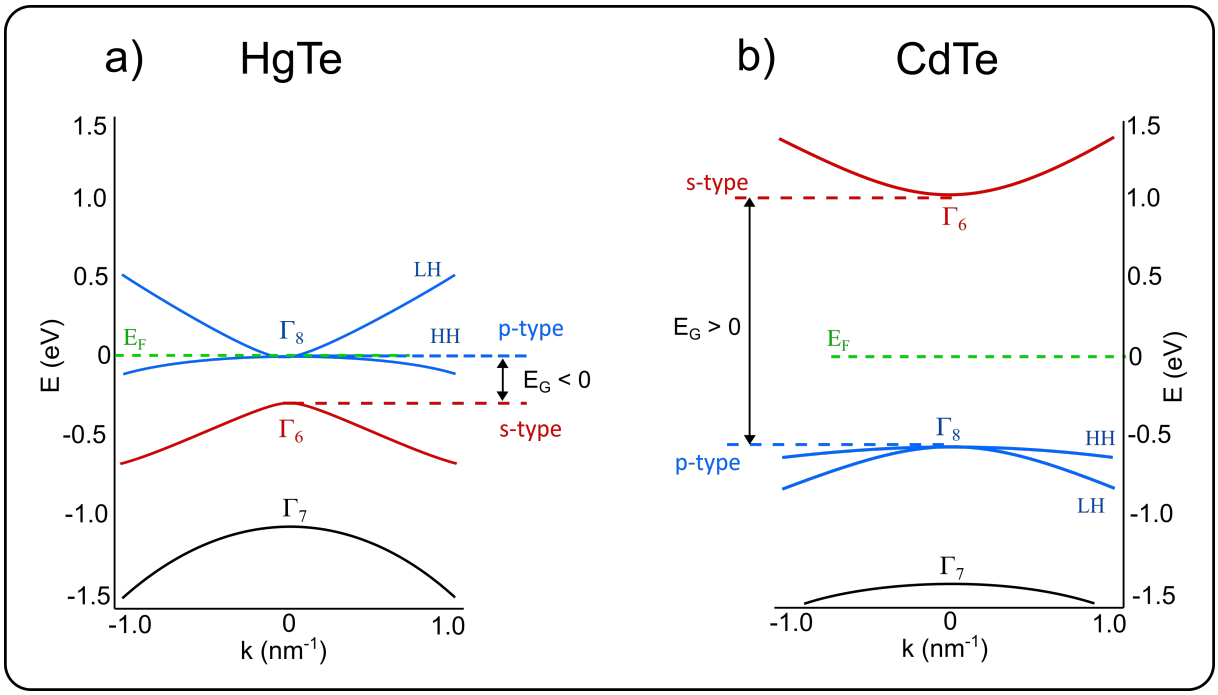

Figure 2.5: a) Schematics of the band structure of the relevant bands around the center of the Brillouin zone for a) HgTe b) CdTe. Figure adapted from [31].

The CdTe compound is a semiconductor with positive band gap $E_G \approx 1.6$ eV between the $\Gamma_{8,HH}$ (VB) and Γ_6 (CB). However, the band inversion makes bulk HgTe a semimetal, with the CB (formed by $\Gamma_{8,LH}$) and VB (formed by $\Gamma_{8,HH}$) bands degenerated at $k = 0$. In this case, the band structure of HgTe gives a key ingredient to engineer a topological insulator phase (band inversion). The next ingredient is the existence of an insulating bulk that, in its turn, necessitates the opening of a band gap.

2.3.3. Gap opening in HgTe

A gap opening in unstrained bulk HgTe (sketched in Fig. 2.6a) can be obtained via the application of tensile strain. By growing HgTe (with a lattice parameter $a_{\mathrm{HgTe}} = 0.6462$ nm) on a substrate with larger lattice parameter, such as CdTe ($a_{\mathrm{CdTe}} = 0.6482$ nm) [48], leads to an energy gap opening between the $\Gamma_{8,HH}$ and $\Gamma_{8,LH}$ bands, as sketched in Fig. 2.6b. In this case, the topological

insulator phase is formed between the $\Gamma_{8,HH}$ and $\Gamma_{8,LH}$ bands.

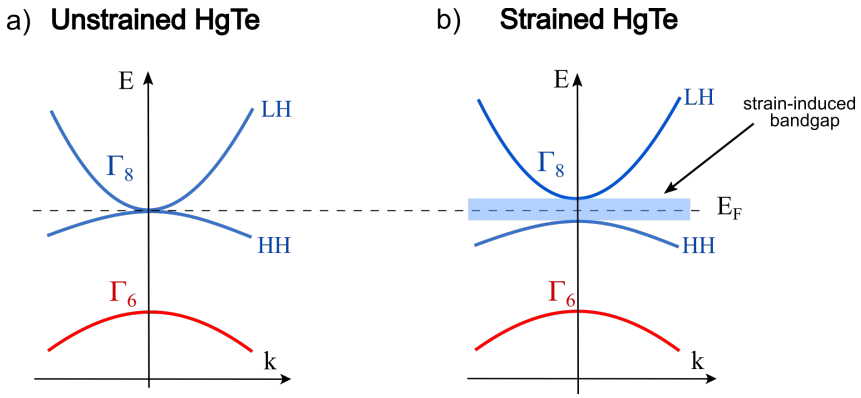

Figure 2.6: Schematic band structure of HgTe around the Fermi energy near the center of the Brillouin zone of a) unstrained and b) strained HgTe.

Realistic HgTe three-dimensional topological insulators samples are grown via molecular-beam epitaxy (MBE), since this technique allows for high sample quality. MBE growth takes place in ultra-high vacuum environment and appropriate temperatures. The desired elements are evaporated and deposited onto a substrate of choice and the desired structure is formed. The lattice mismatch of approximately 0.3 % between HgTe and CdTe allows for the growth of fully strained HgTe layers up to 200 nm, while in thicker layers the strain is relaxed by the formation of dislocations [38]. Theoretical predictions using an eight-band $k \cdot p$ model showed that the energy gap opening in HgTe is very small, of around $E_G \approx 22$ meV [38].

2.3.4. Experimental evidence for the band structure of HgTe

In order to verify the existence of topological surface states in strained bulk HgTe, ARPES measurements were performed in a 1 μm thick HgTe layer on the (001) surface grown by MBE [38]. Figure 2.7a shows the resulting spectrum. The main feature in this figure is the linear dispersing band attributed to the surface states (SSB - originating from the inversion between the $\Gamma_{8,LH}$ and Γ_6 bands) coexisting with the bulk bands (BB - corresponding to the $\Gamma_{8,HH}$ band). The Dirac point is assumed to be buried into the valence band, at approximately 30-50 meV below the band edge.

Moreover, since the topological surface state is a two-dimensional system, one way to probe electrically the existence of topological surface states in 3D topological insulators is via measurements of the quantum Hall effect. In order to perform magnetotransport measurements in the 3D TI HgTe, the samples grown via MBE are patterned into a Hall bar via optical lithography, where the length between the longitudinal voltage contacts is $L = 600\,\mu$m and the transversal voltage contacts is $W = 200\,\mu$m. The lithography fabrication process will be described in detail in Sec. 3.4. In a nutshell, the standard HgTe Hall bars are produced as follows: the HgTe and (Hg,Cd)Te layers are etched away by argon plasma into the Hall bar desired pattern (mesa). A

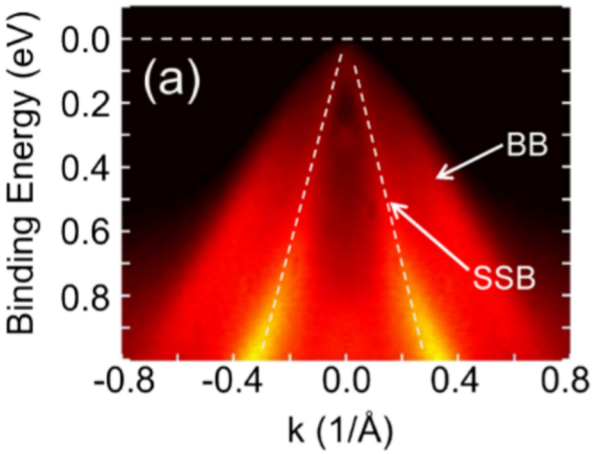

Figure 2.7: ARPES measurements on a 1 μm thick HgTe sample. The dispersion of the surface state (SSB) and bulk bands (BB) are indicated by the arrows. Figure taken from reference [38].

110 nm-thick insulator consisting of SiO_2-Si_3N_4 alternating layers is deposited on top of the Hall bar via PECVD. A 100 nm thick Au (with 5 nm Ti sticking layer) gate electrode is deposited via electron-beam evaporation on top of the insulator. Finally, the mesa contacts are obtained by depositing 50 nm AuGe and 50 nm Au via electron beam evaporation.

Figure 2.8a shows a schematic of a Hall bar configuration and the experimental setup of typical magnetotransport measurements, where an electrical current I flows through the sample from contacts 1 to 4 and the longitudinal (transversal) resistance is measured between contacts 5 and 6 (3 and 5).

The magnetotransport measurements in the presence of an out-of-plane magnetic field can be observed in Fig. 2.8, which shows the b) Hall resistance and c) longitudinal magnetoresistance of a 70 nm thick fully (tensile) strained HgTe layer as a function of applied gate voltage V_g taken at a nominal temperature of 20 mK [39]. The gate voltage V_g allows for the tunning of the carrier concentration in the sample. Several plateaus (due to the formation of Landau levels) are observed in the Hall resistance R_{xy} and the longitudinal resistance R_{xx} shows Shubnikov-de Haas (SdH) oscillations for a wide range of carrier densities (different V_g). The maxima of these oscillations correspond to the crossing of a Landau level with the Fermi energy.

The Hall plateau indexing in topological insulators (where the plateaus lead to a quantized Hall conductivity σ_{xy}) is

$$\sigma_{xy} = (\tfrac{1}{2} + \tfrac{1}{2} + j^t + j^b)\tfrac{e^2}{h} \tag{2.9}$$

where, j^t and j^b are the quantum hall indices for top and bottom topological surface states, respectively. For gate voltages $V_g = -1$ V, only an odd sequenced quantum Hall effect was

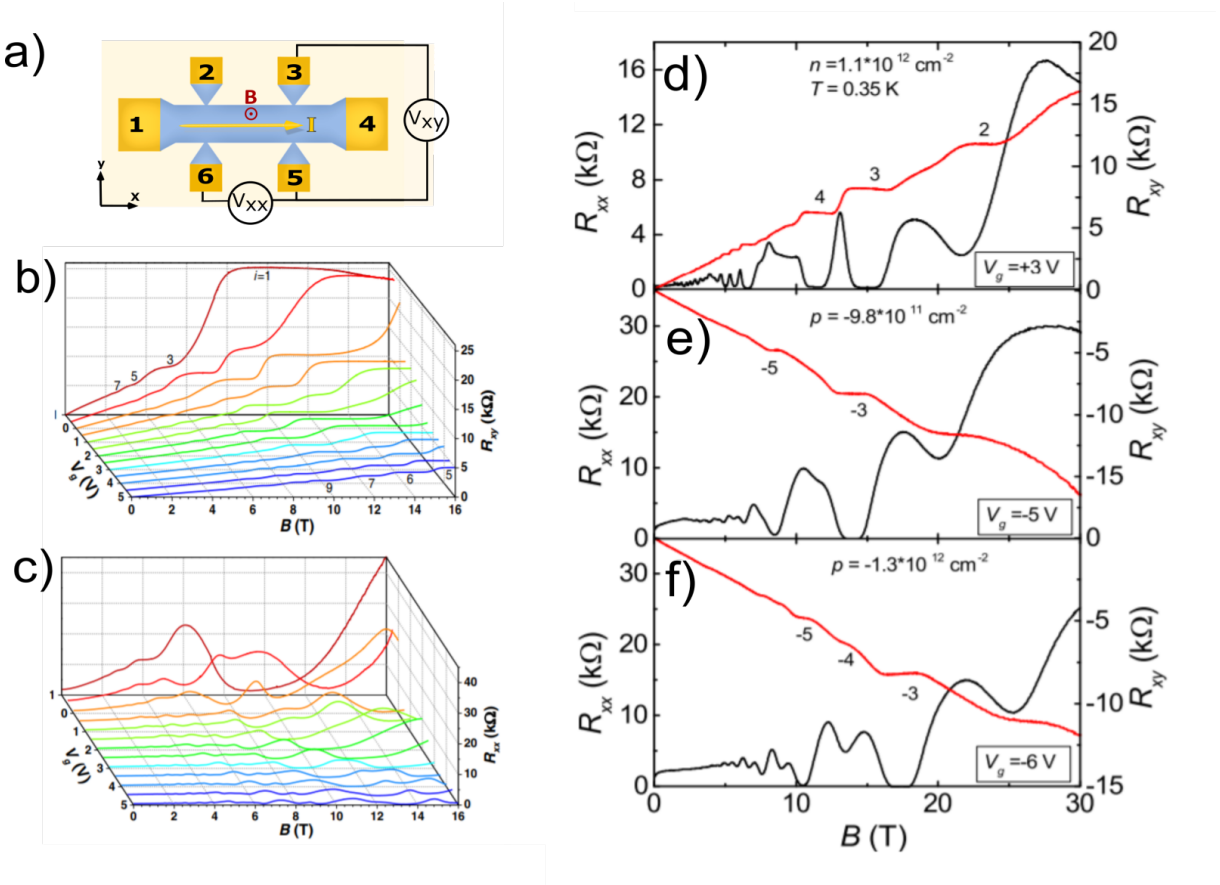

Figure 2.8: a) Hall bar schematics used to performed magnetotransport measurements and measured the longitudinal V_{xx} and transversal V_{xy} voltages. Three-dimensional plot of b) Hall resistance and c) longitudinal magnetoresistance of a 70 nm thick fully strained HgTe layer as a function of applied gate voltage V_g and out-of-plane magnetic field. d) - f) Ambipolar QHE for HgTe capped with protective layers. The oscillations in R_{xx} (black lines) and QHE in R_{xy} (red lines) for different charge-carrier concentrations and labelled filling factors. Figures a) - c) are taken from [39], d) - f) from [49].

observed (Fig. 2.8b), confirming that the observed quantum Hall effect in strained bulk HgTe indeed originates from the topological surface states.

The observation of quantum Hall plateaus for a wide range of carrier densities is surprising, since the band gap of HgTe (of the topological insulator phase) is of the order of just $E_G \approx 20$ meV [38, 39]. In order to explain such results, the authors in Ref. [39] phenomenologically searched for an effective Hartree potential that kept the electrochemical potential in the band gap constant for all gate voltages. Figures 2.9a and 2.9b shows $\vec{k} \cdot \vec{p}$ band structure calculations using a basis of 6-orbitals gate voltage values $V_g = -1$ V and $V_g = 5$ V, respectively. The carrier density at $V_g = -1$ V is $n = 3.5 \times 10^{11}\,\mathrm{cm}^{-2}$ and at $V_g = 5$ V is $n = 2.0 \times 10^{12}\,\mathrm{cm}^{-2}$. Here, the black lines represent the conduction and valence subbands, while blue and red represent the top (TSS in the figure) and bottom (BSS) topological surface states, respectively. The valence band will be here dubbed as "camel back" due to its peculiar shape: the energy dispersion around $k = 0$ resembles an electron-like quadratic dispersion with small effective mass, while at finite k values, it presents a hole-like dispersion with a high effective mass. The resulting potential is shown in Fig. 2.9c and its shape is understood as if the bulk and the topological surface states would be electrostatically decoupled, resulting in two different dielectric constants for the distribution of the potential in the sample: $\epsilon = 21$ for the bulk and $\epsilon = 3$ for the TSS. For both gate voltage values ($V_g = -1$ V and $V_g = 5$ V), the Fermi energy remains inside the band gap (as it can be seen in Figs. 2.9a and 2.9b). With the tuning of the gate voltage, there is a shift in the position of the Dirac point, while the Fermi energy of the bulk bands remains unaffected. This mechanism is named as the "Dirac screening" of the topological surface states. Since these states are metallic, they screen the applied external electric field and allow for tuning of the carrier concentration of the TSS, but not for the bulk. At $V_g = 5$ V, the carrier densities of both surfaces are different, highlighting the fact that a top gate voltage influences the top and bottom topological surfaces differently.

The fact that in the 3D TI HgTe the transport properties can be observed exclusively through the topological surface states places HgTe as an unique topological material in comparison with the Bi-based topological insulators, where parallel bulk conductivity hinders the desired topological properties.

In order to improve the sample quality of the HgTe layers, (Hg,Cd)Te protective layers were introduced as capping layers, allowing for high sample mobilities (1.5×10^5 to 3.0×10^5 cm^2/Vs for electrons and from 2.0×10^4 to 9.0×10^4 cm^2/Vs for holes) and the observation of quantum Hall effect for electron and hole transport regimes. Indeed, Figs. 2.8d-f show QHE in a 60 nm thick HgTe layer that is sandwiched between two $Hg_{0.3}Cd_{0.7}Te$ buffer layers on top (5 nm) and bottom (100 nm) at $T = 0.35$ K (the charge-carrier concentrations and filling factors are labeled in the figures). For the transport in the p-type regime, a two-carrier behavior is observed. At low magnetic fields, a positive Hall slope is observed, indicating that the electrical transport is

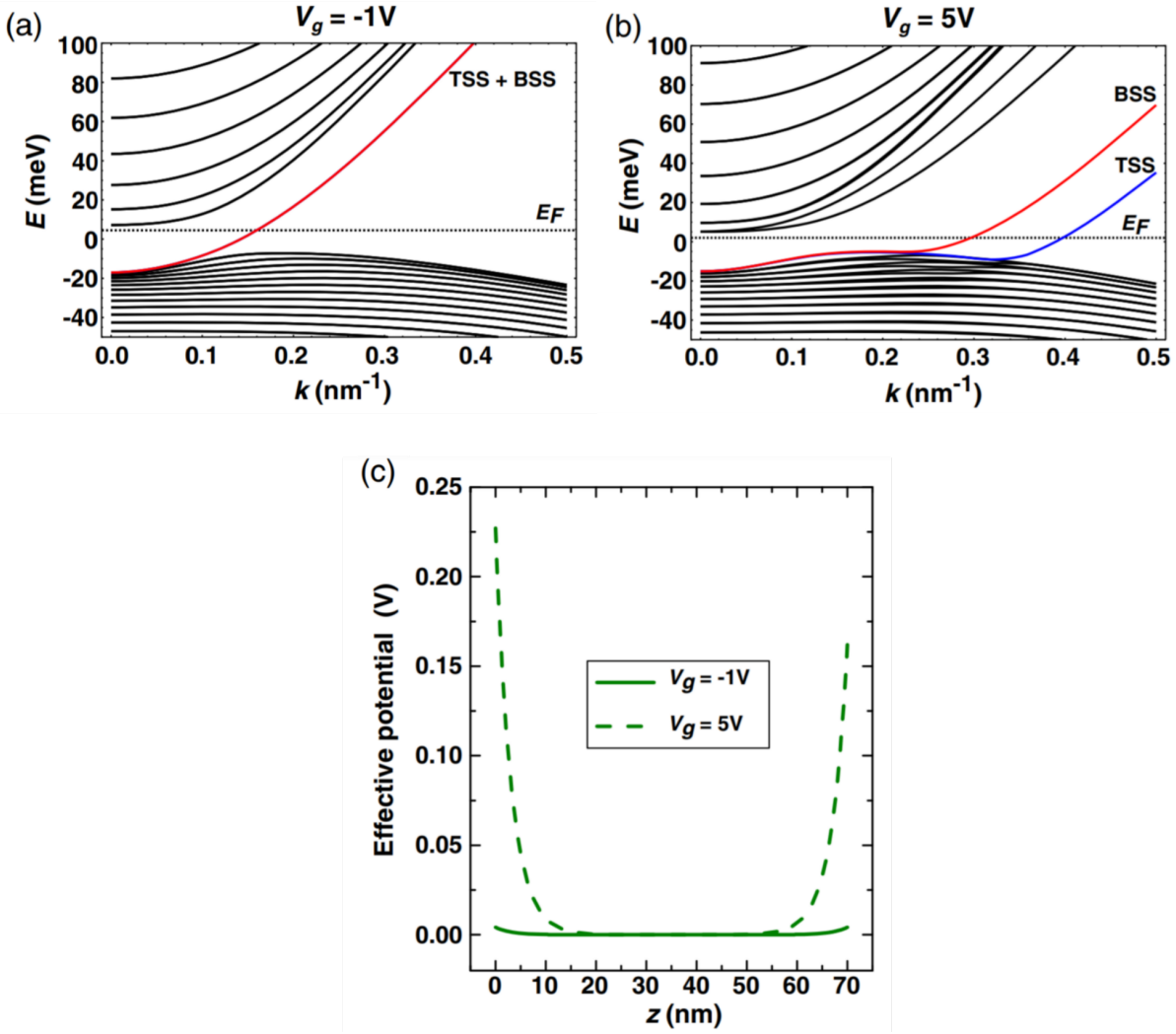

Figure 2.9: $\vec{k} \cdot \vec{p}$ band structure calculations using a basis of 6-orbitals for gate voltages a) V_g = -1 V and b) V_g = 5 V. The dispersions of the top (TSS) and bottom (BSS) surface states are respectively depicted in red and blue. c) Resulting effective electrostatic potentials for $V_g = -1$ V and b) $V_g = 5$ V. Figure taken from Ref. [39].

dominated by electrons. At high magnetic fields, the Hall resistance has a negative slope (hole transport) and also exhibits plateaus. In recent years, several studies in 3D TI HgTe show that the QHE observed in the p-type transport regime could be related to trivial (non-topological) surface states known as massive Volkov-Pankratov states arising from the localization of hole carriers. The nature of this two-carrier transport is further addressed in reference [50, 51].

2.4. Ferromagnetism

Ferromagnetism originates from physics in the atomic level. Its underlying mechanism is based on the fact that every electron possesses its own magnetic moment $\vec{\mu}$. The macroscopic magnetization of a material is defined as the vectorial sum of the magnetic moments per unit of volume, mathematically written as

$$\vec{M} = \frac{\sum \vec{\mu}}{V} \tag{2.10}$$

where V is the total volume of the specimen. Ferromagnetic materials present a net magnetic moment $\vec{M}$, even in the absence of an external magnetic field. This collective ordering is due to the Pauli exclusion principle, which forbids two electrons with the same spin to occupy the same quantum state in order to lower the Coulomb repulsion between them. Qualitatively, ferromagnetism can be understood using the first Hund's rule which states that, in order to minimize the energy in the system, one should put as many electrons with spin, say "up" ($n_\uparrow$), into a partially filled atomic orbital before start adding electrons with spin "down" ($n_\downarrow$). In summary, in ferromagnetic materials, it is energetically more favorable for the spins to align in the same direction, i.e, parallel to each other [52].

In transition-metal ferromagnets such as iron (Fe), nickel (Ni), cobalt (Co) and their alloys, the magnetic character originates from a spontaneous and unequal occupation of the density of states (DoS) for spin-up ($n_\uparrow$) and spin-down ($n_\downarrow$) electrons populating the d bands at the Fermi energy. The spin polarization P is defined as:

$$P = \frac{n_\uparrow - n_\downarrow}{n_\uparrow + n_\downarrow} \tag{2.11}$$

Figure 2.10 sketches how spin polarization can be achieved in paramagnetic and ferromagnetic materials. In the case of paramagnetic materials, the population of electrons (density of states) with spin up and spin down is the same (Fig. 2.10a). However, as it will be shown in Sec. 2.2.3, an electrical current can induce spin polarization in paramagnetic materials, as schematically shown in Fig. 2.10b. Note that in this case, the spin polarization is *induced* and will depend on parameters such as the current density (see Eq. (2.6)), contrary to the case of ferromagnetic materials, where the spin polarization is intrinsic, as depicted in Fig. 2.10c.

For the most known ferromagnetic materials, the spin polarizations are found to be Ni = 31%, Co = 42 %, Fe = 45%, $Ni_{81}Fe_{19}$ = 45%, $Co_{84}Fe_{16}$ = 52% [53].

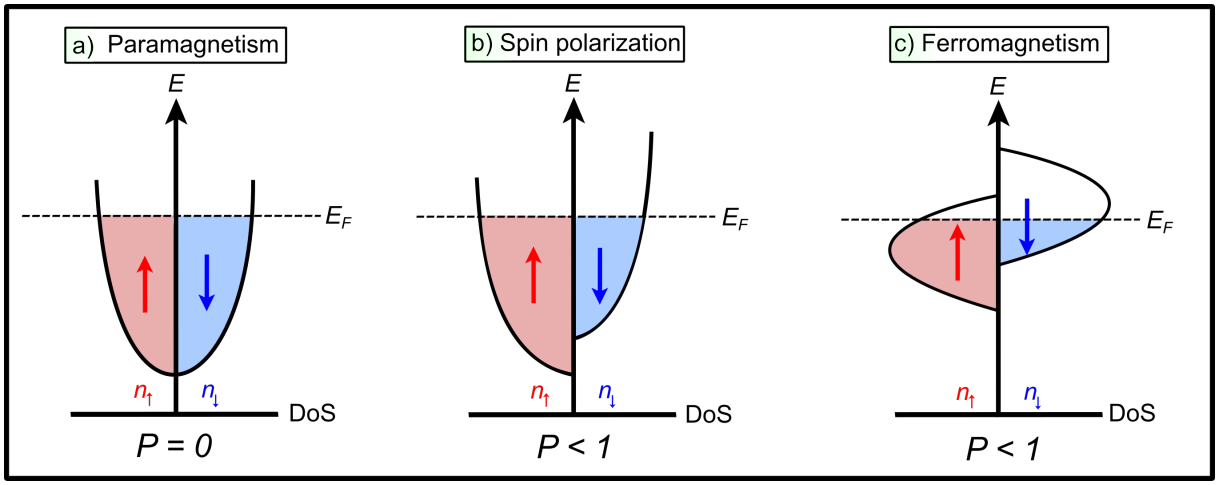

Figure 2.10: a) Ocupation of spin states in paramagnetic materials, E_F is the Fermi energy, P is the spin polarization and red and blue arrows correspond to the density of states for up ($n_\uparrow$) and down ($n_\downarrow$) spins, respectively. Spin polarization in b) paramagnetic and c) ferromagnetic materials.

2.4.1. Anisotropic magnetoresistance and planar Hall effect

Another way to characterize ferromagnetic materials is via magnetotransport measurements. In 1856, William Thomson observed an increase in the longitudinal resistance of ferromagnets for an in-plane magnetic field applied parallel to the electric current, while the resistance decreased for magnetic field applied perpendicular to the current [52, 54]. This effect, called anisotropic magnetoresistance (AMR), can be mathematically formulated em terms of resistivity as [3]:

$$\rho_{xx} = \rho_\perp + (\rho_\parallel - \rho_\perp)\cos^2(\phi) \tag{2.12}$$

where ϕ is the angle between the current and the in-plane magnetic field, and $\rho_\parallel$ and $\rho_\perp$ are the resistivities for magnetic field parallel and perpendicular to the electrical current, respectively. The AMR has a periodicity of $\phi = 180$ degrees and its amplitude can reach values up to 2 % in $Ni_{80}Fe_{20}$ [52].

There is also a corresponding tranverse resistivity, ρ_{xy}, known as planar Hall effect (PHE) [55], mathematically formulated as [56]:

$$\rho_{xy} = (\rho_\parallel - \rho_\perp)\sin\phi\cos(\phi) \tag{2.13}$$

The origin of AMR (or PHE) in most 3d ferromagnets is thought to be dominated by the spin-orbit coupling which mixes the scattering rates between the electrons in the s- and d-bands of the ferromagnet. In simple words, since the SO term is proportional to $\vec{L}\cdot\vec{S}$, the spin dipole moment (S) is aligned by the external magnetic field which, via SOC, results in an isotropic

charge distribution for $L = 0$. For $L \neq 0$, the non-spherical charge distribution leads to different scattering cross-sections for the conduction electrons (electric current) as the relative orientation of the current and the magnetic field changes [52]. Although AMR (or PHE) is common in ferromagnets and it will be used in combination with ferromagnetic resonance to quantify the amplitude of the spin-orbit torques studied in this thesis (see Chap. 3), Chap. 4 will discuss the observation of this effect in non-magnetic 3D topological insulators and its possible origins.

2.4.2. Ferromagnetic resonance - FMR

Ferromagnetic resonance (FMR) is one of the most common ways to determine the properties of ferromagnetic materials. This method was first introduced by Griffiths in 1936 [57] and later formulated mathematically by Kittel [58, 59]. With this technique, several properties of the most known ferromagnets and multilayer structures could be studied [60]. In this section, the discussion of ferromagnetic resonance will be kept on a fundamental level and in the context of thin ferromagnetic films.

The magnetization dynamics of thin ferromagnets can be investigated using the macrospin approximation, which assumes that the magnetization of a thin film remains spatially uniform during its motion and can be treated as a single macrospin. The magnetization vector is expressed as $\vec{m}(t) = \frac{\vec{M}(t)}{M_s}$, where M_s is the saturation magnetization. Mathematically, the magnetization dynamics of ferromagnets can be described using the Landau–Lifshitz–Gilbert (LLG) equation, given by [61–63]:

$$\dot{\vec{m}} = -\gamma \vec{m} \times \vec{H}_{eff} + \alpha \vec{m} \times \dot{\vec{m}} \tag{2.14}$$

where γ is the gyromagnetic ratio defined as $\gamma = \frac{g\mu_B}{\hbar} = 1.76 \times 10^{11}\ \mathrm{s^{-1}\,T^{-1}}$ [64] and H_{eff} the effective magnetic field.

The first term in the Eq. (2.14) describes the magnetization vector precession around the effective magnetic field, as sketched in Fig. 2.11a. The effective magnetic field considers not only the external magnetic field but also intrinsic additional contributions such as the exchange, magnetoelastic and anisotropy fields [52].

In the absence of external forces, the magnetization will precess indefinitely around the effective magnetic field (or equilibrium direction). However, due to relaxation processes, the magnetization vector will relax in a spiral motion until it aligns itself collinearly to H_{eff}, as sketched in Fig. 2.11b. The relaxation mechanisms are embedded into a phenomenological and dimensionless parameter α, known as Gilbert damping parameter [62]. The damping term is an important parameter to quantify changes in the magnetization dynamics due to several effects, such as the absorption of microwaves.

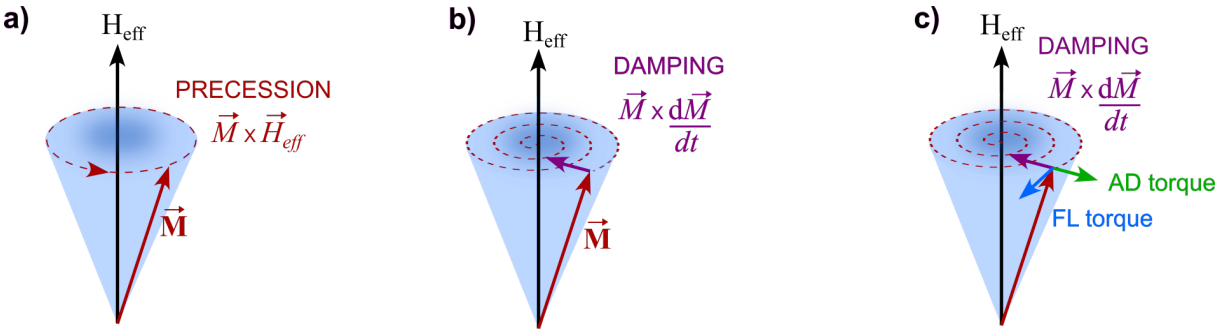

Figure 2.11: Precession of the magnetization $\tilde{M}$ in the a) absence and b) presence of a damping term proportional to $\tilde{M} \times d\tilde{M}/dt$. c) Magnetization dynamics in the presence of anti-damping (AD) and field-like (FL) torques (see next section).

In typical FMR experiments, an oscillating magnetic field H_{rf} is applied perpendicular to the static magnetic field H_{eff}. The oscillating magnetic field H_{rf} has frequencies in the GHz-range, i.e., microwave frequencies. Hence, the magnetization will acquire a vector component perpendicular to H_{eff}. When microwave radiation is absorbed resonantly by a ferromagnet thin film, the magnetization will be tilted out of its equilibrium condition and precess around the effective field H_{eff}. In other words, H_{rf} leads to a torque in the magnetization vector.

In order to resonantly excite the magnetization precession, the microwave frequency ω has to match the precession frequency ω_0, given by [59]:

$$\omega = \omega_0 = \gamma \mu_0 M_{eff} \tag{2.15}$$

where M_{eff} is the effective magnetization. Charles Kittel showed that the resonance condition depends on the shape of the ferromagnet [59]. Since the ferromagnetic structures investigated in Chap. 3 (see Sec. 3.4.3) have dimensions length l = width $w = 20$ μm and thickness $d = 25$ nm, the ferromagnetic slab can be approximated to an infinite plane and the resonance condition is defined as [59]:

$$f = \frac{\mu_0}{2\pi} \sqrt{H_{ext}(H_{ext} + M_s)} \tag{2.16}$$

where H_{ext} is the external static in-plane magnetic field and M_s is the saturation magnetization. This approximation is valid under the condition $H_{ext} = H_{eff}$, which is valid for materials with small magnetic anisotropy, such as $Ni_{80}Fe_{20}$ studied in Chap. 3 in this thesis.

There are two possibilities to fulfill the resonance condition for precession to occur. The first consists in keeping the frequency ω of the H_{rf} fixed and vary the eigenfrequency ω_0 of the magnetization by applying an increasing static magnetic field H_{ext}. The second way is to keep the static magnetic field fixed and change the frequency of the oscillatory field. When ω coincides

with ω_0 of the magnetization, (or experimentally, $H_{rf} = H_{ext}$) the absorption of the microwave field will be maximized.

The absorption of microwaves by the magnetization can be determined by measuring how much of the RF radiation was transmitted and reflected at the resonance condition and it can be detected by changes in the magnetic permeability of the ferromagnetic material. The magnetic permeability (or susceptibility) is dependent on the Gilbert damping parameter and, as will be seen in Chap. 3, has the shape of a Lorentzian peak. Hence, changes in the magnetic susceptibility of the ferromagnetic material cause additional reflection and absorption of the microwave radiation which can be determined by analyzing the Lorentzian shape of the transmitted RF radiation. The master thesis from Christian Jünger [65] offers a comprehensive description of the experimental setup used for the investigations in Chap. 3 and how one can perform analysis of the Lorentzian lineshapes in order to extract physical quantities.

2.5. Spin-transfer torques (STT)

As it will be also seen in Chap. 3, a spin-polarized current can cause changes in the magnetic state of a ferromagnet and, in case its amplitude is significative, it can cause the magnetization to switch [66]. First proposed by Berger [67] and Slonczewski in 1996 [68], spin-transfer torques occur in devices that exhibit non-collinear magnetizations.

Consider an electric current flowing through the multilayers sketched in Fig. 2.12. In this figure, "blue" and "red" layers represent ferromagnets (FM) 1 and 2, respectively, and the middle "empty" part a nonmagnetic spacer layer. The magnetization of FM1 is fixed/pinned (often dubbed as reference layer) and the magnetization of FM2 can freely change its direction (free or recording layer). As the current flows through the multilayers, the reference ferromagnet FM1 polarizes the current in the direction of the magnetization (large blue arrow) which then enters the nonmagnetic layer. It is important to note that the thickness of the spacer layer must be thinner than the spin-diffusion length (a few hundred nanometers for Copper at T = 10 K [69]), so that the current can still be spin-polarized when it enters the second ferromagnet. After passing through the spacer layer, this current of electric charge *and* spin-angular momentum reaches the second ferromagnet (FM2), where the spins aligned non-collinearly with the magnetization are absorbed by the background magnetization, exerting a torque on it. This is the concept of spin-transfer torque. The main message of this section is that the magnetic state of a ferromagnet can be modified by spin-polarized currents, as already addressed in the introduction section of this thesis. This change appears in the form of magnetization oscillations or even in the switching of the magnetization in ferromagnets, as it will be discussed in Chap. 3.

In order to describe spin-transfer torques mathematically, the LLG equation (Eq. (2.14)) can be modified by adding an extra term introduced by Slonczewski in 1996 [68]. The Landau-Lifschtz-

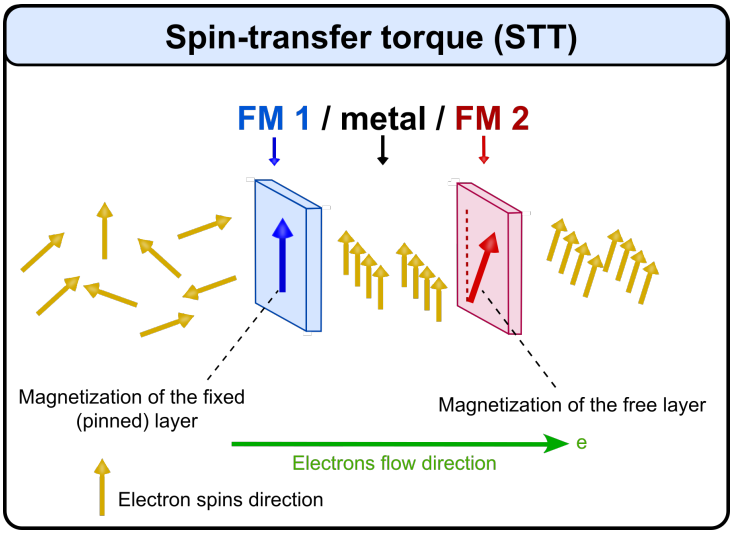

Figure 2.12: Spin-transfer torque mechanism: a reference ferromagnetic layer (FM1) with fixed magnetization serves as a polarizer for the electron spins flowing from one side to the other. The polarized current then flows through a metallic layer and finally reaches the free ferromagnetic layer (FM2), where the spins are absorbed by its magnetization exerting a torque on it.

Gilbert-Slonczewski (LLGS) equation is then given by:

$$\dot{\vec{m}} = -\gamma \vec{m} \times \vec{H}_{eff} + \alpha \vec{m} \times \dot{\vec{m}} + \tau_{stt} \tag{2.17}$$

where τ_{stt} is the spin-transfer torque term.

The LLGS equation has three terms: (i) precession of the magnetization around the effective field, (ii) relaxation of the magnetization towards its equilibrium position, where its magnitude depends on the damping parameter α and (iii) a torque term τ_{stt} that is directly proportional do the spin-polarization and acts as an anti-damping term when the Gilbert damping and the spin-torque align along the same axis but in opposite directions. Chapter 3 will show the LLGS equation can be applied in the context of spin-orbit torques generated by topological insulators.

As conceived by Slonczewski, the torque term can have two components, one in-plane and one out-of-plane. The in-plane torque is known as the Slonczweski torque or “anti-damping” (AD) torque and the out-of-plane torque is called “field-like” (FL) torque. The effect of spin-transfer torque can be viewed as either increasing or decreasing the amplitude of the magnetic precession, as illustrated in Fig. 2.11c.

The basic concepts briefly reviewed in this section will be discussed in more detail in Chap. 3, where the spin polarization generated in the topological surface states of 3D HgTe TI will be used to manipulate the magnetization of a ferromagnet using the FMR technique.

References

[1] G. Dresselhaus, "Spin-Orbit Coupling Effects in Zinc Blende Structures," *Physical Review*, vol. 100, no. 2, pp. 580–586, 1955.

[2] Y. A. Bychkov and E. I. Rashba, "Oscillatory effects and the magnetic susceptibility of carriers in inversion layers," *Journal of Physics C: Solid State Physics*, vol. 17, pp. 6039–6045, 1984.

[3] T. R. Mcguire and R. I. Potter, "Anisotropic Magnetoresistance in Ferromagnetic 3D Alloys," *IEEE Transactions on Magnetics*, vol. 11, no. 4, pp. 1018–1038, 1975.

[4] M. Z. Hasan and C. L. Kane, "Colloquium: Topological insulators," *Reviews of Modern Physics*, vol. 82, no. 3045, 2010.

[5] X. L. Qi and S. C. Zhang, "Topological insulators and superconductors," *Reviews of Modern Physics*, vol. 83, no. 1057, 2011.

[6] A. Manchon, J. Železný, I. M. Miron, T. Jungwirth, J. Sinova, A. Thiaville, K. Garello, and P. Gambardella, "Current-induced spin-orbit torques in ferromagnetic and antiferromagnetic systems," *Reviews of Modern Physics*, vol. 91, no. 035004, 2019.

[7] T. Ihn, *Semiconductor Nanostructures: Quantum states and electronic transport*. Oxford: Oxford, 2010.

[8] R. Winkler, *Spin-Orbit Coupling Effects in Two-Dimensional Electron and Hole Systems*. Springer Berlin Heidelberg, 2003.

[9] V. M. Edelstein, "Spin polarization of conduction electrons induced by electric current in two-dimensional asymmetric electron systems," *Solid State Communications*, vol. 73, no. 3, pp. 233–235, 1990.

[10] J. E. Hirsch, "Spin Hall Effect," *Physical Review Letters*, vol. 83, no. 9, pp. 1834–1837, 1999.

[11] E. I. Rashba, "Properties of semiconductors with an extremum loop. 1. Cyclotron and combinational resonance in a magnetic field perpendicular to the plane of the loop," *Soviet Physics, Solid State*, vol. 2, no. 1109, 1960.

[12] E. I. Rashba, "Semiconductors with a loop of extrema," *Journal of Electron Spectroscopy and Related Phenomena*, vol. 201, pp. 4–5, 2015.

[13] G. Bastard, *Wave Mechanics Applied to Semiconductor Heterostructures*. Les Editions de Physique, 1988.

[14] F. Vas'ko, "Spin splitting in the spectrum of two-dimensional electrons due to the surface potential," *Zh. Eksp. Teor. Fiz.*, vol. 30, no. 9, pp. 574–577, 1979.

[15] J. Luo, H. Munekata, F. F. Fang, and P. J. Stiles, "Observation of the zero-field spin splitting of the ground electron subband in gasb-inas-gasb quantum wells," *Physical Review B*, vol. 38, no. 14, pp. 10142–10145, 1988.

[16] B. Das, D. C. Miller, S. Datta, R. Reifenberger, W. P. Hong, P. K. Bhattacharya, J. Singh, and M. Jaffe, "Evidence for spin splitting in $In_xGa_{1-x}As/In_{0.52}Al_{0.48}As$ heterostructures as B→0," *Physical Review B*, vol. 39, no. 2, pp. 1411–1414, 1989.

[17] S. LaShell, B. A. McDougall, and E. Jensen, "Spin splitting of an Au(111) surface state band observed with angle resolved photoelectron spectroscopy," *Physical Review Letters*, vol. 77, no. 16, pp. 3419–3422, 1996.

[18] G. Nicolay, F. Reinert, S. Hüfner, and P. Blaha, "Spin-orbit splitting of the L-gap surface state on Au(111) and Ag(111)," *Physical Review B*, vol. 65, no. 033407, pp. 1–4, 2002.

[19] F. Reinert, G. Nicolay, S. Schmidt, D. Ehm, and S. Hüfner, "Direct measurements of the L-gap surface states on the (111) face of noble metals by photoelectron spectroscopy," *Physical Review B*, vol. 63, no. 115415, pp. 1–7, 2001.

[20] J. Nitta, T. Akazaki, H. Takayanagi, and T. Enoki, "Gate control of spin-orbit interaction in an inverted $In_{0.53}Ga_{0.47}As/In_{0.52}Al_{0.48}As$ heterostructure," *Physical Review Letters*, vol. 78, no. 7, pp. 1335–1338, 1997.

[21] P. D. King, R. C. Hatch, M. Bianchi, R. Ovsyannikov, C. Lupulescu, G. Landolt, B. Slomski, J. H. Dil, D. Guan, J. L. Mi, E. D. Rienks, J. Fink, A. Lindblad, S. Svensson, S. Bao, G. Balakrishnan, B. B. Iversen, J. Osterwalder, W. Eberhardt, F. Baumberger, and P. Hofmann, "Large Tunable Rashba Spin Splitting of a Two-Dimensional Electron Gas in Bi_2Se_3," *Physical Review Letters*, vol. 107, no. 096802, pp. 1–5, 2011.

[22] Y. S. Gui, C. R. Becker, N. Dai, J. Liu, Z. J. Qiu, E. G. Novik, M. Schäfer, X. Z. Shu, J. H. Chu, H. Buhmann, and L. W. Molenkamp, "Giant spin-orbit splitting in a HgTe quantum well," *Physical Review B*, vol. 70, no. 115328, pp. 1–5, 2004.

[23] E. Ivchenko and G. Pikus, "New photogalvanic effect in gyrotropic crystals," *Soviet Journal of Experimental and Theoretical Physics Letters*, vol. 27, no. 11, p. 604, 1978.

[24] A. Aronov, Y. Lyanda-Geller, G. Pikus, and D. Parsons, "Spin polarization of electrons by an electric current," *Sov. Phys. JETP Letters*, vol. 73, no. 3, pp. 537–541, 1991.

[25] P. Gambardella and I. M. Miron, "Current-induced spin-orbit torques," *Philosophical Transactions of the Royal Society A: Mathematical, Physical and Engineering Sciences*, vol. 369, pp. 3175–3197, 2011.

[26] K. V. Klitzing, G. Dorda, and M. Pepper, "New method for high-accuracy determination of the fine-structure constant based on quantized hall resistance," *Physical Review Letters*, vol. 45, no. 6, pp. 494–497, 1980.

[27] J. D. Thouless, M. Kohmoto, M. P. Nightingale, and M. den Nijs, "Quantized Hall conductance in a two dimensional periodic potential," *Physical Review Letters*, vol. 49, no. 6, pp. 405–408, 1982.

[28] J. E. Avron, D. Osadchy, and R. Seiler, "A topological look at the quantum hall effect," *Physics Today*, vol. 56, no. 8, p. 38, 2003.

[29] F. D. M. Haldane, "Model for a Quantum Hall Effect without Landau Levels: Condensed-

Matter Realization of the "Parity Anomaly"," *Physical Review Letters*, vol. 61, no. 18, pp. 2015–2018, 1988.

[30] C. L. Kane and E. J. Mele, "Z_2 topological order and the quantum spin hall effect," *Physical Review Letters*, vol. 95, no. 146802, pp. 1–4, 2005.

[31] B. A. Bernevig, T. L. Hughes, and S.-C. Zhang, "Quantum Spin Hall Effect and Topological Phase Transition in HgTe Quantum Wells," *Science*, vol. 314, no. 5806, pp. 1757–1761, 2006.

[32] M. König, S. Wiedmann, C. Brüne, A. Roth, H. Buhmann, L. W. Molenkamp, X.-l. Qi, and S.-c. Zhang, "Quantum Spin Hall Insulator State in HgTe Quantum Wells," *Science*, vol. 318, no. 5851, pp. 766–771, 2007.

[33] L. Fu, C. L. Kane, and E. J. Mele, "Topological insulators in three dimensions," *Physical Review Letters*, vol. 98, no. 106803, pp. 1–4, 2007.

[34] J. E. Moore and L. Balents, "Topological invariants of time-reversal-invariant band structures," *Physical Review B*, vol. 75, no. 121306(R), pp. 1–4, 2007.

[35] R. Roy, "Topological phases and the quantum spin Hall effect in three dimensions," *Physical Review B*, vol. 79, no. 195322, pp. 1–5, 2009.

[36] D. Hsieh, D. Qian, L. Wray, Y. Xia, Y. S. Hor, R. J. Cava, and M. Z. Hasan, "A topological Dirac insulator in a quantum spin Hall phase," *Nature*, vol. 452, pp. 970–974, 2008.

[37] J. Chu and A. Sher, *Physics and Properties of Narrow Gap Semiconductors*. Springer, 2008.

[38] C. Brüne, C. X. Liu, E. G. Novik, E. M. Hankiewicz, H. Buhmann, Y. L. Chen, X. L. Qi, Z. X. Shen, S. C. Zhang, and L. W. Molenkamp, "Quantum Hall effect from the topological surface states of strained bulk HgTe," *Physical Review Letters*, vol. 106, no. 126803, pp. 1–4, 2011.

[39] C. Brüne, C. Thienel, M. Stuiber, J. Böttcher, H. Buhmann, E. G. Novik, C. X. Liu, E. M. Hankiewicz, and L. W. Molenkamp, "Dirac-screening stabilized surface-state transport in a topological insulator," *Physical Review X*, vol. 4, no. 041045, pp. 1–6, 2014.

[40] D. M. Mahler, J. B. Mayer, P. Leubner, L. Lunczer, D. Di Sante, G. Sangiovanni, R. Thomale, E. M. Hankiewicz, H. Buhmann, C. Gould, and L. W. Molenkamp, "Interplay of Dirac Nodes and Volkov-Pankratov Surface States in Compressively Strained HgTe," *Physical Review X*, vol. 9, no. 031034, pp. 1–8, 2019.

[41] A. Pfeuffer-Jeschke, *Bandstruktur und Landau-Niveaus quecksilberhaltiger II-VI Heterostrukturen*. PhD thesis, Universität Würzburg, 2000.

[42] E. O. Kane, "Band structure of indium antimonide," *Journal of Physics and Chemistry of Solids*, vol. 1, pp. 249–261, 1957.

[43] E. N. Adams, "Some consequences of possible degeneracy of energy bands in Ge," *Physical Review*, vol. 92, pp. 1063–1064, 1953.

[44] G. Dresselhaus, A. F. Kip, and C. Kittel, "Spin-orbit interaction and the effective masses of holes in germanium," *Physical Review*, vol. 95, no. 2, pp. 568–569, 1954.

[45] X. C. Zhang, A. Pfeuffer-Jeschke, K. Ortner, V. Hock, H. Buhmann, C. R. Becker, and G. Landwehr, "Rashba splitting in n-type modulation-doped HgTe quantum wells with an inverted band structure," *Physical Review B*, vol. 63, no. 245305, pp. 1–8, 2001.

[46] E. G. Novik, A. Pfeuffer-Jeschke, T. Jungwirth, V. Latussek, C. R. Becker, G. Landwehr, H. Buhmann, and L. W. Molenkamp, "Band structure of semimagnetic $Hg_{1-y}Mn_yTe$ quantum wells," *Physical Review B*, vol. 72, no. 035321, pp. 1–12, 2005.

[47] P. Leubner, *Strain-engineering of the Topological Insulator HgTe.* PhD thesis, Julius-Maximilians-Universität Würzburg, 2016.

[48] T. Skauli and T. Colin, "Accurate determination of the lattice constant of molecular beam epitaxial CdHgTe," *Journal of Crystal Growth*, vol. 222, pp. 719–725, 2001.

[49] A. Jost, M. Bendias, J. Böttcher, E. Hankiewicz, C. Brüne, H. Buhmann, L. W. Molenkamp, J. C. Maan, U. Zeitler, N. Hussey, and S. Wiedmann, "Electron-hole asymmetry of the topological surface states in strained HgTe," *Proceedings of the National Academy of Sciences of the United States of America*, vol. 114, no. 13, pp. 3381–3386, 2017.

[50] D. Mahler, *Surface states of the topological insulator and Dirac semi-metal strained HgTe.* PhD thesis, Julius-Maximilians-Universität Würzburg, 2020.

[51] D. M. Mahler, V. L. Müller, C. Thienel, J. Wiedenmann, W. Beugeling, H. Buhmann, and L. W. Molenkamp, "Massive and topological surface states in tensile strained HgTe." 2020.

[52] R. C. O'Handley, *Modern magnetic materials: principles and applications.* New York: Wiley, 1999.

[53] D. J. Monsma and S. S. Parkin, "Spin polarization of tunneling current from ferromagnet/Al_2O_3 interfaces using copper-doped aluminum superconducting films," *Applied Physics Letters*, vol. 77, pp. 720–722, 2000.

[54] W. Thomson, "On the Electro-dynamic Qualities of Metals: Effects of Magnetization on the Electric Conductivity of Nickel and of Iron," *Proc. Royal Soc. Lond.*, vol. 8, pp. 546–550, 1857.

[55] C. Goldberg and R. E. Davis, "New galvanomagnetic effect," *Physical Review*, vol. 94, no. 5, pp. 1121–1125, 1954.

[56] J. P. Jan, *Solid State Physics, Vol. 5.* Academic Press Inc., New York, 1957.

[57] J. H. E. Griffiths, "Anomalous High-frequency Resistance of Ferromagnetic Metals," *Nature*, vol. 158, pp. 670–671, 1946.

[58] C. Kittel, "Interpretation of anomalous larmor frequencies in ferromagnetic resonance experiment," *Physical Review*, vol. 71, no. 4, pp. 270–271, 1947.

[59] C. Kittel, "On the theory of ferromagnetic resonance absorption," *Physical Review*, vol. 73, no. 2, pp. 155–161, 1948.

[60] D. L. Mills and S. M. Rezende, *Spin Dynamics in Confined Magnetic Structures II.* Springer, Topics in Applied Physics, 2003.

[61] L. Landau and E. Lifshitz, "On the theory of the dispersion of magnetic permeability in ferromagnetic bodies," *Phys. Zeitsch. der Sow.*, vol. 8, pp. 153–169, 1935.

[62] T. L. Gilbert, "A Lagrangian Formulation of the Gyromagnetic Equation of the Magnetization Field," *Phys. Rev.*, vol. 100, p. 1243, 1955.

[63] T. L. Gilbert, "A phenomenological theory of damping in ferromagnetic materials," *IEEE Transactions on Magnetics*, vol. 40, no. 6, pp. 3443–3449, 2004.

[64] M. V. Costache, M. Sladkov, C. H. Van Der Wal, and B. J. Van Wees, "On-chip detection of ferromagnetic resonance of a single submicron Permalloy strip," *Applied Physics Letters*, vol. 89, no. 192506, pp. 1–4, 2006.

[65] C. Jünger, *Spin Pumping in the Topological Insulator HgTe.* Master thesis, Julius-Maximilians-Universität Würzburg, 2015.

[66] S. Fukami, T. Anekawa, C. Zhang, and H. Ohno, "A spin-orbit torque switching scheme with collinear magnetic easy axis and current configuration," *Nature Nanotechnology*, vol. 11, pp. 621–625, 2016.

[67] L. Berger, "Emission of spin waves by a magnetic multilayer traversed by a current," *Physical Review B*, vol. 54, no. 13, pp. 9353–9358, 1996.

[68] J. C. Slonczewski, "Current-driven excitation of magnetic multilayers," *Journal of Magnetism and Magnetic Materials*, vol. 159, pp. L1–L7, 1996.

[69] E. Villamor, M. Isasa, L. E. Hueso, and F. Casanova, "Contribution of defects to the spin relaxation in copper nanowires," *Physical Review B*, vol. 87, no. 094417, pp. 1–5, 2013.

3

Spin-orbit torques generated by the 3D TI HgTe

The relativistic spin-orbit coupling is understood to play a fundamental role in enabling the generation of spin-polarized currents in nonmagnetic metals and semiconductors [1–3]. This current of charge and spin can be transferred to an adjacent ferromagnet exerting a spin-orbit torque (SOT) on it, which opens up new opportunities to manipulate the magnetization of the ferromagnetic layer in spintronic devices and to substitute conventional charge-based microelectronic devices to devices based on spin functionalities. The figure of merit in the SOT scheme is the "charge-to-spin conversion efficiency", which enables the classification of which are promising material candidates for such applications. Topological insulators are predicted to be ideal candidates to generate spin-polarized currents due to the robust locking between the momentum and spin of the carriers flowing in the topological surface states[4]. In this chapter, we evaluate if the 3D topological insulator HgTe is a potential candidate to generate torques in ferromagnets by using the spin-transfer torque ferromagnetic resonance (ST-FMR) technique, followed by a detailed description of the device fabrication and the mathematical modelling of the magnetization dynamics of a ferromagnetic material under the action of spin torques. Finally, the perspectives for future investigations of spin-orbit torques using HgTe topological insulator is presented.

3.1. Generating spin-polarized currents in 3D topological insulators

As mentioned in the introduction chapter, topological insulators are good candidates for the generation of spin-polarized currents because of the rigid locking between spin and momentum of the electrons travelling in the topological surface states, as sketched in Fig. 3.1a. The robustness of the spin-momentum locking against impurity scattering enables metallic transport without significant spin relaxation or, in other words, the spin information is maintained even after a large number of scattering events.

It has been predicted that spin accumulation in topological insulators can be obtained by applying an electric field (or flowing an electric current) on the surface of a three-dimensional topological insulator [4]. Similarly to the situation described in Sec. 2.2.3, the electrons in the Fermi surface are accelerated in the direction of the field and more forward going electron states are occupied than backward going states. This generates an electric current that, due to the spin-momentum locking, is accompanied a non-equilibrium surface spin accumulation as sketched in Fig. 3.1b. In this example, a current flowing in the x-direction generates a spin accumulation in the y-direction.

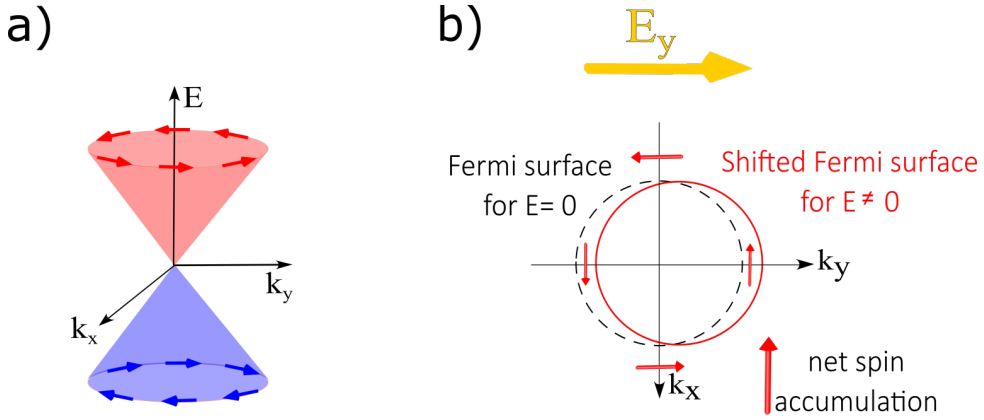

Figure 3.1: a) Linear energy dispersion relation of a massless Dirac particle, where the red and blue arrows represent the spins in the topological top and bottom surfaces, respectively. b) Sketch of the mechanism by which an electric field E applied on the topological surface states generate a non-equilibrium spin density (or spin accumulation) due to the rigid coupling between spin and momentum of the carriers.

At equilibrium, the spin expectation value of the electrons occupying the surface states vanishes, however, the application of an electric field leads to non-equilibrium transport and, therefore, to a finite spin expectation value. For a current flowing, say, in the y-direction $j_y = nev_F$, the amplitude of the *density* spin accumulation is given by:

$$s_x = \frac{\hbar}{2ev_F} j_y \tag{3.1}$$

Here, in order to be able to describe the nature of the SOTs, the torques arising from the application of an electric field to an interface with broken inversion symmetry will be dubbed as *inverse spin galvanic effect (iSGE)* SOTs.

3.2. Physics of SOTs in 3D topological insulators

In topological insulators, spin-orbit torques originate from the spin density generated locally at the interface between the TI and the FM. The non-equilibrium spin density generated on the surface of the topological insulator transfers angular momentum to the magnetization of the ferromagnet via an exchange term, given by $(\Delta/2)\hat{\sigma}\cdot\vec{m}$, where Δ is an exchange coupling energy corresponding to the exchange between the itinerant carriers spins and the localized magnetic moments of the ferromagnet. In contrast, in the SOTs generated by the spin Hall effect, a spin current flows from the normal metal into the ferromagnet. In this context, the low-energy Hamiltonian for topological insulators can be written as:

$$\hat{H} = v\hat{\sigma}\cdot(\vec{p}\times\hat{z}) + (\Delta/2)\hat{\sigma}\cdot\vec{m} \tag{3.2}$$

It is important to note that this model can only be applied if the Dirac states are preserved.

The spin-orbit torques $\vec{T}$ are often interpreted as an effective magnetic field acting on the magnetization of the ferromagnetic material and have the general form:

$$\vec{T} = \Delta\vec{m}\times\vec{s} \tag{3.3}$$

Due to spin-momentum locking, in topological insulators the non-equilibrium spin density is often aligned perpendicular to the direction of the electric field, being proportional to $\vec{s}\propto\hat{z}\times\vec{E}$ and, therefore, Eq. (3.3) is proportional to:

$$\vec{T}\propto\vec{m}\times(\hat{z}\times\vec{E}) \tag{3.4}$$

Equation (3.4) already provides some insight on the nature of the SOT generated by topological insulators. This torque, which acts out of the plane defined by the magnetization (field-like torque), resembles the Oersted torques. Indeed, Ndiaye et. al. showed that the SOTs in topological insulators possesses both in-plane (known as damping-like torque) and out-of-plane components of the form [5]:

$$\vec{T} = \tau_{FL}\vec{m}\times\vec{s} + \tau_{DL}m_z\vec{m}\times(\hat{z}\times\vec{s}) \tag{3.5}$$

where m_z is the out-of-plane component of the magnetization, τ_{FL} and τ_{DL} are the field-like and damping-like torques, respectively. In that work, it is argued that the damping-like torque (which is proportional to the out-of-plane magnetization component m_z) disappears when the

magnetization lies in the plane of the surface and, therefore, the torques caused by topological insulators should be out-of-plane. This theoretical prediction is in stark contrast with SOT-FMR measurements performed in Bi-families topological insulators. This discrepancy is often attributed to the significant parallel bulk conductivity in these systems that changes the symmetry of the SOTs and to the alteration of the surface of the topological insulator due to orbital hybridization with the ferromagnetic metal.

It is also important to highlight that the form of torques presented in Eq. (3.5) have a similar symmetry with the torques arising from the SHE, however, while the SOTs in topological insulators arise from an exchange interaction between electron spins in the TSS and the magnetization, SHE-SOTs arise from the *absorption* of angular momentum coming from a spin-current generated via the SHE. Due to interfacial effects and other contributions to the torque, there is not much point in trying to disentangle the origin of both spin-current origins [6].

Lastly, several experimental studies assume that torques associated with absorption or transfer of spin angular momentum have a dissipative character (anti-damping torque), while torques arising from the iSGE are field-like torques. Again, these assumptions should be analyzed with caution, since effects such as interband transitions, spin relaxation/precession can significantly provide other contributions to the SOTs. In this case, symmetry alone cannot directly separate the iSGE- and SHE-SOTs, but they remain a powerful tool to qualitative and phenomenologically describe the spin-orbit torques.

Given the challenges and drawbacks in the interpretation of the SOTs presented in this section, 3D HgTe TI provides a reasonable platform to investigate SOTs since one of the key features of this system is the absence of bulk conductivity and electrical transport dominated by the topological surface states. Combined with state-of-art device fabrication techniques, some of the drawbacks pointed out in this section can be excluded and/or minimized and will be described in this chapter.

The next section deals on how to obtain a mathematical description of the SOTs in terms of realistic experimental parameters.

3.3. Spin-torque Ferromagnetic Resonance - Theory

This section aims to introduce calculations based on the Landau–Lifshitz–Gilbert–Slonczewski (LLGS) equation, which describes the magnetization dynamics of a ferromagnetic material under the action of spin torques and external magnetic fields. The amplitudes of the torques are introduced in Sec. 3.3.1. In Sec. 3.3.2, the response of the magnet due to the current-induced spin-torques, i. e., the generation of a DC mixed voltage, is derived. The calculations follow a similar procedure as introduced in [7].

3.3.1. FMR amplitude under the action of spin-torques

In order to investigate the current-induced spin torques exerted in the magnetization of the ferromagnetic material, one needs to understand how the LLGS equation can be applied to the topological insulator/ferromagnet (TI/FM) bilayer. For this purpose, the coordinate system depicted in Fig. 3.2 is used. In this system, the unprimed coordinates are constructed based on the orientation of the external magnetic field aligned in the y-direction, so that the average magnetization is oriented predominantly in this direction. The primed coordinates give the orientation of the sample geometry, where the RF current flows in the y'-direction. In the HgTe layer, the orange arrow represents the current flowing through this layer and the red arrows oriented in the x'-direction represent the spins of the top topological surface state oriented perpendicular to the current direction (due to spin-momentum locking). The spins orientation of the bottom topological surface state are not depicted in this figure.

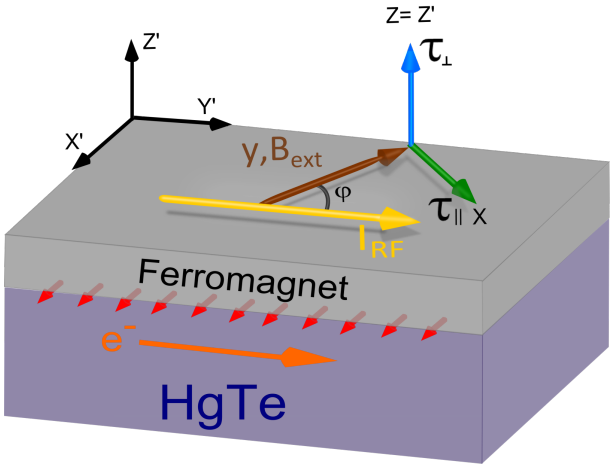

Figure 3.2: Sketch of the reference system used for the topological insulator/ferromagnet bilayer. The current flows through the device in the y'-direction and the external magnetic field B_{ext} is applied in the y-direction. The red arrows in the HgTe layer depict the spin from the top topological surface states. In this figure, the spins of the bottom topological surface state are not depicted. The green and blue arrows represent the torques applied in the plane and out of the plane of the ferromagnetic material, respectively.

As already introduced in Sec. 2.5, when angular momentum is transferred to a ferromagnetic material, its magnetization will oscillate, producing changes in the magnetoresistance of the ferromagnet. This spin torque on the magnetization can be observed at the resonance condition as a change in the microwave absorption and/or linewidth of the ferromagnetic material. For a ferromagnetic thin film with in-plane magnetization, the resonance frequency is given by $\omega_0^2 = \gamma^2 B_{ext}(B_{ext} + \mu_0 M_{eff})$, where ω_0 is the resonance frequency, γ is the gyromagnetic ratio and M_{eff} is the effective saturation magnetization (see Sec. 2.4.2 for an introduction to FMR). By assuming an applied magnetic field and magnetization almost entirely in the y-direction and also assuming that fields arising from shape anisotropy or crystalline anisotropy are negligible, the magnetization unit vector $\vec{m}$ can be written as:

$$\vec{m}(t) = \frac{\vec{M}(t)}{M_s} = m_x(t)\hat{x} + \hat{y} + m_z(t)\hat{z} \tag{3.6}$$

where M_s is the saturation magnetization and $\hat{z}$ is the direction normal to the film plane.

The generalized LLGS describing the magnetization dynamics under the action of torques is given by:

$$\dot{\vec{m}} = -\gamma \vec{m} \times \vec{H}_{eff} + \alpha \vec{m} \times \dot{\vec{m}} + \tau_x \hat{x} + \tau_z \hat{z} \tag{3.7}$$

where γ is the gyromagnetic ratio ($1.76 \times 10^{11}\,\mathrm{s^{-1}T^{-1}}$), H_{eff} the effective magnetic field τ_x and τ_z are the torques applied in the $\hat{x}$ (in-plane) and $\hat{z}$ (out-of-plane) directions, respectively. The effective magnetic field H_{eff} in Eq. (3.6) is the sum of the external and demagnetization fields, written as $\vec{H}_{eff} = \vec{H}_{ext} - \hat{m} \cdot \hat{z} M_{eff} \hat{z}$.

The in-plane torque τ_x is along the $\vec{m} \times (\vec{x}' \times \vec{m})$ direction, while the torque out-of-plane, τ_z, is along the $(\vec{x}' \times \vec{m})$ direction. One should also notice that the Oersted field created by the current flowing through the bilayer will also generate a torque in the same direction as τ_z, being an additional contribution to the already described out-of-plane torque.

BBy adding the H_{eff} term and solving for x and z component, the LLGS equation can be written as:

$$\begin{cases} m_x = \gamma m_z (H_{ext} + M_{eff}) + \alpha(\frac{dm_z}{dt}) + \tau_x \hat{x} \\ m_z = -\gamma m_x H_{ext} - \alpha(\frac{dm_x}{dt}) + \tau_z \hat{z} \end{cases} \tag{3.8}$$

where α is the damping parameter.

Assuming torques of the form $m_x = m_{x0} e^{i\omega t}$ and ignoring higher frequency components, the two equations for the moment in x and z directions are expressed as:

$$m_{x0} = \frac{i\omega(\alpha\tau_{z0} + \tau_{x0}) + \gamma(H + M_{eff})\tau_{z0}}{\gamma^2 H^2 + \gamma H(\gamma M_{eff} + 2i\alpha\omega) - \omega(\alpha^2\omega - i\alpha\gamma M_{eff} + \omega)} \tag{3.9}$$

$$m_{z0} = -\frac{\gamma H\tau_{x0} + i\omega(\alpha\tau_{x0} - \tau_{z0})}{\gamma^2 H^2 + \gamma H(\gamma M_{eff} + 2i\alpha\omega) - \omega(\alpha^2\omega - i\alpha\gamma M_{eff} + \omega)} \tag{3.10}$$

where $H = H_{ext}$. The equation above can be simplified by considering that the applied radiofrequency current excites the FMR dynamics with a small angle precession, i.e., the deflection angle of M from the equilibrium position is small, resulting in a small damping parameter, so that the approximation $\alpha^2 << 1$ can be valid. In this case, the approximation $\alpha\dot{\tau} = i\alpha\omega\tau_i \approx 0$ can be made. The small angle approximation also implies that higher order in torques can be neglected.

By taking these approximations into account, Eqs. (3.9) and (3.10) can be simplified to:

$$m_{x0} = \frac{i\omega\tau_{x0} + \gamma(H + M_{eff})\tau_{z0}}{\gamma H(H + \gamma M_{eff}) + 2i\alpha\gamma\omega(H + M_{eff}/2) - \omega^2} \tag{3.11}$$

$$m_{z0} = -\frac{\gamma H\tau_{x0} - i\omega\tau_{z0}}{\gamma H(H + \gamma M_{eff}) + 2i\alpha\gamma\omega(H + M_{eff}/2) - \omega^2} \tag{3.12}$$

The resonance condition is defined by the Kittel's formula as [8]: $\omega = \gamma\sqrt{H(H + M_{eff})} \equiv \omega_0$. Magnetic field amplitudes H between 0 mT to 300 mT typically give resonance frequencies $f = \frac{\omega}{2\pi}$ up to 10 GHz, indicating these frequencies belong to the radiofrequencies (RF) domain. The extracted parameters are available in Ref. [9]. Thus, Eqs. (3.11) and (3.12) can be rewritten as:

$$m_{x0} = \frac{i\omega\tau_{x0} + \gamma(H + M_{eff})\tau_{z0}}{\omega_0^2 - \omega^2 + 2i\alpha\gamma\omega(H + M_{eff}/2)} \tag{3.13}$$

$$m_{z0} = -\frac{\gamma H\tau_{x0} - i\omega\tau_{z0}}{\omega_0^2 - \omega^2 + 2i\alpha\gamma\omega(H + M_{eff}/2)} \tag{3.14}$$

The equations presented in (3.13) and (3.14) define the in-plane and out-of-plane torques, respectively. As already mentioned in the previous section, the in-plane torque τ_x is oriented along the $\vec{m} \times (\vec{x}' \times \vec{m})$ direction (Slonczewski or anti-damping torque). The out-of-plane torque (τ_z) is along the $(\vec{x}' \times \vec{m})$ (field-like torque). Both torques are generated by the spin-accumulation in the topological surface states of the TI, however, the out-of-plane torque encloses contributions from the field-like and Oersted torques. One can estimate the field-like torque amplitude by subtracting the Oersted contribution from the total torque. This matter will be addressed in the

later sections of this chapter.

3.3.2. Mixing voltages

At this point, we were able to write the LLGS equation to the coordinate system sketched in Fig. 3.2, as well as to calculate the in-plane and out-of-plane torques exerted in the magnetization of the ferromagnet. However, in order to quantify the magnitude of the applied torques, one needs to be able to quantify the *response* of the magnetization in terms of realistic experimental parameters. Ferromagnetic materials are well known for presenting a longitudinal resistance that depends on the angle between the electric current I and the magnetization M of the film, the anisotropic magnetoresistance (AMR). As described in Sec. 2.4.1, the resistivity is the largest for external in-plane magnetic field applied parallel to the current direction and can be mathematically expressed by $AMR = R_0 + \Delta R \cos^2(\phi)$. By using ferromagnetic materials in proximity with a topological insulator, the RF current flowing through the bilayer structure will mix with the resistance changes of the ferromagnetic material and generate a mixing voltage.

In the experiment, V_{mix} is obtained from the DC voltage arising from the mixture of the RF current and the resistance oscillations in the ferromagnet. In this situation, the RF current and the oscillating resistance have the same frequency, therefore their product will generate a DC rectified voltage. The RF resistance can be written as $\delta R = \frac{dR}{d\phi}\delta\phi$. The RF current is given by $\delta I = I_{RF}\cos(\omega t)$ and therefore the mixing voltage can be written as:

$$\begin{aligned} V_{mix} &= \langle \delta I \cdot \delta R \rangle = \langle \delta I \cdot \left(\frac{dR}{d\varphi}\right) \cdot \delta\varphi \rangle \\ V_{mix} &= \langle I_{RF}\cos\omega t \cdot \left(\frac{dR}{d\varphi}\right) \cdot Re(m_x) \rangle \end{aligned} \tag{3.15}$$

where $Re\,(m_x)$ is the real part of the torques that, for small excitations, oscillates sinusoidally with a phase and amplitude that varies across the resonance condition and only its real component contributes to the mixing voltage. Taking the contribution from the real parts of m_x and m_z already calculated in Eqs. (3.13) and (3.14), V_{mix} results in:

$$V_{mix} = -\frac{I_{RF}}{2}\left(\frac{dR}{d\varphi}\right)\left(\frac{\gamma\omega^2\alpha\tau_{x0}(2H+M) - \tau_{z0}(H+M)) + \tau_{z0}\gamma^3 H(H+M)^2}{(\omega^2-\omega_0^2)^2 + \alpha^2\gamma^2\omega^2(2H+M)^2}\right) \tag{3.16}$$

The equation above can be written in a general form $V_{mix} = I_{RF}(\frac{dR}{d\phi})[A\tau_{x0} + B\tau_{z0}]$ where A and B are given by:

$$A = \frac{\gamma\omega^2\alpha(2B+\mu_0 M)}{(\omega^2-\omega_0^2)^2+\alpha^2\gamma^2\omega^2(2B+\mu_0 M)^2}$$
$$B = \frac{\gamma^3 B(B+\mu_0 M)^2-\gamma\omega^2(2B+\mu_0 M)}{(\omega^2-\omega_0^2)^2+\alpha^2\gamma^2\omega^2(2B+\mu_0 M)^2} \tag{3.17}$$

Defining $\Delta = \alpha\gamma(2H+M)/2$ as the linewidth of the of the SOT-FMR signal, A and B in Eq. (3.17) can be further simplified and the mixing voltage can be written in the following compact form:

$$V_{mix} = -\frac{I_{RF}}{4}\gamma\left(\frac{dR}{d\varphi}\right)\left[\tau_{x0}\frac{1}{\Delta}F_S(B_{ext}) + \tau_{z0}\frac{\sqrt{1+\frac{M}{H}}}{\Delta}F_A(B_{ext})\right] \tag{3.18}$$

where F_S and F_A are the symmetric and antisymmetric Lorentzians lineshapes as a function of the external magnetic field B_{ext}, respectively. Their responses are written as:

$$F_S(B_{ext}) = \frac{(2\Delta)^2\omega^2}{(\omega^2-\omega_0^2)^2+(2\Delta)^2\omega^2} \tag{3.19}$$

$$F_A(B_{ext}) = \left[\frac{(\omega^2-\omega_0^2)^2}{2\omega\Delta}\right]F_S \tag{3.20}$$

In this way, the symmetric and antisymmetric components of the mixed voltage can also be written in the compact form:

$$V_S = -\frac{I_{RF}}{2}\gamma\left(\frac{dR}{d\varphi}\right)\frac{1}{\alpha\gamma\ (2B+\mu_0 M)}\tau_{x0} \tag{3.21}$$

$$V_A = -\frac{I_{RF}}{2}\gamma\left(\frac{dR}{d\varphi}\right)\frac{\sqrt{1+\frac{M}{H}}}{\alpha\gamma\ (2B+\mu_0 M)}\tau_{z0} \tag{3.22}$$

The result obtained in Eqs. (3.21) and (3.22) is one central theoretical derivations of this chapter. From these equations, the torques in- and out-of-plane can be calculated and their amplitudes depend on a few parameters: the voltage amplitude that can be obtained by fitting the Lorentzian lineshapes (V_S or V_A), the effective magnetization (M) and anisotropic magnetoresistance of the ferromagnet layer ($dR/d\phi$), the external applied magnetic field (B_{ext}), the damping parameter (α) and finally the RF current flowing through the bilayer (I_{RF}). Already from these equations, one can observe that one of the key parameters to determine the spin torques using the FMR technique is that it requires a quantitative determination of the I_{RF} flowing through the HgTe/Py

bilayer, which will depend on the device's impedance and on the RF power losses due to the construction of the measurement setup. It is also worth noting that the out-of-plane torque can also originate from the Oersted field, giving an extra contribution to the out-of-plane torque. A quantification of this type of torque will be derived in the following sections. A brief discussion will also be made on this matter.

The mixing voltage encodes the response of the ferromagnet material from the torques exerted on it. For the purpose of data analysis, the type of torque exerted in the magnetization is important because it presents a different phase relationship between the driven frequency and the magnetic response of the ferromagnetic material. The torques exerted in-plane and out-of-plane directions induce a Lorentzian response and its lineshape depends on the resonance phase δ between the driven force (e.g. field-like or damping-like torque) and the response of the magnetization to the applied torques (e.g. anisotropic magnetoresistance or tunneling AMR). The torque exerted in the plane of the ferromagnet (anti-damping or Slonczewski-like torque) gives a symmetric Lorentzian response:

$$\frac{A}{1+(f-f_0)^2/\Delta_0^2} \tag{3.23}$$

where A is the amplitude, f is the frequency, f_0 is the resonance frequency and Δ_0 is the half-width at half-maximum. The out-of-plane ("field-like") torque, on the other hand, gives an antisymmetric Lorentzian response:

$$\frac{B(f-f_0)/\Delta_0}{1+(f-f_0)^2/\Delta_0^2} \tag{3.24}$$

Figure 3.3 shows a schematic plot of the different lineshapes of the Lorentzian as a function of the driving frequency in the sample.

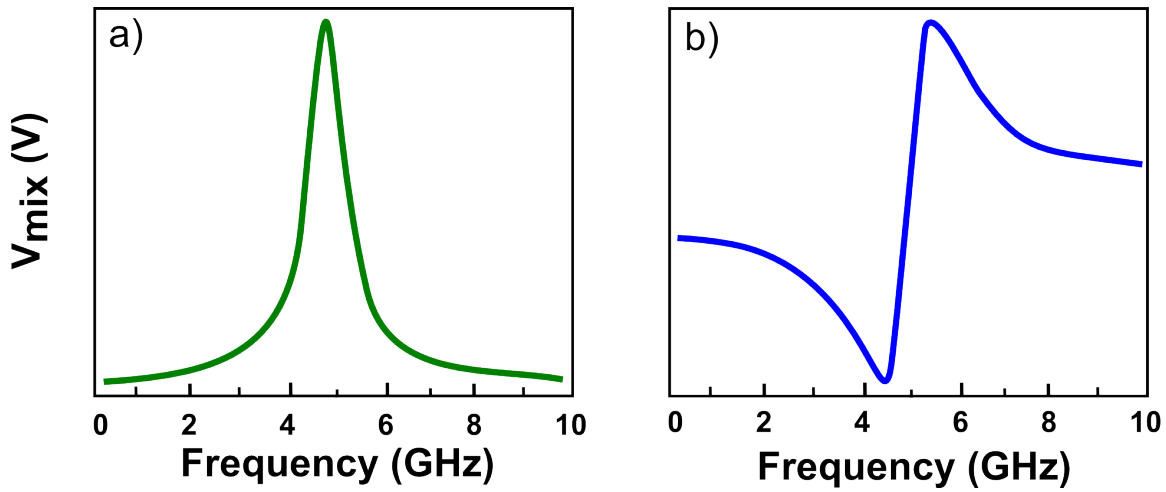

Figure 3.3: Lorentzian lineshapes derived from a) Eq. (3.23) for the symmetric component and b) Eq. (3.24) for the antisymmetric component.

In this case, the analysis of V_{mix} in terms of the symmetric and antisymmetric functions provides information on the torques exerted in the ferromagnet.

3.3.3. Determining SOT conductivities and efficiencies

The spin torque conductivity is determined similarly to the electrical conductivity, given by:

$$\sigma_i = \frac{J_{s,i}}{E} = \frac{J_{s,i} \cdot L}{V} = \frac{J_{s,i} \cdot L}{I_{RF} Z_{RF}} = \tau_i \frac{2e}{\hbar} \frac{M_s t_{mag} L}{I_{RF} Z_{RF} \gamma \cos(\phi)} \tag{3.25}$$

where $J_{s,i}$ the i component (in- or out-of-plane) of the spin current density absorbed by the ferromagnet, E is the amplitude of the electric field, M_s, t_{mag} and L are the saturation magnetization, thickness and length of the ferromagnetic layer, respectively, I_{RF} is the RF current flowing through the TI layer and Z_{RF} is the device impedance.

The spin-torque efficiency (or spin-torque ratio) is the ratio of spin to charge current density in the topological insulator, defined as [7]:

$$\Theta_{s,i} = \frac{J_{s,i}}{J_C} = \frac{\sigma_{s,i}}{\sigma_{active}} = \tau_i \frac{2e}{\hbar} \frac{M_s t_{mag} L}{I_{RF} Z_{RF} \gamma \cos(\phi) \sigma_{active}} \tag{3.26}$$

where σ_{active} is the conductivity of the topological insulator (active) layer and J_C is the charge density.

The contribution from the Oersted field generated by the current flowing in the active layer of the device is

$$\sigma_{Oe} = \frac{e \mu_0 M_s t_{mag} t_{active} \sigma_{active}}{\hbar} \tag{3.27}$$

and its contribution to the spin-torque efficiency is

$$\Theta_{\perp,Oe} = \frac{e \mu_0 M_s t_{mag} t_{active}}{\hbar} \tag{3.28}$$

Having derived the mathematical descriptions of the spin-orbit torques and estimated that the resonance frequencies will be in the RF domain, one needs to fabricate devices with several desired properties. The next section will address the experimental methods used in the SOT investigations.

3.4. Experimental Methods

The fabrication of the spin-orbit torque devices based on 3D HgTe TIs have several details that are crucial to its fabrication. Such details are based on the physics of the SOTs and a detailed description of the device fabrication aims to make the reader aware of how such issues are experimentally addressed in order to obtain an optimized device with the desired properties.

3.4.1. Wafer preparation and mesa etching

The material used for the samples produced in this thesis is named "Q2805" and it consists of a 88 nm thick strained HgTe grown on GaAs substrate. A 55 nm thick bottom layer of (Cd,Hg)Te is placed in between the substrate and the HgTe layer. Note here that the HgTe layer does not have a cap layer. The processing of the sample starts by cleaning its surface with acetone in an ultrasonic bath in order to remove any residuals due to its cleaving. The wafer is cleaved in suitable pieces of (3x3) mm^2. Subsequently, the sample is uniformly coated with liquid photoresist and baked in a hot plate at 50 degrees Celsius, where the resist hardens and solvents partially evaporate. Then, the sample is placed in contact with a partially covered quartz glass mask where the desired pattern is drawn on it. By exposing the resist under a Hg vapor lamp (λ = 365 nm), the pattern is "imprinted" on the sample and the exposed resist parts are solved with a developer. Next, the structure is etched by Argon ion beam etching, where the accelerated ionized atoms (Ar+) hit the parts of the sample surface that are not covered by the resist, leading to the desired removal of the HgTe layer. The process just described is depicted in Figs. 3.4a and 3.4b. For the devices produced in this work, the mesa has two patterns: one of them has the shape of a Hall bar, present in the device for the sample characterization (see Fig. 3.6a). The other pattern consists of two ferromagnetic squares. These squares are the building blocks for the spin torque devices. The Hall bar has a width of W = 80 μm and a length between the longitudinal voltage probe leads L =240 μm.

Figure 3.4: a) Schematics of the CdHgTe and HgTe layers. The HgTe layer has a nominal thickness of t = 88 nm. b) Schematics of remaining structure after dry etching, which is dubbed as "mesa". The mesa has a height $h \approx$ 100 nm.

3.4.2. Tunnel barrier

After the mesa etching, a ferromagnet should be deposited on top of the HgTe mesa. However, as previously discussed in Sec. 3.2, the ferromagnetic material can interdiffuse into the HgTe layer degrading the topological surface states e/or creating an interface with unknown characteristics and making it more challenging to attribute the origin of the SOTs. In order to avoid interdiffusion, a thin diffusion barrier is placed between the HgTe and the ferromagnetic material. This barrier shall have a few properties: a) it cannot be too thick, so that good electrical contact is kept between the HgTe and the ferromagnet and b) it should be thick enough to efficiently prevent interdiffusion. The diffusion barrier is only needed below the ferromagnet, i.e., on top of the mesa. In this work, a thin layer of hafnium oxide HfO_2 of approximately 1 nm was grown via atomic layer deposition (ALD) at 30° Celsius. ALD is a technique based on the alternating sequential use of chemicals (precursors) that react with the surface of a material in self-terminating gas-solid reactions. A typical ALD cycle consists of the following steps:

i) Self-limiting reaction of the first reactant (Reactant A - tetrakis dimethylamino hafnium (TDMAH, $Hf[N(CH_3)_2]_4$)) and the sample surface
ii) Purging with argon ions to remove the reactants that did not react with the surface
iii) Self-limiting reaction of the second reactant (Reactant B - H_2O) to prepare the surface again for the reaction of the first reactant.
iv) Purging step

After depositing HfO via ALD, the insulator is etched away with acetone in ultrasonic agitation. A schematic of the tunnel barrier is depicted in Fig. 3.5 and it has dimensions of (80 x 80) μm.

Figure 3.5: Schematics of the HfO tunnel barrier (≈ 1 nm) represented by the red layer covering the HgTe mesa.

3.4.3. Ferromagnetic sputtering

Now that the surface of HgTe is protected against interdiffusion of ferromagnetic material into it, the next step is to sputter Permalloy ($Ni_{0.8}Fe_{0.2}$) on top of the etched mesa. The samples produced for this work have two different ferromagnets in the same device: one (FM1) with dimensions (20 x 20) μm and FM2 with (20 x 10) μm. Both ferromagnets have a thickness t_{FM}= 25 nm. Permalloy (Py) is applied on top of the HgTe mesa by means of sputter deposition, where Py atoms are ejected from the surface of a Py target due to several collisions with Ar atoms. To protect Py from oxidation, a 10 nm-layer of Ruthenium (Ru) is also sputtered in-situ. Since oxidized Ru is conducting, it provides a suitable cap for the Py thin film. A schematic of the structure (mesa + diffusion barrier + ferromagnet) is depicted in Fig. 3.6a.

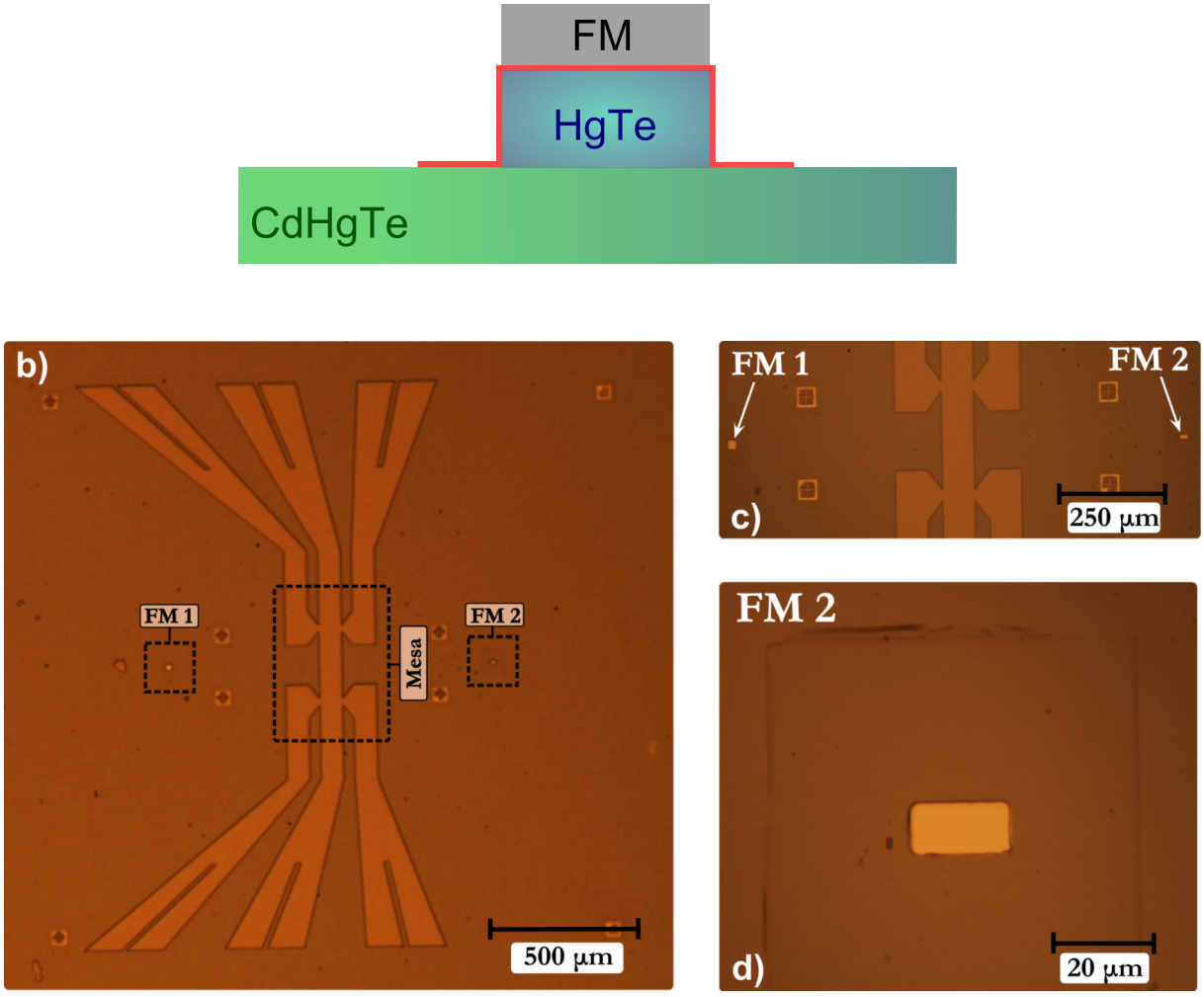

Figure 3.6: a) Schematics of the HgTe mesa covered with sputtered Permalloy (grey) and separated by the HfO diffusion barrier (red). b) Micrograph image of the etched mesa structure. c-d) Zoom in of both ferromagnetic structures present in the device.

Figure 3.6b shows a microscope picture of the real sample indicating the structures described above. Figure 3.6c shows partially the mesa and both ferromagnets zoomed in, while Fig. 3.6d

shows one the ferromagnets, with dimensions (20 x 10) μm. In this figure, one can observe the tunnel barrier (80x 80) μm separating the HgTe from the ferromagnet.

3.4.4. Mesa insulator

The Hall bar insulator is grown via ALD and is composed of three layers: $ZrO_2/HfO_2/Al_2O_3$. Reference [9] gives a detailed description of the need for trilayer insulator processing. The main idea is to use Al_2O_3 to avoid "cracks" in the previously used insulator (SiO_2/Si_2N_3). In order to prevent Al_2O_3 from getting in contact with HgTe, a zirconium oxide (ZrO_2) layer is grown in between. Finally, to protect Al_2O_3 by being etched by the developer (TMAH) in the metallization step, a layer of ZrO_2 is used to protect the Al_2O_3 layer. Lithography tests are described in Ref. [9]. The device shown in Fig. 3.7 does not show the gate insulator, since in this particular device a gate insulator was not used.

3.4.5. Metallization of the Coplanar Waveguide

Before describing the metallization of the coplanar waveguides in the sample fabrication process, it is insightful to present a short introduction on the role of the CPWs in the experiments performed in this thesis, as well as introducing its functioning principle. The next paragraphs offer a short introduction to the CPWs used in this work.

Why using CPWs for STT-FMR measurements?

FMR can be excited by RF magnetic fields (up to 10 GHz) using a coplanar waveguide (CPW), which conceptually consists of a central conductor that carries the current I (signal line), surrounded by two ground plates on ground potential. A current I with a certain amplitude and frequency flowing through the CPW generates a magnetic field according to Ampere's law. This magnetic field has components in-plane and out-of-plane. For the coordinate system displayed in Fig. 3.8 and a RF current I flowing in the $-x$-direction, the generated magnetic field is primarily oriented in the y-direction on top of the signal line. In the gap between the signal and the ground lines, the field is oriented along the z-direction. The employment of a CPW on the experiments performed in this thesis offers several advantages, where the most striking of them is that the topological insulator/ferromagnet bilayer can be accurately inserted into the CPW by means of optical lithography. In this way, oscillating in-plane or out-of-plane magnetic fields can be applied uniformly in the device. Furthermore, electrical contacts (voltage probes) can be connected to the final device, making its measurement straightforward. The other advantage of using CPWs is that a wide range of frequencies can be driven through them. Thus, the frequency dependence of the measured signals can be studied. All measurements presented in this chapter have coplanar waveguides structured on GaAs substrates, with CdTe insulating layers.

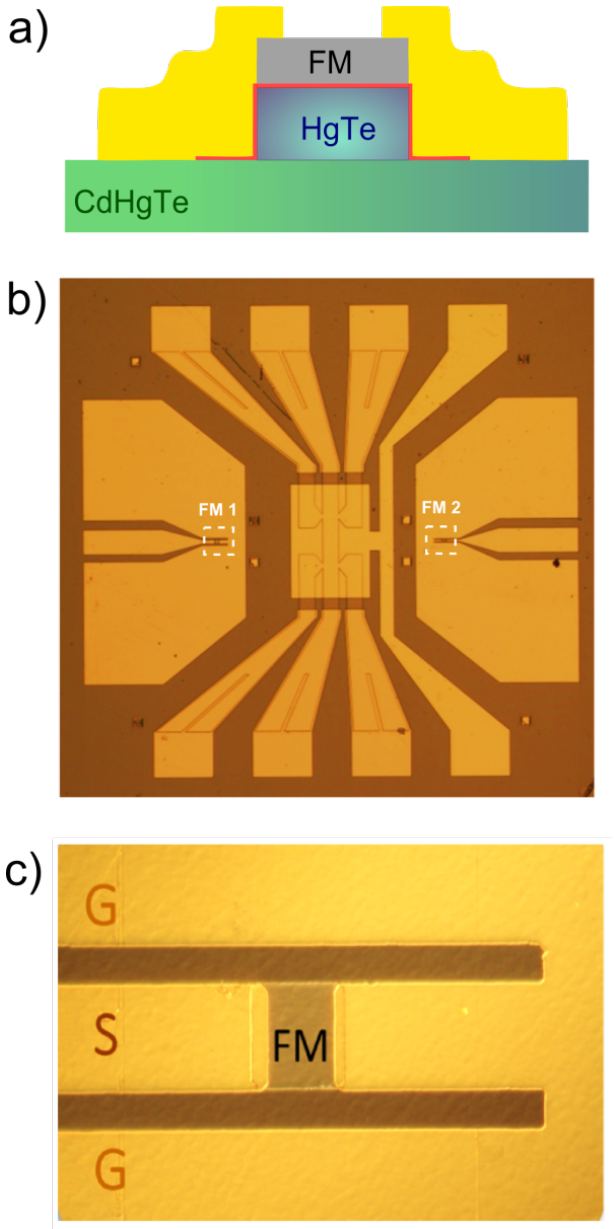

Figure 3.7: a) schematics of the produced layer stack, described from the bottom: CdTe substrate with HgTe mesa (blue/green), HfO diffusion barrier (red), permalloy (grey) and gold metallization of the waveguide (yellow). b) Micrograph image of the whole device, with CPW/FM devices and Hall bar. c) Zoomed in micrograph image of permalloy patterned into the coplanar waveguide.

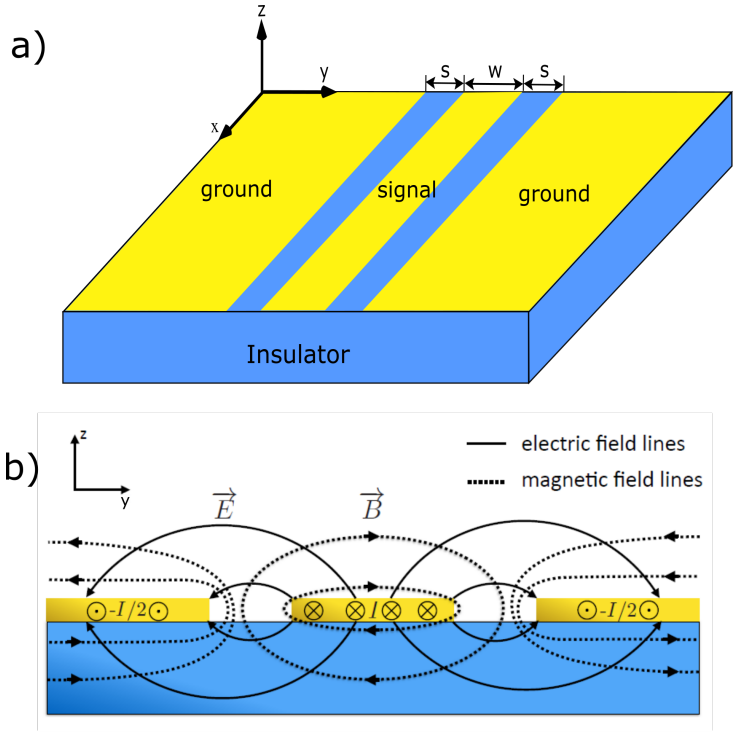

Figure 3.8: a) Schematics of a coplanar waveguide (yellow) on an insulator. The signal line has a width $w = m$. The gap between the signal lines and the ground plates is $s = m$. b) Representation of the electric (solid) and magnetic (dashed) field lines in a CPW for a current flowing in the depicted direction. Figure taken from [9].

Since the AC currents are applied to CPWs, one of the very important points is the propagation of electromagnetic waves through conductors, which can cause losses by reflections when reaching obstacles such as connectors, loads, etc. In this situation, it is important to have the maximum power transferred to the device, so that accurate excitation fields and frequencies can be applied to it. In order to avoid RF power losses and/or reflections while the current is transmitted through the CPW, the waveguide should be designed to have an impedance of 50 Ω, a value that matches the wave propagation impedance of coaxial cables connectors and signal generators used in the experimental setup. This can be done by using the software provided by SONNET. The impedance matching of 50 Ω depends on the geometry of the device, such as the width of the signal line *"w"* and the gap between signal and ground lines *"s"*. Since all cables and RF equipment are conventionally designed for 50 Ohm, this optimal impedance for the CPW can be obtained by using standard available softwares and for the devices investigated in this work, the signal line width $w = 20$ μm and the distance between the signal line and the ground plates is $s = 10$ μm. In the geometry shown in Fig. 3.7b, one notices that the CPW is shorted. Having the sample near the short ensures that the RF electric field is zero at this point, and I and B are maximum.

The CPWs are incorporated into the HgTe/Py layer by means of metallization. This is implemented by evaporating gold (Au) and deposited it on top of the structure defined by a negative

photoresist. In this step, the gate electrodes as well as the electrical contacts for the Hall bars are also metallized. The layer consists of 5 nm of titanium (Ti) and 200 nm of Au, where Ti is used to improve the adhesion of Au to mesa insulator.

3.5. Experimental setup and characterization

The SOT devices fabricated via optical lithography need to be inserted into the cryostat to be characterized and measured. The sample is mounted inside a sample holder (red dashed lines in Fig. 3.9a)) coupled to an insert equipped with the RF cables that is inserted into the cryostat. In order to transmit the RF current, coaxial cables are used. An overview of the measurement stick and the sample holder is shown in Figs. 3.9a) and 3.9b), respectively.

As described in Sec. 3.3.2, the V_{mix} response from the ferromagnet is a rectified DC voltage, which can be detected by a DC voltmeter. However, since the amplitudes of the rectified voltage in the TI/FM bilayer are small, in order to reduce the noise (i.e., in order to increase the signal to noise ratio) of the measurements performed in this work, the lock-in technique was employed. The amplitude of the RF current is modulated by a low frequency (f = 113 Hz) sinusoidal wave signal (see Fig. 3.10b). The low frequency modulating signal is at the same time the reference for the lock-in amplifier and thus, the response of the device can be detected with the phase-locking technique. The V_{mix}, in this case, is not a "pure" DC voltage, but a low-frequency voltage resulting from the modulation of the RF current amplitude.

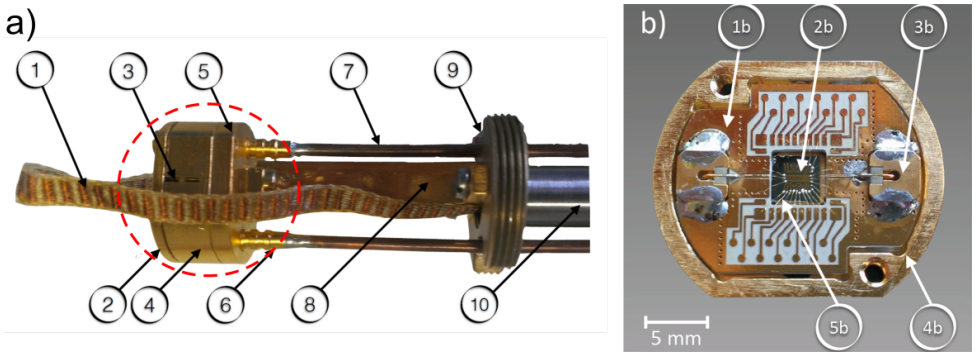

Figure 3.9: a) Picture of the sample holder mounted on the insert. 1 shows the loom copper cables used to contact the sample to measurement equipments. 2, 3, and 4 top and middle part of the sample box with slit, respectively. 5 shows the bottom part of the sample holder and the RF connectors used to connect the PCB through the bottom part of the sample holder are shown in 6. Semi-rigid coaxial cable in 7. Copper extension in 8 screwed on the bottom part of the sample holder and plate 9 with screw-thread. Loom cables inside the tube shown in 10. b) Photograph of the sample holder shown in red dashed lines in a). Holder with PCB 1b, sample 2b, RF connector 3b, bottom plate of sample holder 4b, and bond wires connecting the sample to the box 5b. Figure taken from [9].

In order to apply a RF current and simultaneously detect the low-frequency response of the device (V_{mix}), a bias tee is used in our setup. Conceptually, a bias tee can be viewed as a three-port component, with one low-frequency DC port coupled via an inductor, one RF port coupled via a capacitor, and a combined (RF+DC) port. Thus, the bias tee allows high-frequency signals to pass through the circuit, but it blocks the AC response. The experimental setup used in this work is depicted in Fig. 3.10. This figure shows a microscope image of the lithographically produced device, where the HgTe/FM bilayer is inserted into the signal lines of the coplanar

waveguide. A RF source generates a current with amplitude I_{RF} and frequency f that is guided by the waveguide through the device. The V_{mix} response is measured with the already described standard low-noise lock-in technique.

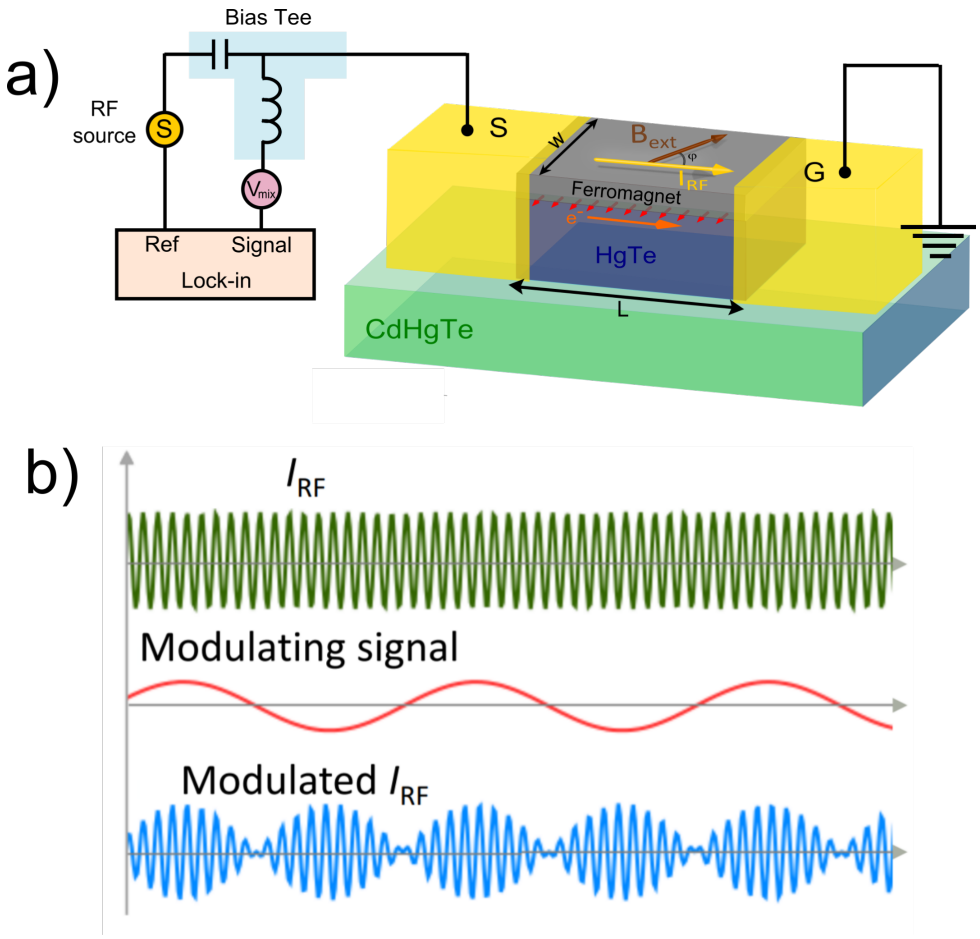

Figure 3.10: a) Schematics of the experimental setup used to study the SOT devices. The circuit includes the device under study, a high-frequency signal generator, a bias tee and a lock-in amplifier. b) Schematics of the technique used to obtain the rectified DC voltages. The I_{RF} from the signal generator (green) is modulated by a signal of lower frequency (red) and the final modulated I_{RF} (blue) is the voltage arriving at the device. Figure b) taken from [10].

3.6. Results and discussion

As mentioned in the fabrication section 3.4, the spin torque samples have two devices (mesa + ferromagnet) in the same chip carrier. Here, the results presented at room-temperature refer to sample "ST7 B" which have dimensions of (20 × 20) μm. The results at $T = 4.2$ K refer to sample "ST7 A" whose dimensions are (20 × 10) μm. Both devices ST7 A and ST7 B have similar properties as the ones described in this thesis. The reader is referred to Refs. [11, 12] for further details on both devices.

3.6.1. Characterization of the FMR setup at room temperature

In order to characterize the produced devices, the frequency dependence of V_{mix} was studied at room temperature (300 Kelvin). The setup used for the experiments is the one described in Fig. 3.10. The amplitude of the RF excitation ("output voltage") is $V = 500$ mV and the angle between the electrical current and the external magnetic is $\phi = -45$ degrees. Figure 3.11a shows a typical measurement of V_{mix} as a function of the in-plane magnetic field for f= 5 GHz. For a magnetic field of $B_{in} = 38$ mT, a resonance is observed. One can perform similar measurements for different frequencies and increasing magnetic field range. The results is shown in Fig. 3.11b, where the external in-plane magnetic field is swept from B_{ext} = (8-150) mT in 3 mT steps and the frequency of the RF current I_{RF} is stepped from f = (2-11) GHz in 100 MHz steps. In this figure, the color code indicates the amplitude of the V_{mix} normalized with respect to each frequency maximum value. Figure 3.11b also shows that the amplitude of V_{mix} decreases at higher frequencies and this can be explained by the higher attenuation of the RF current at high frequencies REF.

The magnetic properties of the the ferromagnet can be extracted by fitting the resonance field for different frequencies and model it using the Kittel equation [8], given by:

$$f = \frac{\mu_0 \gamma}{2\pi} \sqrt{H_{ext}(H_{ext} + M_s)} \tag{3.29}$$

Equation (3.29) is valid under the assumption that $H_{eff} \approx H_{ext}$. This is justified for materials with a small magnetic anisotropy ($H_{aniso} \approx 0$). This model also assumes that the magnetization of the ferromagnet can be described in a macrospin picture.

Figure 3.11c shows the frequency f as a function of the extracted resonant magnetic field H_r, i.e., the magnetic field at which the ferromagnet is in resonant condition. From the Kittel fit, the gyromagnetic ratio γ and the saturation magnetization M_s can be extracted. These parameters give a good indication of the quality of the ferromagnetic film. From the fit shown in Fig. 3.11c,

the following values are found:

$$\begin{aligned} 4\pi M_{s,B} &= (412 \pm 23) \text{ mT} \\ \gamma_B &= (240 \pm 5.3) \text{ GHz T}^{-1} \end{aligned} \tag{3.30}$$

where the index "B" indicates these values correspond to the device ST7 B.

The values for the saturation magnetization M_s found for the other device in the chip carrier, ST7 A, is smaller compared to ST7 B device, while the gyromagnetic ratio γ is similar for both devices:

$$\begin{aligned} 4\pi M_{s,A} &= (331 \pm 29) \text{ mT} \\ \gamma_A &= (266 \pm 10) \text{ GHz T}^{-1} \end{aligned} \tag{3.31}$$

where the index "A" indicates these values correspond to the device ST7 A.

The errors in both the M_s and γ arise from the uncertainty (minimum to maximum) estimation of possible fits. The measured values of the gyromagnetic ratio in this work is in good agreement with the values reported in the literature for permalloy [13]. On the other hand, the saturation magnetization M_s is reported to be around $M_s \approx 1$ T, which does not fit the values found in this work, even with a large uncertainty. This discrepancy may indicate inhomogeneities in the sputtered Permalloy or that the magnetic field used (≈ 70 mT) was not enough to reach the saturation magnetization (M_s).

3.6.2. FMR analysis at $T = 4.2$ K

A similar procedure as the one implemented in the previous section is performed at $T = 4.2$ K in the device ST7 A. The amplitude of the RF excitation is $V = 600$ mV and the angle between the electrical current and the external magnetic is $\phi = -45$ degrees. The external in-plane magnetic field is swept from $B_{ext} = (0\text{-}300)$ mT in 5 mT steps and the frequency of the RF current I_{RF} is stepped from $f = (2\text{-}13)$ GHz in 100 MHz steps. In this figure, the color code also indicates the amplitude of the V_{mix} normalized with respect to its maximum value. The results are shown in Fig. 3.12. The behavior observed in Fig. 3.12 is similar to the one observed in Fig. 3.11b. By perfoming a Kittel fit, the extrated values of the saturation magnetization and the gyromagnetic ratio for this device are:

$$\begin{aligned} 4\pi M_{s,A} &= (1201 \pm 297) \text{ mT} \\ \gamma_A &= (162 \pm 19) \text{ GHz T}^{-1} \end{aligned} \tag{3.32}$$

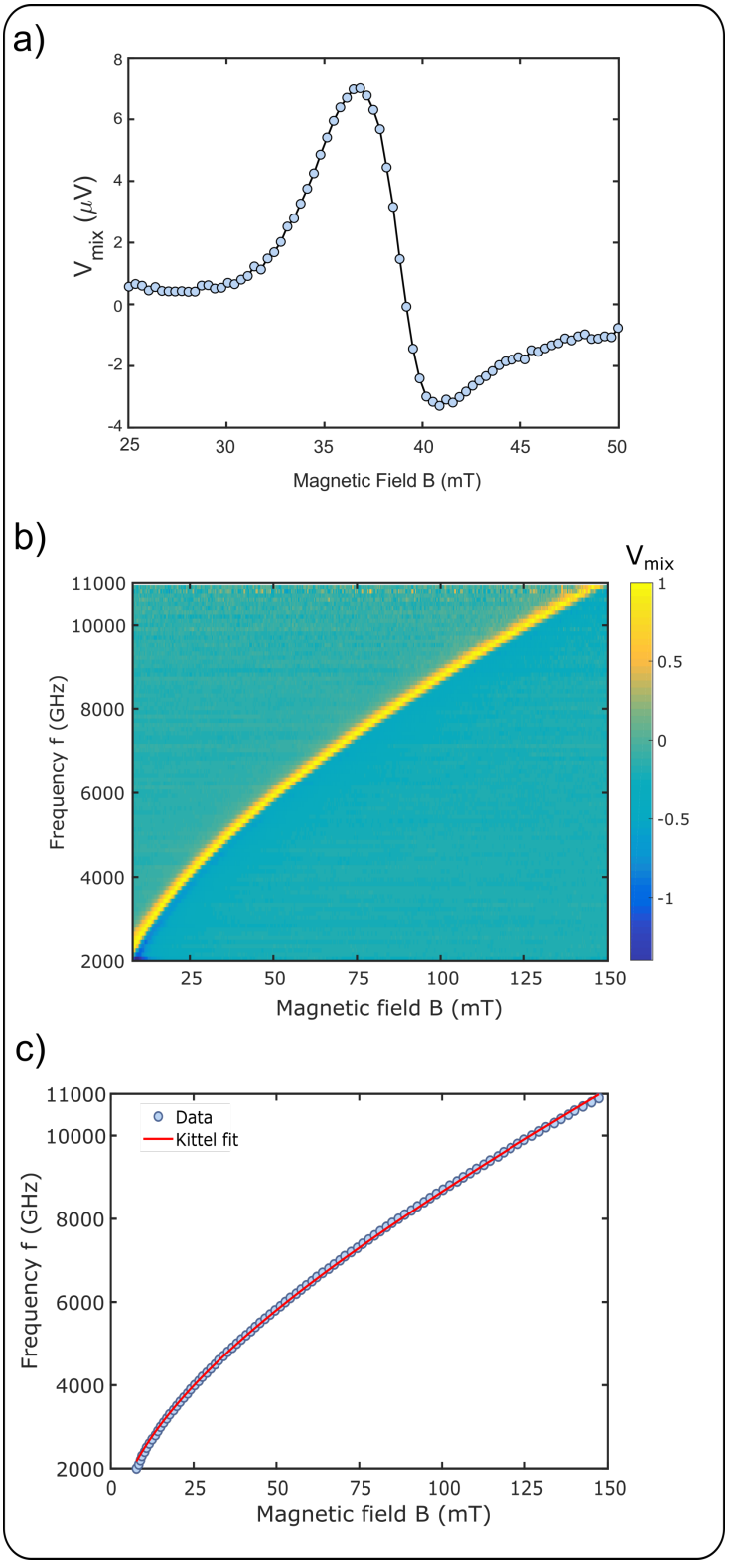

Figure 3.11: a) Measured mixing voltage V_{mix} at room-temperature at a frequency $f = 5$ GHz and $\phi = -45$ degrees. b) Frequency dependence of normalized V_{mix} amplitude as a function of the in-plane magnetic fied for an angle $\phi = -45$ degrees. c) Measured resonance frequency from b) and corresponding fits with Kittel formula (Eq. (3.29)).

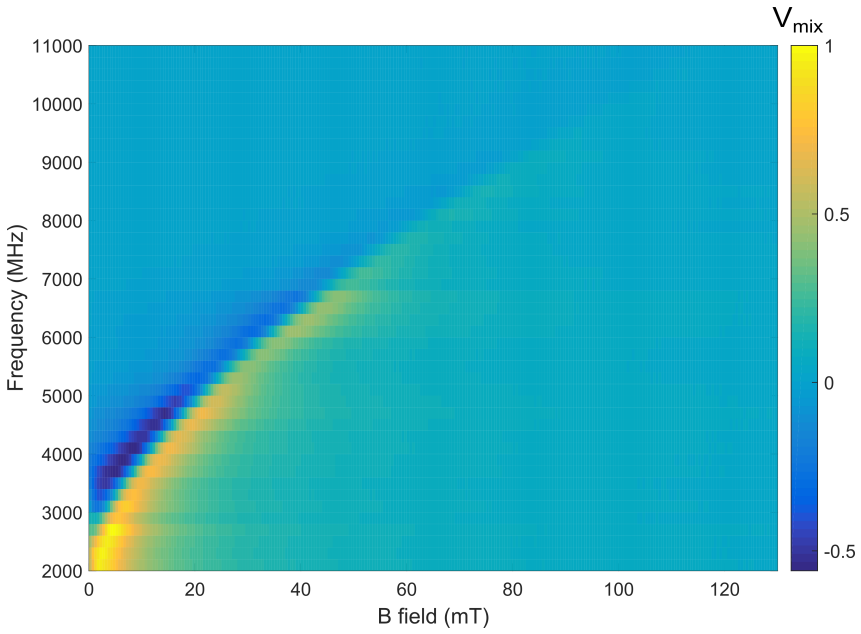

Figure 3.12: Frequency dependence of normalized V_{mix} amplitude as a function of the in-plane magnetic fied for an angle $\phi = -45$ degrees.

These values are in good agreement with the literature and, in comparison with the measurements performed at room temperature, it might indicate that the saturation magnetization M_s can be better determined at higher magnetic fields. These measurements establish that the devices investigated in this work present the standard properties of ferromagnetic materials and are, therefore, suitable for further studies.

Figure shows V_{mix} as a function of the in-plane magnetic field for a frequency $f = 6$ GHz. One can obtain the symmetric and anti-symmetric components of the mixing voltage by fitting such a curve with Eqs. (3.19) and (3.19), respectively. Both components lead to the in-plane and out-of-plane torques computed by Eq. (3.21) and Eq. (3.22), respectively. The extracted parameters will be discussed in Sec. 3.7.

3.6.3. Angular dependence of V_{mix}

In order to analyze in more detail the symmetries of the in-plane and out-of-plane spin-orbit torques using the SOT-FMR technique, angular dependence measurements of V_{mix} were performed. Figure 3.14 shows the angular dependence of the mixing voltage V_{mix} separated into symmetric and antisymmetric components at a temperature $T = 4.2$ Kelvin and an excitation voltage in the output of the voltage source of $V = 1.7$ Volts. Here $\phi = 90$ degrees mean that current and magnetic field are perpendicular to each other.

At a first glance, this angular dependence seems to be rather complicated, however, it can be partially understood from the contribution arising from the AMR of the ferromagnet. Since the

AMR in these materials is written as $R(\phi) = R_0 + \Delta R \cos^2(\phi)$ (where ΔR means the difference in the resistance between current parallel and perpendicular to the in-plane magnetic field), it follows that the AMR term contributes with the dependence $\frac{dR}{d\phi} \propto \cos(\phi)\sin(\phi)$. The current-induced torques arising from the spin Hall effect/inverse Spin Galvanic Effect (anti-damping) or the out-of-plane (field-like) torque due to the Oersted field scale with $\cos(\phi)$.

Since $V_{mix} \propto \frac{dR}{d\phi}\tau$, its angular dependence is given by $V_{mix} \propto \cos^2(\phi)\sin(\phi)$, for both its symmetric and antisymmetric components.

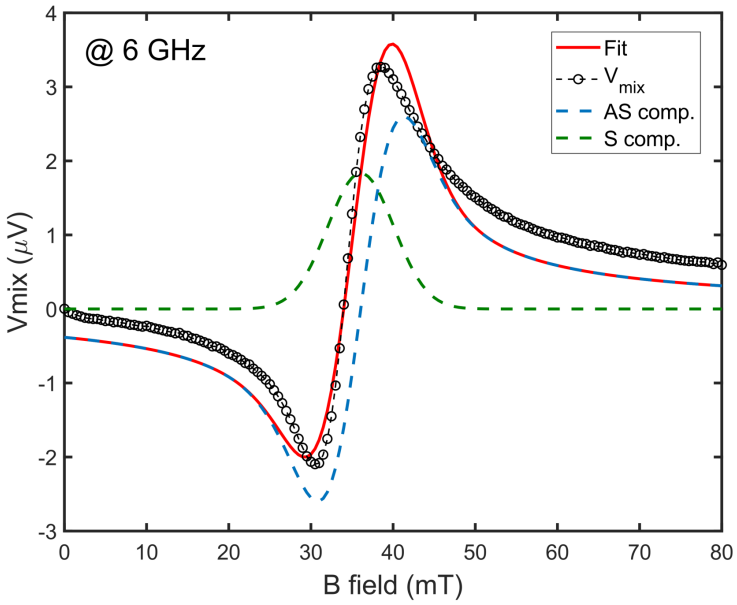

Figure 3.13: Measured mixing voltage V_{mix} at a frequency $f = 6$ GHz, with a typical Lorentzian fit. The symmetric and antisymmetric lineshapes of V_{mix} are depicted in dashed green and blue lineshapes, respectively, while the red curve shows the total fit.

From the angular dependence of V_{mix} at $T = 4.2$ K, one can observe that its anti-symmetric component fits well the predicted angular dependence, indicating that out-of-plane torques are present in the bilayer devices. However, although the amplitudes of the in-plane torque are measurable, its angular dependence does not follow such a prediction. These results are in contradiction with the SOT-FMR measurements performed at low-temperature using Bi_2Se_3 as the topological insulator material, where the in-plane component of the spin-torque is present and it increases with decreasing temperature [14].

This (lack of) angular dependence in the devices measured in this thesis implies that the in-plane torque induced by the spin-polarization in the TSS is absent at low-temperatures or it is contaminated by parasitic effects. Another way to interpret these results is provided in Ref. [5], where it is argued that, due to the nature of the generation of spin-polarized currents (via the inverse spin galvanic effect), the in-plane torque should be absent in topological insulators interfaced with ferromagnetic materials with *in-plane* magnetization. This result only applies

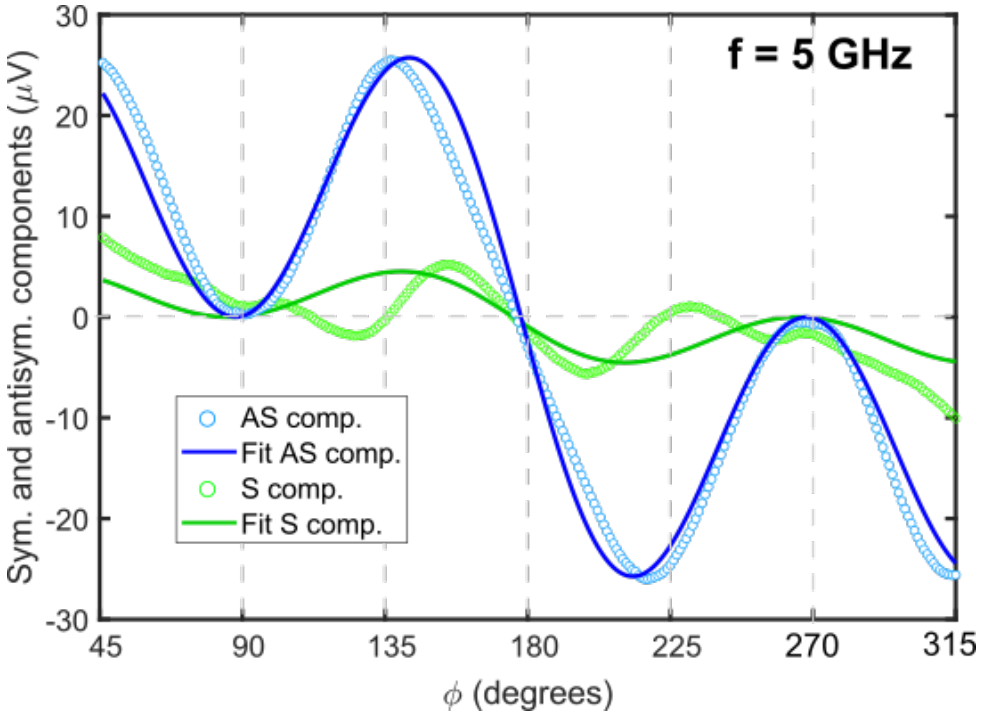

Figure 3.14: Angular dependence of V_{mix} at a frequency $f = 5$ GHz and a temperature $T = 4.2$ K. The data (dots) is fitted by a function $V_{mix} \propto \cos^2(\phi)\sin(\phi)$.

when the Dirac states are preserved in the presence of the adjacent ferromagnetic layer. As described in Sec. 3.4, a layer of HfO was used in between the HgTe and the Py to protect the HgTe surface properties. Thus, it could be reasonable to assume that in-plane torques are absent in our devices as predicted in Ref. [5].

Moreover, Ref. [6] corroborates this argument by mentioning that Bi-family topological insulators show sizable bulk conductivity, suggesting that bulk states might play a role in the in-plane component of the spin-orbit torques generated by topological insulators.

Further insight into the origin of the SOT in the devices investigated in this thesis can be obtained from the measurements of the angular dependence of V_{mix} at room-temperature (300 Kelvin). The measurements were performed in device ST7A at a frequency of $f = 5$ GHz with an excitation voltage of $V = 750$ mV. Figure 3.15 shows the angular dependence of the symmetric and anti-symmetric components of V_{mix}.

The most striking feature in these measurements is that both components have similar amplitudes and that both components follow the expected $\cos^2(\phi)\sin(\phi)$ angular dependence, apart from a phase between them. This result is reproducible in both devices (ST7A and ST7B) [12]. The angular dependence of the symmetric component of V_{mix} is in stark contrast with the measurements performed at $T = 4.2$ K, where *only* the angular dependence of the anti-symmetric component (and therefore the out-of-plane torque) was observed.

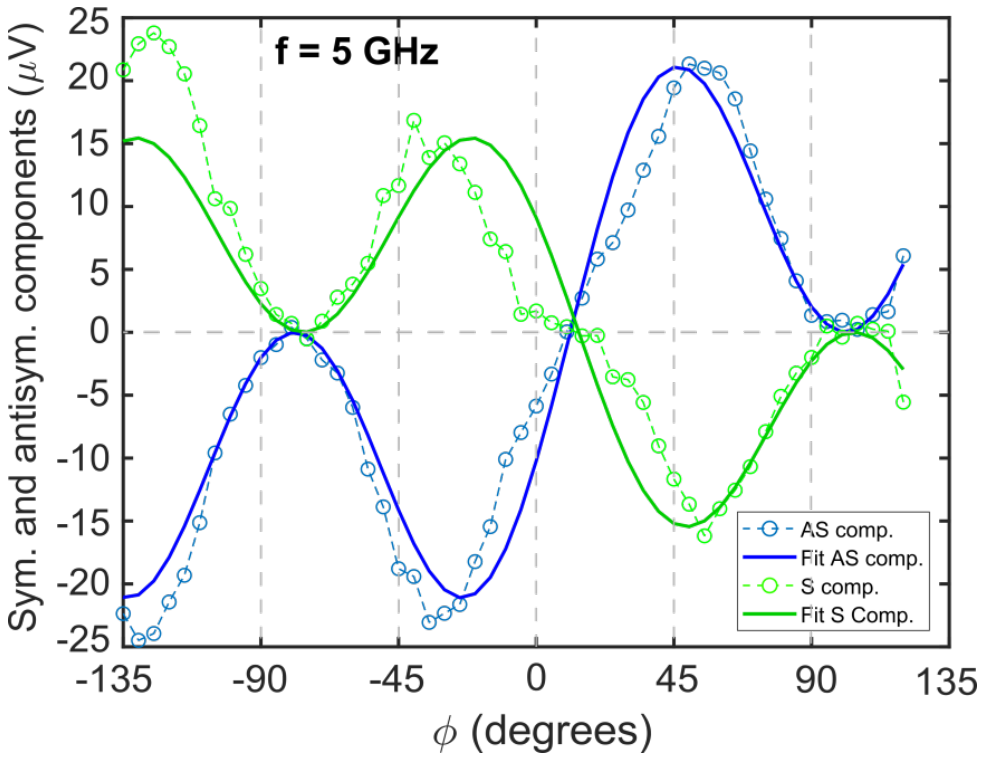

Figure 3.15: Angular dependence of V_{mix} at a frequency $f = 5$ GHz and a temperature $T = 300$ K. The data (dots) is fitted by a function $V_{mix} \propto \cos^2(\phi)\sin(\phi)$.

In the next sections, the spin-orbit torques will be quantified, followed by a discussion of the obtained results.

3.7. Determination of the SOT efficiencies

This section deals with the challenges in determining the electrical current flowing through the HgTe layer. Knowing the electrical current flowing through the HgTe layer is the important parameter in the determination of the SOTs since, as already discussed in the theoretical sections, the spin accumulation is proportional to the amount of charge current flowing through the TI layer. To estimate the charge current/power arriving at the HgTe/Py bilayer, there are several factors that must be considered in the experimental setup, such as the losses of the RF cables and sample holder, the difference in impedance between the CPW and the bilayer and the shunting of the electrical current through the permalloy. Additionally, in the presence of high current densities, thermovoltage effects can compromise the reliable reading of the magnetization state. These parasitic effects are discussed below.

(i) **Attenuation of the RF power due to cables and sample holder**

In order to correctly estimate the RF current flowing through the TI/FM bilayer, one needs to characterize the coaxial cables used to transmit the RF signal because they cause the attenuation of the RF power. After characterizing the losses arising from the RF cables, one can estimate the current arriving at the bilayer. In Ref. [9], the attenuation of the RF lines used in the experiments performed in this thesis was measured at temperatures of $T = 4.2$ K and $T = 300$ K using a vector network analyzer (VNA). A VNA consists of a source used to generate a known signal (reference) and a set of receivers, used to determine changes of the signal caused by the device-under-test (DUT). A signal is used as the input for the DUT and the VNA measures both the signal that is reflected from the input side, as well as the signal that is transmitted to the output side of the DUT. The amount of transmitted and reflected signals depends on the impedance of the DUT. The VNA measures both the reflected and transmitted signals and compares the resulting signal to the reference. The ratio of the transmitted to the reference signal provides a transmission coefficient that indicates the attenuation of the RF cables. The losses on the cables were characterized as a function of the frequency f. Figure 3.16a shows the attenuation for both coaxial lines as a function of the frequency of the RF signal measured at $T = 4.2$ Kelvin and $T = 300$ K, respectively. The attenuation of both cables can be theoretically be described by Eq. (3.12) in [9]. From that work, it was determined that the maximum loss ($f = 20$ GHz) of the coaxial cables is -6.8 dB at $T = 4.2$ Kelvin and -12.8 dB at room temperature. The measurements of the attenuation by RF cables provide the first source of losses of the power arriving at the TI/FM bilayer interface.

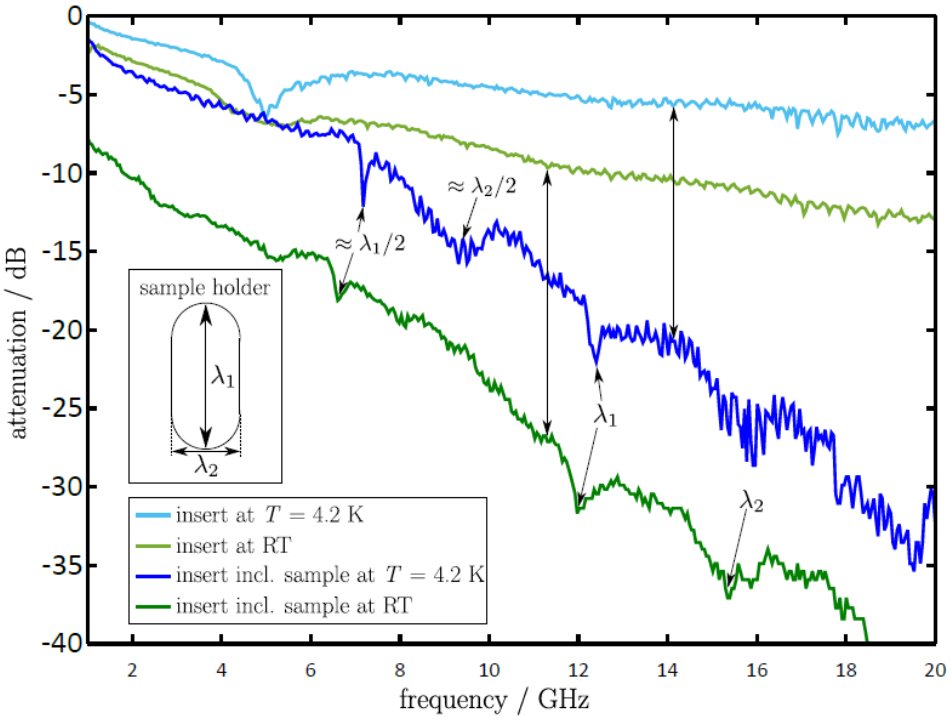

Figure 3.16: Measured attenuation in the frequency range of 1 GHz to 20 GHz at $T = 4.2$K (blue) and RT (green) including sample. Attenuation of the coaxial lines of the insert without the sample for RT (light green) and $T = 4.2$K (light blue). Arrows indicating the difference between the attenuation of the insert to insert including sample for both temperatures. Inset with scheme of sample holder. Figure taken from [9].

(ii) **Resistivity mismatch between the HgTe and Py layers**

Another factor that influences the amount of current flowing through the HgTe/Py bilayer, and especially through the HgTe layer, is the fact that the permalloy thin film is more conductive than HgTe and, therefore, most of the current flowing through the device will be shunted through the ferromagnet (see the quantitative analysis below). This indicates that at the bilayer interface, most of the electrical current will be shunted through the Py layer and the spin accumulation generated by the topological insulator surface states will be reduced. A precise quantification of the resistivity of the topological insulator is rather cumbersome because it requires knowing its average value at the interface between HgTe and Permalloy. This is hard to determine since the addition of the Permalloy on top of HgTe could cause bend bending of the bands. Reference [7] approaches this issue by mimicking the band-bending effects of the permalloy on top of Bi_2Se_3. In the case of the devices studied in this thesis, we adopt a different approach, by considering the upper and lower limits of the resistance of both HgTe and Py.

One way to circumvent the resistivity difference in such devices is to couple topological insulators to insulating ferromagnets instead of ferromagnetic metals, so that the majority of the current flows through the topological insulator layer. A few investigations in this direction can be found in the literature on topological insulator/magnetic topological insulator bilayers, where the spin conversion efficiencies seem to be higher than in nonmagnetic metals [15, 16]. Coupling HgTe with ferromagnetic insulators is not an option in our devices, HgTe is volatile at about 80 degrees Celsius and the growth of magnetic insulators generally involves temperatures of a few hundred degrees Celsius [17].

After understanding the factors that can influence the RF current flowing through the HgTe/Py bilayer, it is clear at this point that the amplitudes of the spin-torques and efficiencies can only be estimated and that such efficiencies should be always analyzed with great care. Assuming that band bending at the interface of the two materials is negligible, one can determine the currents by taking into account the attenuation of the RF cables and the resistivity of HgTe and Py. The data used for this analysis is the same as the ones presented in Sec. 3.6.2.

The losses in the coaxial cables and in the sample box were determined from Fig. 3.16, which shows the frequency dependence of the attenuation in units of *dB*. At a given frequency f, the output voltage from the power supply will be attenuated by a factor in *dB*. For a temperature of $T = 4.2$ Kelvin, the initial voltage, i.e., the voltage at the output of the power supply has a nominal value of $V = 600$ mV. At a frequency $f = 4$ GHz, the RF cables attenuate the initial voltage by approximately -6 dB, so that the voltage arriving at the signal line of the coplanar waveguide is $V_{in} \approx 300$ mV, named V_{in} for "input voltage".

Having the voltage drop at the device, one can estimate the current flowing through the Py and through the HgTe layers. As already mentioned, estimating the conductivity/resistivity of the

HgTe layer is a hard task and the following simplifications were made in order to estimate the order of magnitude of the torques in our devices.

The longitudinal resistance value of the HgTe layer is obtained by measuring the Hall bar built separately in the SOT devices. For simplification, this measurement was already performed in the spin-pumping experiments in [9] and it was shown that the lithography process alters the resistance of the sample. Indeed, for a Hall bar processed with the standard optical lithography technique, the sheet resistance at $V_g = 0$ V was found to be $R_s \approx 50\ \Omega/\square$. However, with the lithography process used to produce the bilayer devices, the sheet resistance increases to $R_s \approx 500\ \Omega/\square$. These two values will be used as "lower" and "upper" limits to estimate the resistance of HgTe in the SOT devices. Here, the resistance of a square conductive sheet, $\square$, is the same no matter its size, as long as it remains a square. The reader is made, again, aware that the *precise* resistance value of the HgTe cannot be obtained by other means. Adopting these values for the ST7 A device dimensions, the resistance of HgTe, assuming no band bending or diffusion of permalloy into it, is $R_{HgTe} \approx$ (100-1000) Ω for lower and upper limits, respectively.

Following the same procedure, one finds that the resistance of Permalloy for the ST7 A device dimensions is $R_{Py} \approx 12\ \Omega$. It is clear from these values that most of the current will be shunted through the Py layer, leaving a significant uncertainty on how much current flows through the HgTe layer, whose resistance is approximately 10 to 100 times higher than Py. Knowing the current flowing through the HgTe layer, one can use Eqs. (3.21) and (3.22) to calculate the in-plane and out-of-plane torques, respectively. Here, $\alpha = 1 \times 10^{-2}$ was used [9, 11, 12]. The symmetric and antisymmetric amplitudes of the torques were obtained by fitting the mixing voltage curve with the symmetric and antisymmetric Lorentzian lineshape. For the estimation of the torques at room temperature, the data presented in Sec. 3.6.1 was used and a similar procedure, as described above, was performed. The calculated torque amplitudes for lower and upper limits at $T = 4.2$ K are presented in tables 3.1 and 3.2, respectively. For the calculation of the torques at room-temperature, we assume the lower limit resistance of HgTe at low-temperatures, $R_{HgTe} \approx 50\ \Omega$, for the (20x20) μm^2 device dimensions. The torques obtained at room-temperature are presented in table 3.3.

The amplitudes of the torques obtained in this work at $T = 300$ K are similar to the ones presented in Ref. [7] for similar investigations on spin-orbit torques generated by the BiSe topological insulator. At $T = 4.2$ K, the torque amplitudes differ from those values up to one (two) orders of magnitude for the upper (lower) limits, respectively. This discrepancy in these values comes from the definition of the "current-to-spin" efficiency. For the lower limit of the HgTe resistance, there will be more current flowing through it, resulting in higher efficiency values.

f (GHz)	I_{RF} (mA)	S (μV)	A (μV)	$\tau_{\parallel}$ (T)	$\tau_{\perp}$ (T)
3.2	3.4	1.5	7.1	2.8×10^{-5}	0.9×10^{-5}
4.0	3.0	1.6	7.6	3.4×10^{-5}	1.7×10^{-5}
5.0	2.8	1.8	5.5	4.2×10^{-5}	1.8×10^{-5}
6.0	2.5	1.8	4.2	4.8×10^{-5}	2.0×10^{-5}
7.0	2.4	1.0	2.2	2.8×10^{-5}	1.3×10^{-5}

Table 3.1: Parameters used in the calculation of the torques at different frequencies at $T = 4.2$ K and $\phi = 45$ degrees for the lower limit

f (GHz)	I_{RF} (mA)	S (μV)	A (μV)	$\tau_{\parallel}$ (T)	$\tau_{\perp}$ (T)
3.2	340	1.5	7.1	2.8×10^{-4}	0.9×10^{-4}
4.0	300	1.6	7.6	3.4×10^{-4}	1.7×10^{-4}
5.0	280	1.8	5.5	4.2×10^{-4}	1.8×10^{-4}
6.0	250	1.8	4.2	4.8×10^{-4}	2.0×10^{-4}
7.0	240	1.0	2.2	2.8×10^{-4}	1.3×10^{-4}

Table 3.2: Parameters used in the calculation of the torques at different frequencies at $T = 4.2$ K and $\phi = 45$ degrees for the upper limit

f (GHz)	I_{RF} (mA)	S (μV)	A (μV)	$\tau_{\parallel}$ (T)	$\tau_{\perp}$ (T)
3.2	3.0	40.0	-57.0	2.4×10^{-4}	-6.7×10^{-5}
4.0	2.7	24.8	-27.8	1.7×10^{-4}	-4.6×10^{-5}
5.0	2.2	23.5	-25.0	2.0×10^{-4}	-6.4×10^{-5}
6.0	2.2	11.4	-11.2	1.1×10^{-4}	-3.5×10^{-5}
7.0	1.7	6.7	-6.6	8.8×10^{-5}	-3.3×10^{-5}

Table 3.3: Parameters used in the calculation of the torques at different frequencies at $T = 300$ K (room temperature) and $\phi = -45$ degrees

From the torque amplitudes presented in the above tables, one finds the conductivities (Eq. (3.27)) for the in-plane and out-of-plane torques at low-temperatures: $\sigma_{\parallel} \approx (1 - 50) \times 10^5 \frac{2e}{\hbar} (\Omega\text{m})^{-1}$
$\sigma_{\perp} \approx (1 - 20) \times 10^5 \frac{2e}{\hbar} (\Omega\text{m})^{-1}$

At room-temperature, the conductivity values are found to be:

$\sigma_{\parallel} \approx (5 - 15) \times 10^5 \frac{2e}{\hbar} (\Omega\text{m})^{-1}$
$\sigma_{\perp} \approx (2 - 4) \times 10^5 \frac{2e}{\hbar} (\Omega\text{m})^{-1}$

These values are of the same order of magnitude as the ones presented at Ref. [7]. One can still calculate the torque efficiencies from Eq. (3.28), which gives qualitative information on how much of the electrical current is "converted' into spin. The following values are found for $T = 4.2$ K:

$\theta_{\parallel} \approx 1 - 20$
$\theta_{\perp} \approx 1 - 10$

At room-temperature, the following torque efficiencies are calculated: $\theta_{\parallel} \approx 2$
$\theta_{\perp} \approx 0.5$

At low-temperatures, the spin-torque efficiency can reach values up to 20, which is about 10 times larger than that at 300 K. This value is comparable to the efficiencies reported in the literature for BiSe and BiSbTe systems using SOT-FMR measurement technique. Figure 3.17 is adapted from Ref. [10] and shows the spin-torque efficiencies for different material systems. In most of the Bi-based topological insulator systems, the spin-torque efficiencies increase with decreasing temperature. In BiSe films grown by MBE, this behavior was attributed to the decrease of the bulk contribution in the TI film, suggesting that the bulk states in Bi_2Se_3 "contaminate" the contribution of the TSS to the spin-torque effects [14, 18]. In other SOT-FMR experiments using the BiSe system, the spin-torque ratio was measured as a function of the thickness of the TI thin films. In these systems, the decrease of the film thickness leads to lower bulk conductance and electric transport dominated by the TSS. In Ref. [19], the authors show that in Bi_2Se_3 TI thin films (5-8 quintuple layers) the spin-torque signal is dominated by the TSS and that bulk contributions to the electric transport can weaken the spin-torque efficiencies.

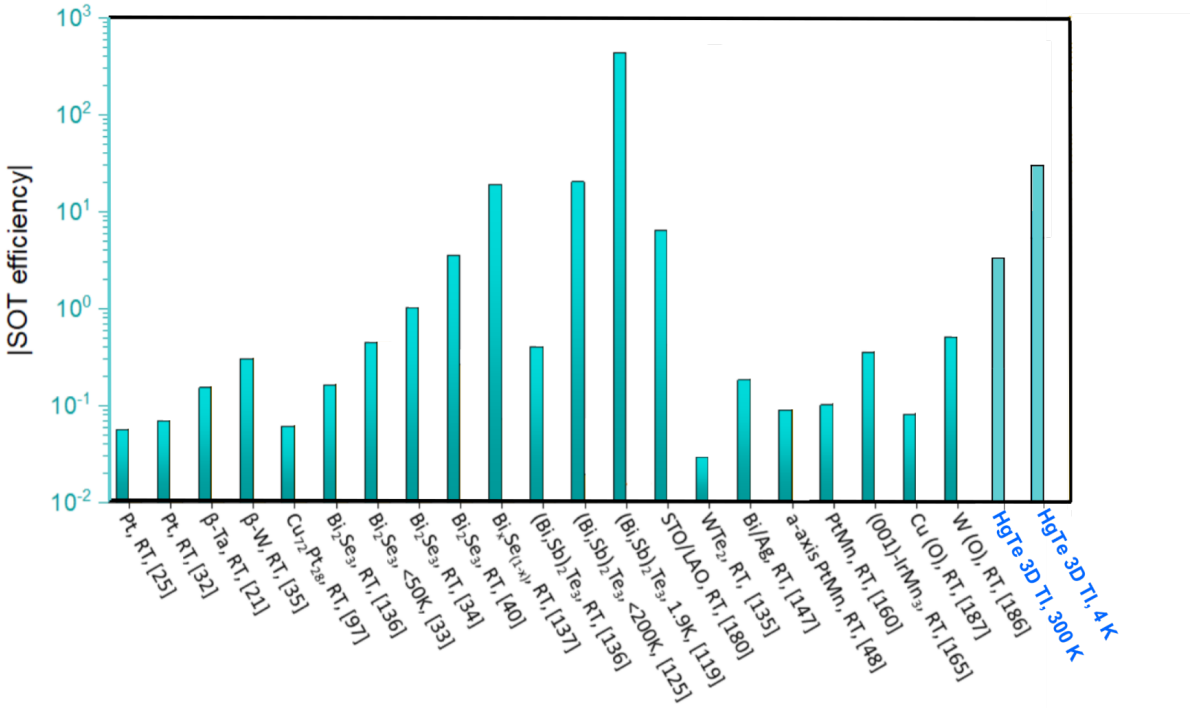

Figure 3.17: Figure adapted from [10] showing the summary of the SOT efficiencies of a variety of materials, including the present investigation on 3D TI HgTe. The x-axis denotes the materials with their corresponding measurement temperature and references as given in [10]. Here RT denotes room temperature.

In the experiments performed in this thesis, one would be tempted to state that that the SOT efficiencies generated by the 3D TI HgTe are higher at low-temperatures because the conduction is dominated by the topological surface states. However, there are several parasitic effects that

can play a role in the accurate determination of the SOT efficiencies. The next section will discuss some of the caveats in the origin of the previously discussed quantities.

3.8. Critical review of the SOT efficiencies

As briefly mentioned in Sec. 3.6.3, the angular dependence of the mixing voltages significantly differ at low- and room-temperatures. Figures 3.14 and 3.15 show that, at $T = 4.2$ K, the angular dependence of the in-plane torque component does not follow the predicted angular dependence ($\propto \cos^2(\phi)\sin(\phi)$). On the other hand, estimations of the spin-torque amplitudes indicate values comparable to similar investigations in the literature [7] (see table 3.1 and table 3.2).

(i) 3D TI HgTe at low- and room-temperatures

From the physics point of view, there are fundamental differences when it comes to the behavior of strained 3D TI HgTe at low- and room-temperature[1]. It is known that the bandgap of semiconductor materials decreases with increasing temperatures [20]. In the samples studied in this thesis, the bandgap opened via strain between the $\Gamma_{8,LH}$ and $\Gamma_{8,LH}$ bands is about 10−20 meV. At room temperature, the energy of the carriers is E ≈ 25 meV and it is reasonable to consider that the electrical transport is no longer dominated by the topological surface states, but rather by bulk states. Several theoretical works in the literature suggest that the bulk states might enhance the damping-like torque [21, 22], which could be a candidate to explain the presence of both in-plane and out-of-plane torques at room temperature. At low temperatures, where only topological surface states contribute to the conduction, the angular dependence of the in-plane component of the torque does not follow a clear symmetry, indicating that in-plane torque components might not be present in our devices. As already discussed in Sec. 3.2 and in Ref. [5], the in-plane component of the torque is proportional to the out-of-plane component of the magnetization ($\tau_{\parallel} \propto m_z$). For the devices investigated in this thesis, the out-of-plane component of the magnetization of permalloy disappears, since the films are thin (≈ 25 nm) and the magnetization predominantly lies on the x, y-plane.

(ii) HfO tunnel barrier

Another factor that might be crucial to undoubtedly identify the origin of the torques in the TI/FM devices is the quality of the diffusion barrier separating HgTe from Permalloy. Since the spin-orbit torque originating from the iSGE relies on the overlap between the wavefunctions of the carriers in the TSS and in the ferromagnet, the properties of the barrier play an essential role in interpreting the results described above. The main feature of a tunnel barrier is that it should be simultaneously thin (around 1 nm to 2 nm) to study the SOTs and thick enough to guarantee that electrons flowing through the TSS do not flow through the ferromagnet.

For the situation where the insulator thickness is too thin, “defects” or conductive shorts through

[1] It is worth to mention here that, so far, it is not clear if the strain in the HgTe remains constant at low- and room-temperatures

the insulating barrier, known as pinholes can cause the shunting of the HgTe and the permalloy thin film. Moreover, if the barrier is too thin, Py could diffuse into HgTe yielding degradation of the topological surface states, modification of the interface chemistry [23] or their different work functions could lead to the Fermi level position variation [24, 25]. Several similar works reported in the literature do not avoid this interdiffusion and deposit the ferromagnetic material directly onto the topological insulator. Scarce reports are found on the literature addressing this issue, being one of them the work in [26] that employed an 8 nm-thick copper spacer layer in between BiSeTe TI and 10 nm of Permalloy in order to study the Fermi-level-dependence of the spin-orbit torques. They were able to show that the thickness of the Cu spacer can greatly influence the amplitude of both in-plane and out-of-plane torques.

For the case in which the HfO tunnel barrier is too thick, the reader is reminded that the surface state spins couple with the magnetic moments of the ferromagnet through an exchange term H_{ex} =-$\Delta_{ex}\vec{m}\cdot\vec{S}$. If such overlap is not guaranteed, it is likely that the in-plane torque will be absent and the out-of-plane torque component originating from the Oersted field dominates the SOT amplitude. The estimated efficiencies arising from the Oersted fields in the devices studied in this thesis can be computed from Eq. (3.27) and are found to be $\theta_{Oe,RT} = 1.5$ and $\theta_{Oe,LT} = 5.0$ for room- (RT) and low-temperatures (LT), respectively. These efficiency values clearly state that Oersted fields could play a role in the out-of-plane torque efficiencies, especially at room temperatures, where the in-plane torque efficiencies are estimated to be $\theta_{\perp} \approx 0.5$. However, given the uncertainty in the determination of the electric currents flowing through the HgTe layer, one is not able to disentangle between the torques arising from the Oersted field and the SOTs by the spin-polarization in the topological surface states.

It is worth mentioning that spin-pumping FMR experiments performed at room temperature in 3D HgTe TIs showed that a $\approx$ 1.6 nm-thick HgCdTe can be a suitable barrier to protect the surface states of HgTe and it can lead to very high spin-to-charge current conversion rates [27]. In the same work, the authors also demonstrate that the insertion of a Cu spacer layer instead of HgCdTe leads to small conversion efficiencies, even in comparison to NiFe in direct contact with HgTe. Their results suggest that the metal/insulator in contact with the topological insulator is a crucial parameter in experiments involving spin-torques or spin-pumping.

(iii) Thermoelectric effects

One main difference between the measurements described in Sec. 3.6.3 is that the excitation voltage used in the measurements at low temperature is twice as high in comparison with the measurements at room temperature. The use of high power/voltages combined with a ferromagnetic metal with low resistance can lead to the heating of the permalloy and, consequently, to thermovoltages at the interface of the bilayer, contaminating the reading of the mixing voltage.

Because of the different conductivities of HgTe and permalloy, it is likely that most of the electrical current will be shunted through the permalloy layer. If the RF currents applied to the TI/FM bilayer are too high, this could lead to the heating of the ferromagnetic film while the TI layer remains "cold", i.e., at $T = 4.2$ K. As a potential difference between two points in a metal generates an electrical current, a temperature difference also generates electron transport. When a thermal gradient is present in a ferromagnetic metal or semiconductor, an electric field perpendicular to both the temperature gradient and the magnetization is generated [28]. The thermopower response will depend on the material constituting the junction and on its density of states (DoS).

In the case of the HgTe/Py bilayer, this thermal parasitic effect should be considered and unequivocally identified in the analysis of the experiment, as it can give rise to a significative contribution for the V_{mix} response of the ferromagnet. Previous studies of the effects of temperature gradients in ferromagnetic semiconductor junctions were previously studied in our group. Naydenova et. al showed a voltage response to a temperature difference across the interface between (Ga, Mn)As/GaAs junctions [29].

If thermoelectric effects are present in the HgTe/Py bilayer, the mixing voltage signal measured in our experiments could be poisoned by the thermovoltage, in a way that both symmetric and antisymmetric components can no longer be reliably determined. The current densities calculated for the studies at low temperatures are $j \approx 10^6 \mathrm{A/cm}^2$. These current density values are one order of magnitude lower in comparison with values reported on investigations of magnetization switching of bilayers consisting of heavy metals (Ta) and magnetic tunnel junctions [30]. On the other hand, the current density values found here are similar to the ones reported on the investigation of the magnetization switching of BiSe/Py bilayers measured via magneto-optic Kerr effect (MOKE) [19]. Given the intrinsic inaccuracy on the determination of the current flowing through the HgTe/Py bilayer, one cannot reliably assess if thermoelectric effects might poison the reliable reading of the magnetization state/oscillations.

A similar experiment as the one reported by Naydenova et. al. was performed on HgTe/ZrO/Py layered structures by *K. Martin* [31]. In this type of structure, in order to measure the thermovoltages at the $2f$ frequency, electrons should flow only through the HgTe heating channel. However, due to non-uniform barrier thickness, the electrons can also flow through different current paths and, therefore, the $2f$ voltage detection is contaminated by the $1f$ contribution and the reliable reading of the thermovoltages in these systems becomes challenging.

For the investigations performed in this thesis, the SOT device geometry does not allow for a study of the thermoelectric effects and/or the quality of the tunnel barrier in the SOT devices. However, the goal of this discussion is to make the reader aware that any SOT efficiencies and angular dependences should be analyzed with extreme care, since these parasitic effects may originate a significant uncertainty on identifying if SOTs are present in our devices and in

determining their origin and amplitudes. The interested reader is referred to Ref. [31] for further investigations about thermoelectric effects.

(iv) In-plane MR of the 3D TI HgTe

Last, all the measurements performed in the SOT devices assume that an in-plane magnetic field does *not* affect the magnetoresistance of the 3D TI HgTe. However, Chap. 4 will demonstrate that this is not the case and that, indeed, in-plane magnetic fields modify the MR of the topological insulator. The extent of this influence in the SOT-FMR measurements is out of the scope of this thesis. However, some early "hints" on the influence of the in-plane magnetic field in spin-pumping FMR experiments are discussed by C. Jünger and the reader is referred to his work for further information [9]. As the reader can already conclude, there are a few experimental parameters that play a key role in interpreting the results on the devices investigated in this thesis.

As already discussed in Sec. 3.3.2, the RF current flowing through the device is a crucial parameter in estimating the torques accurately. Moreover, before calculating the torque efficiencies, one should be aware that several parasitic effects can contribute to correctly estimate these amplitudes and that such efficiencies should be taken *cum grano salis*.

Ultimately, the studies performed in this thesis aimed to show that a proper and careful determination of the spin torque amplitudes can be cumbersome, given that several effects make it uncertain not only to quantify the SOT efficiencies but also raises the question if HgTe is efficient in generating spin torques at all. Additionally, the nature of the FMR experiments, combined with an indirect, model-dependent extraction of parameters, requires a careful understanding of the mentioned possible parasitic effects and their quantitative influence on the torque efficiencies.

It is clear from the investigations reported here that, in order to reliably estimate the spin torque efficiencies, one needs a tool that reliably writes the information in the magnetization and undoubtfully and correctly reads its magnetic state. An elegant novel experimental approach is presented in the next section.

3.9. Perpectives

As already discussed in the previous section, there are several parasitic effects that can influence the estimation of the current-induced spin-orbit torques using the FMR technique, especially the estimation of the current flowing through the TI/FM bilayer. In order to circumvent these challenges, one requires a device and experimental setup where the current flowing through the bilayer is known or where the current flows only through the HgTe layer. In the framework of the spin Hall effect, the works performed in [32] and [30] were able to demonstrate a spin Hall effect-induced magnetization switching of an in-plane magnetized nanomagnet at room temperature. By using a bilayer system consisting of a thin film of Tantalum and a magnetic tunnel junction (MTJ) with different thickness and magnetization scheme configurations, both works were able to demonstrate that the magnetization switches for critical currents in the order of 10^7 A $(\mathrm{cm})^{-2}$. These works were able to show that the spin current can cause not only magnetization oscillations but also switch the magnetization of ferromagnets.

Compared to the SOT-FMR technique, the direct measurement of the magnetization switching of a nanomagnet offers several advantages, such as the possibility to estimate the electrical current flowing through the topological insulator layer and the direct measurement of the amount of charge current needed to switch the magnetization of the ferromagnet. Another advantage is this approach, is that thermopower effects could be avoided since one could send an electric current pulse and wait for the system to cool down before reading the magnetization state. In this way, the magnetization state can be reliably read, without contamination from spurious voltages. However, a problem that could arise in such a measurement scheme lies in the spin texture of the top topological surface state since, as discussed previously, an Oersted field can also switch the magnetization of the ferromagnet. Moreover, if the Oersted field and the spins of the carriers in the topological surface states are aligned in the same direction, the measurement of the spin-orbit torque is compromised, since it is not possible to distinguish if the switching occurred due to the spin accumulation in the surface states or due to the Oersted field. Reversing the direction of the electrical current also does not provide insight in distinguishing both contributions, since both the spin density and the Oersted field invert their signs with inverting the current direction. An accurate determination of the SOTs generated from the iSGE on the topological surfaces can be obtained if the Oersted field and the direction of the spin density are oriented in opposite directions.

From this perspective, the experimental scheme depicted in Fig. 3.18 presents an alternative to circumvent the parasitic effects rising from the SOT-FMR technique. In this scheme, a spin valve device consisting of Py/Cu/CoFe is sputtered on top of the 3D HgTe TI, separated by a thin insulating barrier. Spin valves are devices consisting of two ferromagnets (here Py and CoFe) with in-plane magnetization separated by a thin conducting layer (Cu). Such devices exhibit

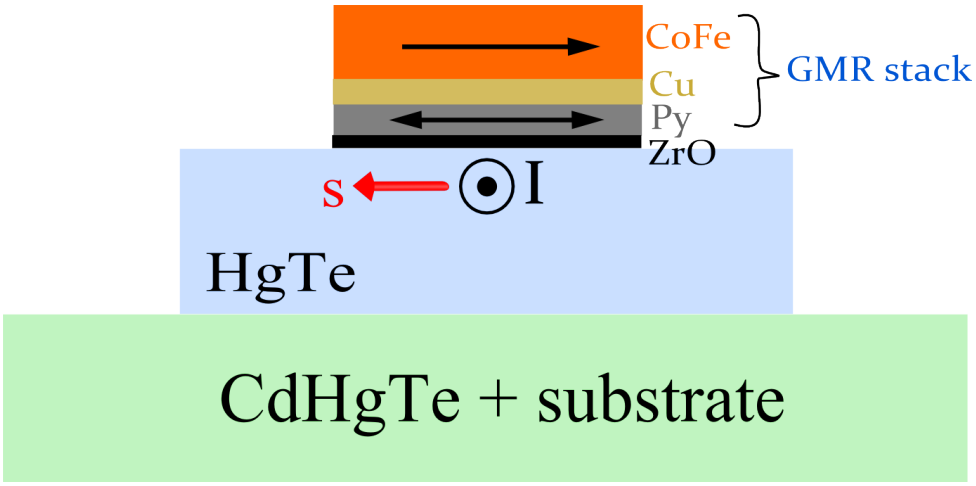

Figure 3.18: Micrograph image of the produced HgTe/Py bilayer. Here, S and G stands for the signal and ground lines, respectively. Permalloy (FM) is accurately placed into the coplanar waveguide by means of optical lithography.

giant magnetoresistance (GMR), a spin-dependent scattering effect where the resistance of both magnetizations aligned parallel to each other is lower in comparison with the situation where the magnetization of the ferromagnetic layers are perpendicular to each other, as depicted in Fig. 3.18 (see the introduction section for further details). In the proposed experimental setup, a current would flow through the HgTe TI layer and, due to spin-momentum locking, there will be a spin accumulation at the interface whose angular momentum can be transferred to the Py adjacent ferromagnetic layer. By keeping the magnetization of CoFe pinned in a specific orientation, the transfer of angular momentum would yield the magnetization to switch from, for example, parallel to anti-parallel state. This is called the "writing" step. The "reading" step can be performed by electrically measuring the GMR of the spin valve by means of a metallic air bridge contact [33], which allows the measurement of the resistance of the spin-valve. In this way, the current-induced transfer torques in the TI/spin-valve bilayers could be measured directly via the switching of the magnetization, without the need for indirect and model-dependent extraction of torque amplitudes. For studies of SOTs in these type of devices, the reader is referred to K. Martin Ph.D. thesis [31].

3.10. Summary and conclusions

In this chapter, we introduced the physics of the generation of spin-polarized currents in topological insulators and how they can be used to manipulate the magnetization of an adjacent ferromagnet. A thorough mathematical description of how the Landau–Lifshitz–Gilbert–Slonczewski is applied to the TI/FM system was introduced, as well as how experimental quantities can be obtained. The device fabrication section showed that its design should be carefully planned in order to avoid parasitic effects that can influence the measurements of the spin-torque. The measurement setup showed that the mixing of the RF current and the RF resistance will give rise to a DC voltage, from which we can make an indirect quantitative measurement of the spin torque efficiencies.

In the results section, the reader was made aware that, although the investigations in this thesis show that HgTe might be efficient in exerting spin torques in adjacent ferromagnets, several parasitic effects might contaminate the writing and the reading of the information in the ferromagnet, leading many times to overestimated spin efficiencies and/or ambiguous interpretation on the origin of the spin-orbit torques. One important parameter allowing for a better estimation of the torque amplitudes relies on knowing the current flowing through the HgTe layer, which in turn depends on its conductivity. Determining such a parameter is extremely difficult since band bending effects could play a role in the conductivity of the 3D TI HgTe layer. While other reports mimick the bend banding in their material systems [7], in this investigation we did not attempt to compute the conductivity of the active layer, but rather to establish a "lower" and an "upper" boundary for its value based on how the sample fabrication process influences the resistivity of the material.

When comparing the SOT efficiencies using 3D TI HgTe with other existent topological insulators, the investigations in this thesis show that they are comparable [10], which would put HgTe as a potential material for spintronics applications. However, the reader is in numerous opportunities incentivized to maintain a critical attitude towards claims of high SOT efficiencies generated by 3D topological insulators, in the hope to provide the reader with a stimulus to find possible solutions for the discussed issues.

Moreover, an elegant approach was introduced in the perspectives section, where HgTe is combined with a spin-valve nanostructure. This experiment will allow not to only know the current density in the HgTe layer, but also to *switch* the magnetization of the ferromagnet, in stark contrast with the investigations in this thesis, where the SOT could only cause resistance oscillations in the Permalloy that could be measured only *indirectly* via the AMR effect.

References

[1] Y. A. Bychkov and E. I. Rashba, "Properties of a 2D electron gas with lifted spectral degeneracy," *JETP Letters*, vol. 39, no. 2, pp. 66–69, 1984.

[2] V. M. Edelstein, "Spin polarization of conduction electrons induced by electric current in two-dimensional asymmetric electron systems," *Solid State Communications*, vol. 73, no. 3, pp. 233–235, 1990.

[3] S. D. Ganichev, S. N. Danilov, P. Schneider, V. V. Bel'Kov, L. E. Golub, W. Wegscheider, D. Weiss, and W. Prettl, "Electric current-induced spin orientation in quantum well structures," *Journal of Magnetism and Magnetic Materials*, vol. 300, pp. 127–131, 2006.

[4] I. Garate and M. Franz, "Inverse spin-galvanic effect in the interface between a topological insulator and a ferromagnet," *Physical Review Letters*, vol. 104, no. 146802, pp. 1–4, 2010.

[5] P. B. Ndiaye, C. A. Akosa, M. H. Fischer, A. Vaezi, E. A. Kim, and A. Manchon, "Dirac spin-orbit torques and charge pumping at the surface of topological insulators," *Physical Review B*, vol. 96, no. 014408, pp. 1–8, 2017.

[6] A. Manchon, J. Železný, I. M. Miron, T. Jungwirth, J. Sinova, A. Thiaville, K. Garello, and P. Gambardella, "Current-induced spin-orbit torques in ferromagnetic and antiferromagnetic systems," *Reviews of Modern Physics*, vol. 91, no. 035004, 2019.

[7] A. R. Mellnik, J. S. Lee, A. Richardella, J. L. Grab, P. J. Mintun, M. H. Fischer, A. Vaezi, A. Manchon, E. A. Kim, N. Samarth, and D. C. Ralph, "Spin-transfer torque generated by a topological insulator," *Nature*, vol. 511, pp. 449–451, 2014.

[8] C. Kittel, "On the theory of ferromagnetic resonance absorption," *Physical Review*, vol. 73, no. 2, pp. 155–161, 1948.

[9] C. Jünger, *Spin Pumping in the Topological Insulator HgTe*. Master thesis, Julius-Maximilians-Universität Würzburg, 2015.

[10] Y. Wang, R. Ramaswamy, and H. Yang, "FMR-related phenomena in spintronic devices," *Journal of Physics D: Applied Physics*, vol. 51, jun 2018.

[11] J. Donges, *Spin-transfer torque generiert durch einen 3-dimensionalen topologischen Isolator*. Bachelor thesis, Julius-Maximilians-Universität Würzburg, 2015.

[12] N. Krainovic, *Ferromagnetische Resonanz und Spin-transfer Torque mit 3-dimensionalen topologischen Isolatoren*. Bachelor thesis, Julius-Maximilians-Universität Würzburg, 2015.

[13] M. V. Costache, M. Sladkov, C. H. Van Der Wal, and B. J. Van Wees, "On-chip detection of ferromagnetic resonance of a single submicron Permalloy strip," *Applied Physics Letters*, vol. 89, no. 192506, pp. 1–4, 2006.

[14] Y. Wang, P. Deorani, K. Banerjee, N. Koirala, M. Brahlek, S. Oh, and H. Yang, "Topological surface states originated spin-orbit torques in Bi_2Se_3," *Physical Review Letters*, vol. 114, no. 257202, pp. 1–5, 2015.

[15] Y. Fan, P. Upadhyaya, X. Kou, M. Lang, S. Takei, Z. Wang, J. Tang, L. He, L. T. Chang, M. Montazeri, G. Yu, W. Jiang, T. Nie, R. N. Schwartz, Y. Tserkovnyak, and K. L. Wang, "Magnetization switching through giant spin-orbit torque in a magnetically doped topological insulator heterostructure," *Nature Materials*, vol. 13, pp. 699–704, 2014.

[16] Y. Fan, X. Kou, P. Upadhyaya, Q. Shao, L. Pan, M. Lang, X. Che, J. Tang, M. Montazeri, K. Murata, L. T. Chang, M. Akyol, G. Yu, T. Nie, K. L. Wong, J. Liu, Y. Wang, Y. Tserkovnyak, and K. L. Wang, "Electric-field control of spin-orbit torque in a magnetically doped topological insulator," *Nature Nanotechnology*, vol. 11, pp. 352–359, 2016.

[17] M. B. Jungfleisch, J. Ding, W. Zhang, W. Jiang, J. E. Pearson, V. Novosad, and A. Hoffmann, "Insulating nanomagnets driven by spin torque," *Nano Letters*, vol. 17, pp. 8–14, 2017.

[18] J. Han, A. Richardella, S. A. Siddiqui, J. Finley, N. Samarth, and L. Liu, "Room-temperature Spin-Orbit Torque Switching Induced by a Topological Insulator," *Physical Review Letters*, vol. 119, no. 077702, pp. 1–5, 2017.

[19] Y. Wang, D. Zhu, Y. Wu, Y. Yang, J. Yu, R. Ramaswamy, R. Mishra, S. Shi, M. Elyasi, K. L. Teo, Y. Wu, and H. Yang, "Room temperature magnetization switching in topological insulator-ferromagnet heterostructures by spin-orbit torques," *Nature Communications*, vol. 8, no. 1364, 2017.

[20] T. Ihn, *Semiconductor Nanostructures: Quantum states and electronic transport*. Oxford: Oxford, 2010.

[21] F. Mahfouzi, B. K. Nikolić, and N. Kioussis, "Antidamping spin-orbit torque driven by spin-flip reflection mechanism on the surface of a topological insulator: A time-dependent nonequilibrium Green function approach," *Physical Review B*, vol. 93, no. 115419, pp. 1–10, 2016.

[22] M. H. Fischer, A. Vaezi, A. Manchon, and E. A. Kim, "Spin-torque generation in topological insulator based heterostructures," *Physical Review B*, vol. 93, no. 125303, pp. 1–4, 2016.

[23] L. A. Walsh, C. M. Smyth, A. T. Barton, Q. Wang, Z. Che, R. Yue, J. Kim, M. J. Kim, R. M. Wallace, and C. L. Hinkle, "Interface Chemistry of Contact Metals and Ferromagnets on the Topological Insulator Bi2Se3," *Journal of Physical Chemistry C*, vol. 121, pp. 23551–23563, 2017.

[24] S. Zhang and A. Fert, "Conversion between spin and charge currents with topological insulators," *Physical Review B*, vol. 94, no. 184423, pp. 1–5, 2016.

[25] J. Zhang, J. P. Velev, X. Dang, and E. Y. Tsymbal, "Band structure and spin texture of Bi_2Se_3 3d ferromagnetic metal interface," *Physical Review B*, vol. 94, no. 014435, pp. 1–7, 2016.

[26] K. Kondou, R. Yoshimi, A. Tsukazaki, Y. Fukuma, J. Matsuno, K. S. Takahashi, M. Kawasaki, Y. Tokura, and Y. Otani, "Fermi-level-dependent charge-to-spin current conversion by Dirac surface states of topological insulators," *Nature Physics*, vol. 12, pp. 1027–1031, 2016.

[27] P. Noel, C. Thomas, Y. Fu, L. Vila, B. Haas, P. H. Jouneau, S. Gambarelli, T. Meunier, P. Ballet, and J. P. Attané, "Highly Efficient Spin-to-Charge Current Conversion in Strained

HgTe Surface States Protected by a HgCdTe Layer," *Physical Review Letters*, vol. 120, no. 167201, pp. 1–6, 2018.

[28] G. E. W. Bauer, E. Saitoh, B. J. V. Wees, and P. St, "Spin caloritronics," *Nature Materials*, vol. 11, pp. 391–399, 2012.

[29] T. Naydenova, P. Dürrenfeld, K. Tavakoli, N. Pégard, L. Ebel, K. Pappert, K. Brunner, C. Gould, and L. W. Molenkamp, "Diffusion thermopower of (Ga,Mn)As/GaAs tunnel junctions," *Physical Review Letters*, vol. 107, no. 197201, pp. 1–5, 2011.

[30] S. Fukami, T. Anekawa, C. Zhang, and H. Ohno, "A spin-orbit torque switching scheme with collinear magnetic easy axis and current configuration," *Nature Nanotechnology*, vol. 11, pp. 621–625, 2016.

[31] K. Martin, *Current-induced magnetization switching by a generated spin-orbit coupling in the 3D topological insulator material HgTe*. PhD thesis, Julius-Maximilians-Universität Würzburg, 2020.

[32] L. Liu, C. F. Pai, Y. Li, H. W. Tseng, D. C. Ralph, and R. A. Buhrman, "Spin-torque switching with the giant spin hall effect of tantalum," *Science*, vol. 336, no. 6081, pp. 555–558, 2012.

[33] T. Borzenko, C. Gould, G. Schmidt, and L. W. Molenkamp, "Metallic air-bridges fabricated by multiple acceleration voltage electron beam lithography," *Microelectronic Engineering*, vol. 75, pp. 210–215, 2004.

4

Galvanomagnetic effects in the 3D TI HgTe

In 1856, William Thomson observed an increase in the longitudinal resistance of ferromagnets for an in-plane magnetic field applied parallel to the electric current, while the resistance decreased for magnetic field applied perpendicular to the current [1, 2]. Although anisotropies in the magnetoresistance are understood to be a key signature of the magnetoresistance of ferromagnetic materials [2], in this chapter we investigate the surprising observation of this effect in the non-magnetic 3D TI HgTe. We start the chapter with the characterization of the devices used to investigate this effect. Since the measurement setup requires a careful alignment between the sample and the in-plane magnetic field rotation planes, the reader is guided through a section on how to properly perform such an alignment, followed by electronic transport measurements performed in two different devices. The reader is then introduced to band structure calculations that attempt to model and explain such effects and to a detailed discussion of the challenges in finding an unified model that explains our observations.

4.1. Sample characterization

The sample that will be investigated in detail in this chapter is named "Q2830". It consists of a 70 nm thick 3D HgTe topological insulator layer, grown on a CdTe substrate with 10 nm thick (Cd,Hg)Te top and bottom layers, as sketched in Fig. 4.1a. The samples are patterned into a Hall bar configuration sketched in Fig. 4.1b, where the distance between the longitudinal voltage contacts is $L = 600$ μm and the width of the Hall bar is $W = 200$ μm. In order to tune the carrier density of the topological insulator, the sample is equipped with a top gate electrode (in orange in Fig. 4.1b) separated by a 110 nm thick SiO_2/Si_3Ni_4 insulator (not shown in the figure).

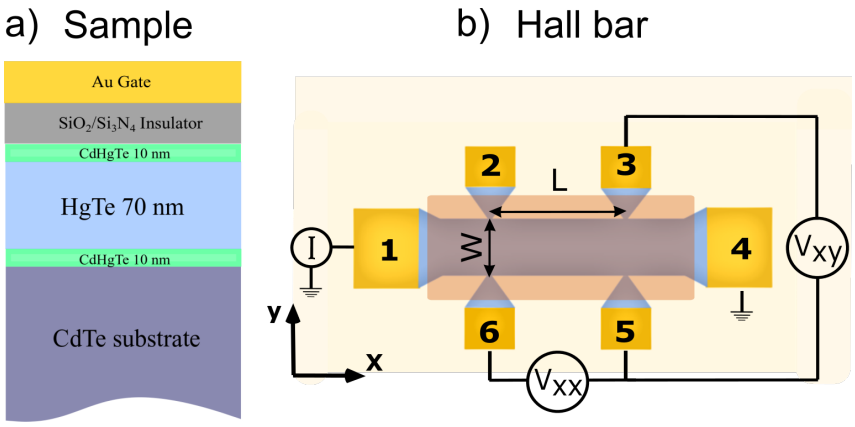

Figure 4.1: a) Layer stack of device Q2830 used in the magnetotransport studies in this chapter. The device consists of a CdTe substrate, followed by a 70 nm thick HgTe sandwiched between 10 nm thick CdHgTe protective layers. b) The devices are shaped into a Hall bar geometry in order to measure the longitudinal (V_{xx}) and transversal (V_{xy}) voltages.

In order to characterize the sample transport properties, quantum Hall effect measurements were performed at $T = 4.2$ K. Refering to the Hall bar schematics in Fig. 4.1b, an electric current I flows through contacts 1 to 4. The longitudinal (transversal) voltages V_{xx} (V_{xy}) are measured between contacts 5 and 6 (3 and 5). The longitudinal (transversal) resistances R_{xx} (R_{xy}) can be calculated as $R_{xx}(R_{xy}) = V_{xx}(V_{xy})/I$.

Figure 4.2a shows the amplitude of the longitudinal resistance R_{xx} measured as a function of the applied gate voltage V_g at zero magnetic field. From the data presented in this figure, one can observe that the longitudinal resistance of the sample can be tuned with the application of the top gate voltage. The behavior of the sample can be better understood in combination with Figs. 4.2b and 4.2c. Figure 4.2b shows how R_{xx} and R_{xy} change as a function of the out-of-plane magnetic field B_{out} for $V_g = 0$ V. While R_{xy} shows a positive slope with quantized Hall plateaus (a key signature of topological surface states already discussed in Sec. 2.3.4), R_{xx} shows typical Shubnikov de Haas (SdH) oscillations.

Figure 4.2c shows the gate dependence of the transverse resistance R_{xy} as a function of B_{out} for different gate voltages (different colors). At $V_g = 2$ V, the Hall resistance shows a positive slope, which increases when the gate voltage is decreased. At $V_g = -1$ V (where the longitudinal resistance resistance reaches a maximum value in Fig. 4.2a), the slope of the R_{xy} curves shown in Fig. 4.2c is not linear. At $V_g = -2$ V, the R_{xy} - B_{out} curve shows a positive slope for small magnetic fields ($\approx$ 250 mT) and negative slope at high magnetic fields. This behavior indicates the presence of two types of carriers (electrons and holes) contributing to the electrical transport [3].

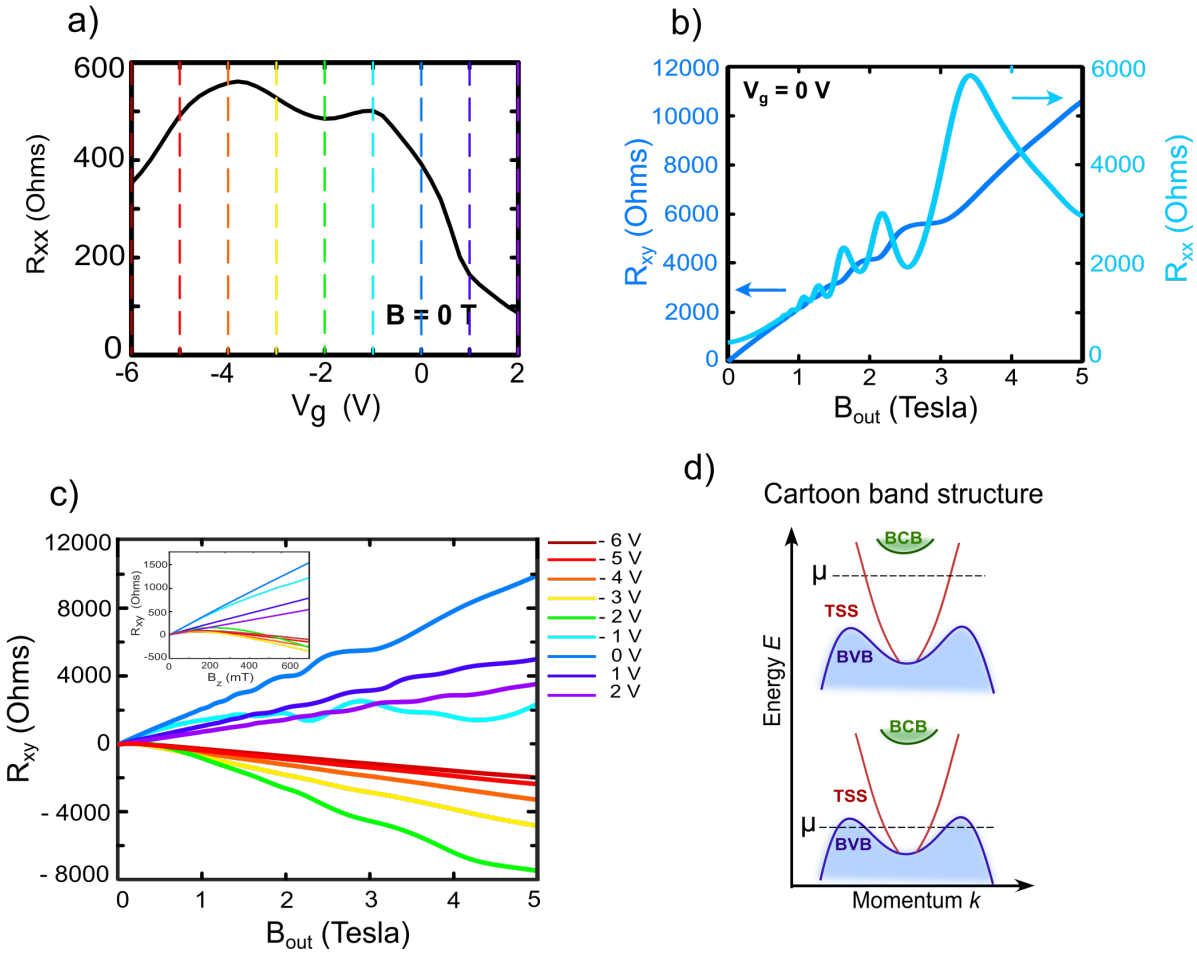

Figure 4.2: a) Gate dependence of the longitudinal resistance R_{xx} at B = 0. b) Magnetotransport measurements performed at a gate voltage $V_g = 0$ V. R_{xx} is depicted in light blue while R_{xy} is shown in dark blue. c) Gate dependence of the Hall resistance R_{xy} in the presence of an in-plane magnetic field. d) A cartoon of the HgTe band structure, depicting the topological surface states (TSS) and bulk conduction (BCB) and valence bands (BVB).

A cartoon of the HgTe band structure is shown in Fig. 4.2d. The red lines represent the topological surface states (TSS) and the green and blue bands represent the bulk conduction (BCB) and valence band (BVB) bands, respectively. The dashed black lines illustrate the chemical potential μ. As discussed in Sec. 2.3.4, this band is named camel back due to its peculiar shape.

The positive slope of R_{xy} observed in Fig. 4.2c corresponds to electrical transport dominated by the electrons from the TSS (top part of Fig. 4.2d)). On decreasing the gate voltage, the electrochemical potential crosses simultaneously the topological surface states and the camel back bands, as illustrated in the bottom part of Fig. 4.2d. When Fig. 4.2d is analyzed in combination with Fig. 4.2c, one observes that at $V_g = -1$ V R_{xy} does not show a defined slope, indicating that electrons from the TSS and holes from the camel back band contribute to the electrical transport. With the further decrease of the applied gate voltage, more hole-like states are populated and the Hall slope changes sign. For gate voltages $V_g = -2$ V to -6 V, the electrical transport is governed by the massive Volkov Pankratov states, as further discussed in Ref. [4].

The calculated carrier densities can reach values up to $n = 8 \times 10^{11}\,\mathrm{cm}^{-2}$ in the n-conducting regime and $n = -10 \times 10^{11}\,\mathrm{cm}^{-2}$ in the p-type transport regime. For the mobilities, it can reach values from $\mu_\mathrm{n} = 300 \times 10^3\,\mathrm{cm}^2/\mathrm{Vs}$ and $\mu_\mathrm{p} = 30 \times 10^3\,\mathrm{cm}^2/\mathrm{Vs}$, where μ_n and μ_p are the mobilities in the n- and p-type transport regimes, respectively.

Although this simple cartoon model crudely illustrates the main features of the HgTe band structure (and consequently its transport properties), the reader is reminded that, in real systems, only a full calculation can account for the subtleties of the band structure.

4.2. Planar Hall effect measurements

The planar Hall effect was first introduced in Sec. 2.4.1. In a few words, PHE is the angular dependence of the transversal resistance R_{xy} in the presence of an in-plane magnetic field [5, 6]. This effect is commonly observed in ferromagnetic materials, which also show anisotropic magnetic resistance (AMR) [7]. In this section, we introduce the experimental observation of PHE in the *non-magnetically* doped 3D topological insulator HgTe.

4.2.1. Setup preparation - avoiding parasitic effects

For the PHE investigations performed here, the device Q2830 described in the previous section was used. Similar to the experimental setup introduced in Sec. 3.5, the Hall bar was glued into a chip carrier and mounted into a sample holder, which is inserted into a dilution refrigerator equipped with a 3D magnet, allowing for the application of a maximum magnetic field of $B_{in} =$ 1 T in the x-, y- and z-spatial directions (B_x, B_y and B_z, respectively). The base temperature of the dilution refrigerator m is about $T = 30$ mK. A schematical of the experimental setup is shown in Fig. 4.3a. An electrical current I flows through the sample from contacts 1 to 4 and the longitudinal (transversal) voltage V_{xx} (V_{xy}) is measured between contacts 5 and 6 (3 and 5). In this configuration, an in-plane magnetic field (B_{in}) is applied in the sample plane. The angle between the in-plane magnetic field vector and the electrical current is defined as ϕ. Current and magnetic field are parallel to each other at $\phi = 0$ degrees.

PHE studies explore how the sample magnetoresistance changes in the presence of an *in-plane* magnetic field, which requires a careful alignment between the sample and the in-plane magnetic field planes. However, in realistic experimental setups, the sample plane is slightly misaligned with the magnetic field plane of rotation by an angle $\theta \approx$ 1-2 degrees. This misalignment can have several origins, such as the mounting of the sample into the dilution refrigerator or the amount of glue used to fix the Hall bar to the chip carrier. If the sample and the magnetic field planes are misaligned, an out-of-plane component of the magnetic field generates an orbital magnetoresistance that can hinder the magnetoresistance response one is interested to investigate. In order to achieve reliable measurements, one needs to perfectly align the sample plane with the magnetic field plane or, in other words, achieve $\theta \approx 0$ degrees. This is done by minimizing the transversal magnetoresistance R_{xy} for current parallel to the in-plane magnetic field because in this configuration the transversal resistance due to an in-plane magnetic field is expected to be zero (see Sec. 2.4.1). This alignment is performed at high carrier densities ($V_g = 2$ V), where the Hall slope is strictly positive. For the investigations discussed in this chapter, angles as low as $\theta \approx 0.3$ degrees were achieved.

The attention of the reader is also drawn to the fact that the angular dependence of R_{xy} rather than R_{xx} will be studied. This is because the sample misalignment cannot be fully excluded.

Although the misalignment is very small, a large sample resistance could cause the contribution from the orbital MR to be comparable to the amplitude of the AMR. Moreover, for the R_{xx} measurements, the angular dependence of the orbital MR (arising from the out-of-plane magnetic field component) has the same symmetry of the expected AMR response ($\propto \cos(\phi)^2$). In this case, one cannot distinguish between the legitimate AMR arising from an in-plane magnetic field and the orbital magnetoresistance. In the case of R_{xy}, however, a misalignment between the sample and the magnetic field plane (finite θ values) gives opposite resistance values for, say, current parallel and anti-parallel to the in-plane magnetic field. In this way, by summing up both R_{xy} for positive and negative in-plane magnetic fields, one should be able to exclude misalignment effects. This procedure will be shown in detail in Sec. 4.2.3.

Moreover, as it will be shown in Sec. 4.3.1, the longitudinal MR at strong in-plane magnetic fields shows oscillations that cannot be explained by the orbital MR arising from the sample misalignment.

Since PHE measurements are performed under an in-plane magnetic field, one needs to ensure that a non-magnetic chip carrier is used in the experiment, otherwise, its influence could "distort" the in-plane magnetic field vector, leading to erroneous interpretations on the origin of the magnetoresistance responses.

4.2.2. Planar Hall effect results

With the sample and magnetic field planes aligned parallel to each other, one can investigate the magnetoresistance response of the sample due to the application of an in-plane magnetic field (B_{in}). The experiments were performed as shown in the schematics of Fig. 4.3a. An in-plane magnetic field vector of $B_{in} = 1$ T is applied in the sample plane and rotated by an angle ϕ with respect to the electric current. Note that in this configuration it is the magnetic field vector that rotates, while the sample is static.

Figures 4.3b and 4.3c show the angular dependence of R_{xx} and R_{xy} at a gate voltage of $V_g = -3$ V, respectively. Similarly to R_{xy}, the longitudinal resistance R_{xx} shows an oscillatory behavior with a periodicity of 180 degrees. Its amplitude follows a well-behaved angular dependence $\propto \cos\phi^2$ and one would naively attribute this signature to the AMR effect introduced in Sec.2.4.1 [8]. However, as discussed in the previous section, this response is likely to be polluted by the MR response arising from an out-of-plane magnetic field component due to the sample misalignment and its extent cannot be quantified and, hence, cannot be excluded. In turn, the angular dependence of R_{xy} will be studied in detail.

Figure 4.3c shows that the transversal resistance (red dots) also shows an oscillating behavior with 180 degrees periodicity. Its amplitude is zero for current parallel or perpendicular to the in-plane magnetic field, while it shows maxima and minima when ϕ is a multiple of 45 degrees.

Mathematically, the anisotropy of R_{xy} can be fitted using Eq. (2.13) (red line in Figure 4.3c), which is slightly modified here as:

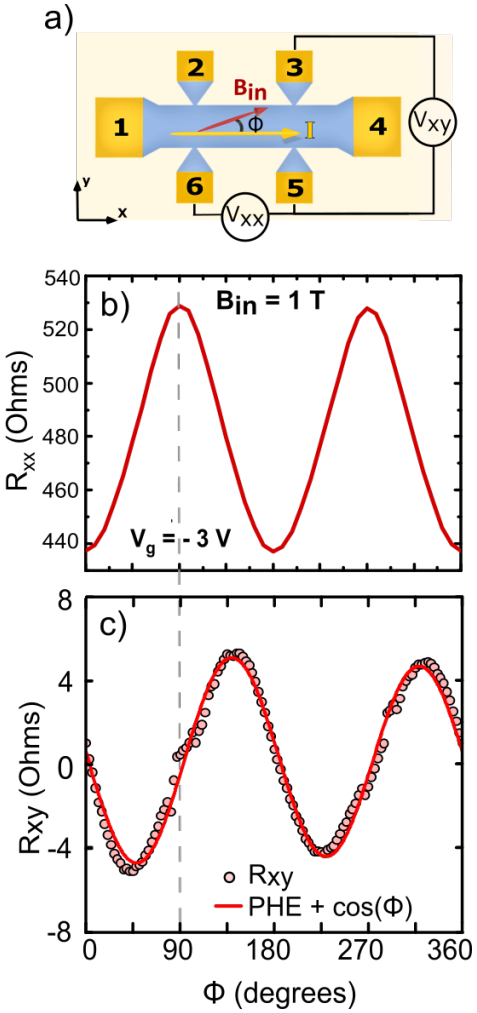

Figure 4.3: a) Schematics of the PHE and AMR measurements performed in a Hall bar shape geometry. B_{in} corresponds to the in-plane magnetic field vector which makes an angle ϕ with the electrical current. b) AMR and c) PHE effect measurements performed at V_g = -3 V at B_{in} = 1 T. In c), the red solid line is a fit $\propto \cos\phi \sin\phi$ to the PHE experimental data. In the measurements presented in b) and c), the magnetic field is parallel to the electrical current for $\phi = 0$ degrees (grey dashed lines).

$$R_{xy} = A_{PHE} \cos\phi \sin\phi + A_{mis} \cos\phi \tag{4.1}$$

The first term at the right side of Eq. (4.1) gives the angular dependence of PHE with amplitude A_{PHE}. The second term represents the symmetry of the finite misalignment between the sample and magnetic field rotation plane ($\propto \cos(\phi)$) with amplitude A_{mis}. This result clearly confirms the observation of PHE in the 3D topological insulator HgTe.

Theoretically, as briefly described in Sec. 2.4.1 and Ref. [7], the amplitudes of the AMR and PHE should be the same, however, in our experiments the AMR can be polluted by the orbital magnetoresistance. One can gain insight into the influence of the orbital MR (arising from sample misalignment) by comparing the amplitudes of the measured longitudinal and transversal resistances. In this case, we compare the *resistivity* instead of the resistance of the sample, since this quantity does not depend on the length or width of the Hall bar. The longitudinal resistivity is given by $\rho_{xx} = \mathrm{R_{xx}}W/L$, while the transversal resistivity is given by $\rho_{xy} = R_{xy}$ [9, 10]. The amplitude of the AMR (A_{AMR}) at $B_{in} = 1$ T is $A_{AMR} \approx 90\ \Omega$ (Fig. 4.3b), which leads to $\rho_{xx} \approx 30\,\Omega$. On the other hand, the amplitude of the planar Hall resistivity is $\rho_{xy} \approx 9\,\Omega$ at $V_g = -3$ V, which is at least three times smaller than its longitudinal counterpart. This result might indicate that the spurious out-of-plane magnetic field component arising from misalignment is likely to influence the amplitude of the AMR and, therefore, we focus on an assessment of the PHE in our devices.

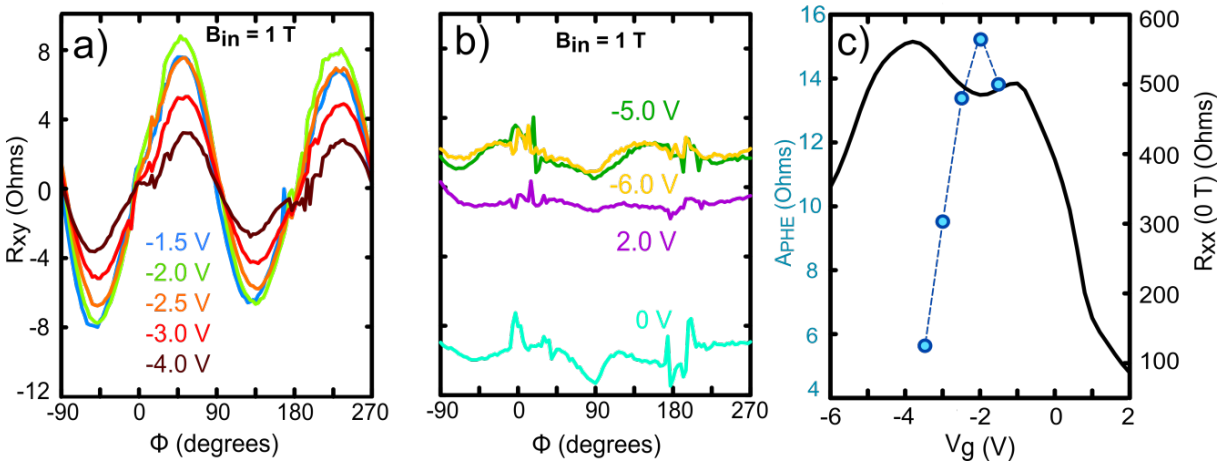

Figure 4.4: a) and b) shows the gate dependence of planar Hall effect for a magnetic field $B_{in} = 1$ T. c) PHE amplitude from the data presented in a) and b), calculated with Eq. (4.1).

Figures 4.4a and 4.4b show the PHE measured for different gate voltage values V_g. From these figures, one can observe that PHE can be resolved for gate voltages $V_g = -1.5$ V to -4.0 V. Figure 4.4b shows, however, that the effect cannot be resolved when the electric transport is dominated by electrons ($V_g = 2$ V) or holes ($V_g = -5$ V and -6 V). Figure 4.4c shows the amplitude of PHE obtained by fitting the experimental data in Figs. 4.4a and 4.4b with Eq. (4.1). The PHE amplitudes can reach amplitude values up to $A_{PHE} = 15\ \Omega$ at $B_{in} = 1$ T and the data suggests that PHE can be observed for a narrow range of carrier densities ($V_g = -1.5$ V to -3.5 V).

As already mentioned in Sec. 2.4.1, the observation of PHE is a consequence of anisotropies in the resistivity tensor. It is a key signature of the MR in ferromagnetic materials and its existence relies on the SOC, which promotes different scattering rates between s- and d-bands.

In topological systems, the planar Hall effect is also observed in Weyl and Dirac semimetals, and its original is understood as a consequence of chiral anomaly [11–14]. However, the observation of PHE in 3D topological insulators is very surprising, since these systems are non-magnetic. Moreover, this is a reproducible effect observed in several similar devices. The next section will address the amplitude of PHE at high magnetic fields (up to 7 T) and compare how the investigations presented in this thesis compare with similar observations reported in other 3D TI systems.

4.2.3. High magnetic field PHE measurements

From the previous section, one would naively conclude that PHE cannot be resolved in the n-conducting regime for in-plane magnetic fields up to $B_{in} = 1$ T. In order to acquire a better picture of the effect, this section deals with studies of PHE at high magnetic fields. The experimental setup used for the measurements described here is similar to the one described in Sec. 2.4.1, with a few modifications.

The samples are now measured at a temperature of $T = 4.2$ K and mounted into a cryostat, in a way that the magnetic field vector is constant and the sample plane is rotated. Note that in this measurement configuration, the angle θ is constant and only the angle ϕ can be modified. This means that the misalignment between the sample and the magnetic field plane cannot be avoided and/or minimized. Consequently, the MR response of the sample will be polluted by an out-of-plane magnetic field component. This parasitic MR modifies the transversal resistance R_{xy} response, since an out-of-plane magnetic component generates a Hall resistance that increases linearly with the magnetic field, as shown in Fig. 4.5a at $\phi = 135$ degrees. However, this issue can be circumvented if one takes advantage of the fact that the R_{xy} response arising from the out-of-plane magnetic field component (the Hall signal) is anti-symmetric with respect to the magnetic field or, in other words, $R_{xy}(+B) = -R_{xy}(-B)$, as shown in Fig. 4.5b. In this way, by measuring R_{xy} for positive and negative magnetic fields and by summing them up ($R_{xy}(+B) + R_{xy}(-B) = 0$), one is able to eliminate resistance responses originating from the out-of-plane magnetic field component. Hence, only the first term in Eq. (4.1), which is the amplitude of the PHE, should remain (Fig. 4.5c).

The PHE as a function of the in-plane magnetic field B_{in} at different gate voltages V_g, after the data "symmetrization", is shown in Fig. a for $\phi = 45$ degrees and in Fig. 4.6b for $\phi = 135$ degrees.

At a first glance, the most striking feature observed in Figs. 4.6a and 4.6b is that R_{xy} (or the amplitude of the PHE) does not increase monotonically with the in-plane magnetic field. For the entire range of V_g ($V_g = -5$ V to 2 V), R_{xy} shows an oscillating behavior. In order to check for consistency, one can compare the PHE amplitudes at $T = 30$ mK (see Fig. 4.4c) and $T = 4.2$ K (Figs. 4.6a and 4.6b) for an in-plane magnetic field amplitude $B_{in} = 1$ T. For example, at this

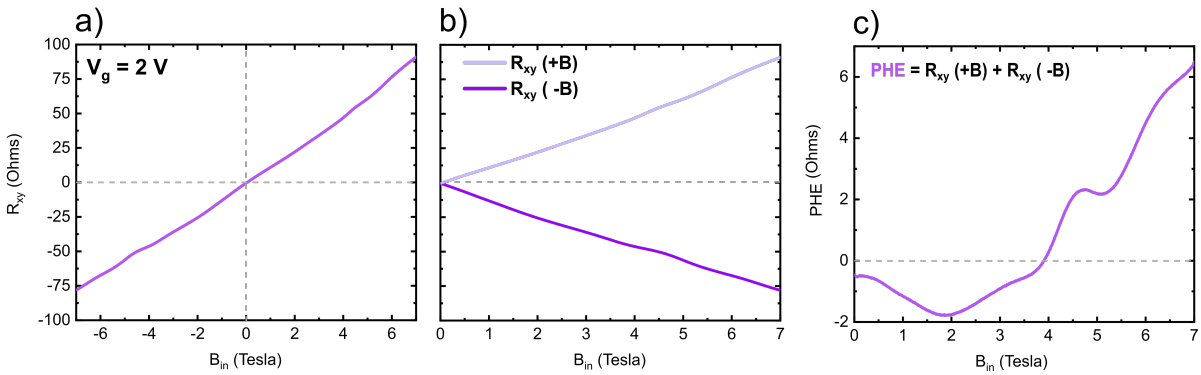

Figure 4.5: An example on how R_{xy} is obtained for $\phi = 135$ degrees and $V_g = 2$ V. a) Raw R_{xy} data: if a misalignment between the sample and the applied external magnetic field plane exists, an out-of-plane magnetic field component arise leading to a Hall response of the sample. In order to exclude this Hall resistance, a symmetrization of the data is performed as shown in b). The sum of the Hall resistance with positive and negative magnetic fields should be zero. The remaining signal is the response of the sample in the presence of a "pure" in-plane magnetic field, as depicted in c).

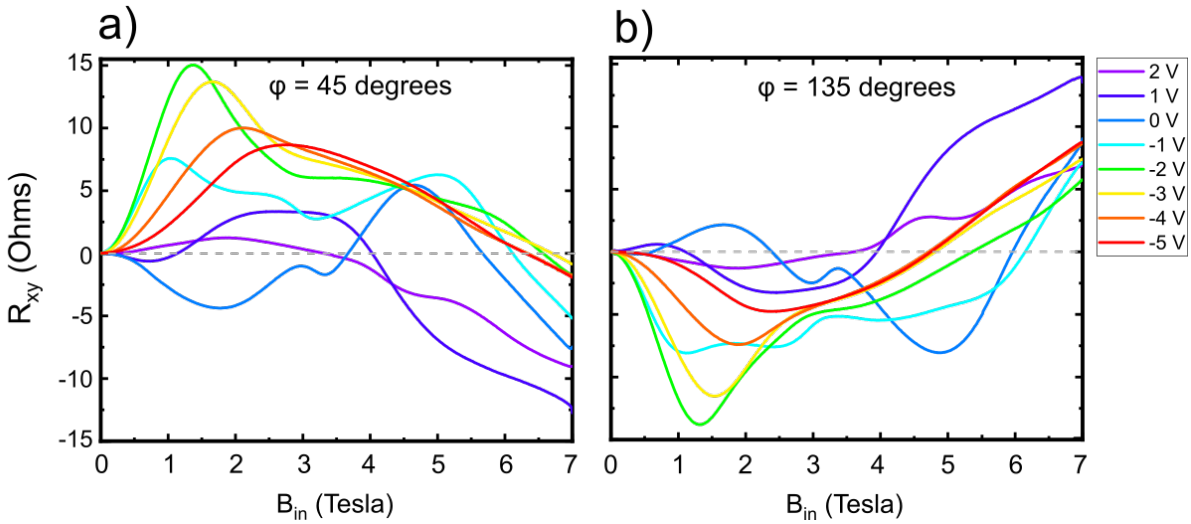

Figure 4.6: Gate dependence of the tranversal resistance R_{xy} in function of the in-plane magnetic field B_{in} for a) $\phi = 45$ degrees and b) $\phi = 135$ degrees.

magnetic field strength, Fig. 4.6b shows that R_{xy} exhibits maximum amplitudes at gate voltages $V_g = -1$ V to -3 V. This is the reason why PHE could not be observed in the far n- ($V_g = 1$ V and 2 V) and p-conducting regimes ($V_g = -4$ V and -5 V) in the measurements presented in Fig. 4.4.

At low magnetic fields ($B_{in} = 0$ T to 2 T) and $\phi = 45$ degrees, the PHE is positive (PHE > 0) for electrical transport dominated by holes (negative gate voltages). Taking $V_g = -2$ V as a representative curve, one notices that the PHE amplitude increases monotonically for in-plane magnetic fields up to $B_{in} \approx = 1.5$ T, then it reaches a maximum value followed by a decrease in its amplitude. Similar behavior is also observed for $V_g = -3$ V to -5 V, however, the main difference between these curves is that the magnetic field strength at which the turning point

occurs depends on the carrier density. Additionally, at $V_g = 0$ V and -1 V, where the carrier density seems to be a minimum (see Fig. 4.2c), the PHE amplitude shows several oscillations. Another interesting feature of the curves presented in Figs. 4.6a and 4.6b is that the PHE amplitude crosses zero value for all carrier densities. Moreover, at high magnetic fields ($B_{in} = 7$ T), PHE has the same sign for all the measured gate voltages.

As already stated, the observation of PHE in 3D topological insulators is very surprising. Moreover, the oscillations in the amplitude of the effect are very puzzling, especially the change in its sign as a function of V_g and B_{in}. Planar Hall effect has already been observed in $Bi_{2-x}Sb_xTe_3$ topological insulator thin films [15]. In that work, the authors attributed the origin of the PHE to the breaking of the time-reversal symmetry by an in-plane magnetic field, which anisotropically lifts the topological protection of surface Dirac fermions from backscattering.

Although the theoretical model of electron scattering of impurities proposed by Taskin et al. predicts the anisotropy of the scattering rates leading to the PHE, the theory model needs a debatable ingredient. According to their argument, *"the uniform magnetic field in a disordered medium with spin-orbit interactions will generate magnetic fields at random positions that can induce spin-flip scattering"*. In their model, the magnetization of the impurities is a necessary condition for the observation of PHE. It is important to note that the material system used to investigate PHE in that work is non-magnetic and/or the presence of magnetic impurities is not mentioned. However, the central argument of that investigation is that the impurities are polarized by an in-plane magnetic field. Moreover, the authors in Ref. [15] also report a monotonic magnetic field dependence of the PHE amplitude, which is in stark contrast with the PHE investigations on the 3D TI HgTe reported here. Such difference could be explained by the different mobilities of both materials. For the n-conducting regime, the mobilities in HgTe can reach values up to $\mu = 300\ 000$ V/(cm)^2, giving an indication of the high quality of material investigated in this thesis.

Alternatively, Nandy et al. addressed the existence of PHE from the perspective of the non-trivial Berry phase and magnetic moments of the 3D topological insulators bulk states [16]. However, such a model is not applicable to experiments involving transport on the topological surface states and, therefore, it does not seem to bring insight into the PHE observations discussed in this thesis.

Another perspective on the observation of PHE in 3D topological insulators is presented in Ref. [17]. In that work, the authors argue that if nonlinear momentum terms (which describe the asymmetry between the electron and hole Dirac cones) are included in the Dirac Hamiltonian, anisotropic backscattering can arise from the tilt of the Dirac cone by the in-plane magnetic field. The proposed model also takes into consideration electron scattering off a strong impurity potential and the magnetic nature of the scatterers is irrelevant for the existence of the PHE. This mechanism seems to be a promising road to explain the origin of PHE in 3D TIs since it is widely

known that a more realistic description of topological insulators Hamiltonian should include the asymmetry between electron and hole branches of the Dirac cone dispersion [18, 19].

Anisotropies in the conductivity were also predicted for two-dimensional electron systems. In 2003, Schliemann and Loss proposed a theory of anisotropic transport in two-dimensional electron gases [20]. According to the authors, the anisotropy in the electrical conductivity can be induced by the interplay between Rashba and Dresselhaus spin-orbit couplings in QWs confined in the (001) direction. If both spin-orbit coupling mechanisms are present in the 2DEG system, the Fermi contours become anisotropic, leading to anisotropies in the electrical conductivity. Moreover, in 2019 Sablikov also proposed that a magnetic field applied in the plane of a two-dimensional system with Rashba SO coupling strongly affects the transport properties and yields anisotropies in the Fermi contours, which in turn lead to anisotropies in the conductance [21].

Although topological surface states and two-dimensional electron gases with Rashba SOC are different systems, both present similar mathematical descriptions. The plausibility of some of the arguments proposed above will be explored at the end of this chapter to address the origin of PHE and MR oscillations (see next section) observed in the 3D TI HgTe.

4.3. Longitudinal MR oscillations in 3D TI HgTe

As briefly mentioned in the previous section, the longitudinal MR in HgTe also shows non-monotonic behavior. Although is very likely that the orbital MR response arising from the out-of-plane magnetic field component contributes to the overall MR, such non-monotonic behavior, here dubbed as MR oscillations, cannot alone be explained by the orbital MR. Hence, this section will show the investigations of these oscillations in detail and attempt to discuss their origin.

4.3.1. MR oscillations of sample Q2830

In order to gain insight into the origin of the PHE oscillations observed in Fig. 4.6, the longitudinal resistance (R_{xx}) of sample Q2830 is measured simultaneously with R_{xy}. The setup used for these measurements is the same as described in Sec. 4.2.3. Note that in this measurement configuration, the misalignment of the sample plane with the magnetic field vector cannot be avoided and, therefore, one cannot separate responses arising from in-plane or out-of-plane magnetic fields.

The longitudinal magnetoresistance is normalized with the following expression:

$$MR(\%) = \frac{R_{xx}(B) - R_{xx}(B=0)}{R_{xx}(B=0)} \tag{4.2}$$

Figures 4.7a and 4.7b show the normalized MR for in-plane magnetic field parallel ($B_{in} \parallel I$) and perpendicular ($B_{in} \perp I$) to the current, respectively. At a first glance, as already observed in the magnetic field dependence of PHE, the longitudinal MR also shows oscillations. This effect is, again, reproducible for other similar devices. It is also clear from Figs. 4.7a and 4.7b that the oscillations in the MR are more pronounced for current parallel to the magnetic field.

At low-densities ($V_g = -2$ V to 0 V) and $B_{in} \parallel I$, the MR oscillations are very pronounced and the amplitude of the oscillations decreases with increasing carrier density. At the lowest carrier density ($V_g \approx 0$ V), the MR amplitude is maximum for $B_{in} \parallel I$ and it decreases on increasing the density of electrons or holes. On the other hand, for $B_{in} \perp I$, the MR is mainly negative in the presence of hole mediated transport and, although the MR oscillates, such oscillations are not so pronounced.

However, one major drawback to the interpretation of these measurements is that the out-of-plane magnetic field component arising from the sample misalignment cannot be avoided in this setup configuration. On the other, the oscillations in the magnetoresistance cannot be explained only by the orbital MR (compare Fig. 4.7 with Fig. 4.2 at $V_g = 0$ V). Therefore, one can assume that

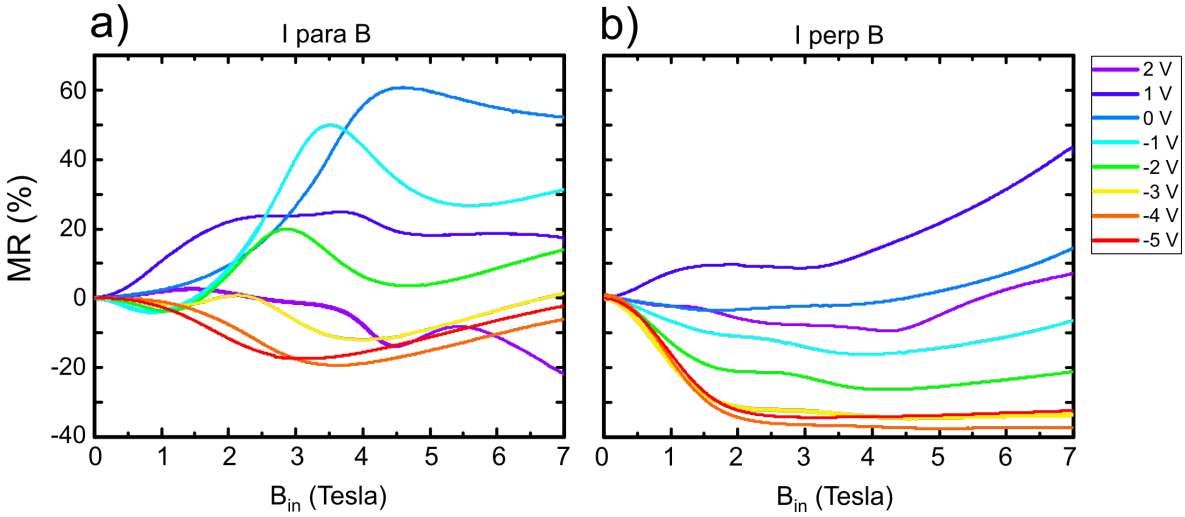

Figure 4.7: Gate dependence of the normalized longitudinal magnetoresistance R_{xx} in function of the in-plane magnetic field B_{in} for a) current parallel ($\phi = 0$ degrees) and b) perpendicular ($\phi = 90$ degrees) to the current. The color code represents different gate voltage values V_g.

the origin of such oscillations does not arise from an out-of-plane magnetic field component due to sample misalignment but, at the same, one cannot quantify its influence in the oscillations.

In order to further investigate this effect, the next section shows measurements of in-plane magnetoresistance in a similar 3D TI HgTe sample where the sample misalignment is minimized and, hence, a better assessment of the MR oscillations due to the in-plane magnetic field can be performed.

4.3.2. MR oscillations of sample Q2761

The device used for these measurements is named Q2761 and it consists of a 90 nm-thick 3D TI HgTe grown on a CdTe substrate, with 50 (10) nm-thick CdHgTe bottom (top) layers. The samples were shaped into a Hall bar geometry as described in Sec. 4.1. Figure 4.8a shows a schematic of the layer stack and Fig. 4.8b shows the gate sweep (R_{xx} at B = 0) along with the device carrier densities n as a guide for the reader to identify n- and p-type transport regimes. Although not shown here, the Hall resistance shows a positive slope at $V_g = 0$ V, while two carrier behavior can be observed at $V_g = -1$ V.

Similarly to the measurements performed in device Q2830 (Sec. 4.2.1), the measurements in device Q2761 were performed by keeping the magnetic field vector/direction constant and rotating the sample plane. However, in this configuration, the sample is rotated in the zx **or** zy plane and allows for the minimization of R_{xy} for $B_{in} \parallel I$ or $B_{in} \perp I$. Here, it is important to clarify that to perform the measurements for in-plane magnetic field parallel or perpendicular to the electric current, the sample has to be removed from the cryostat, changed its configuration and cooled down again. In other words, the measurements presented for device Q2761 for $B_{in} \parallel I$ and

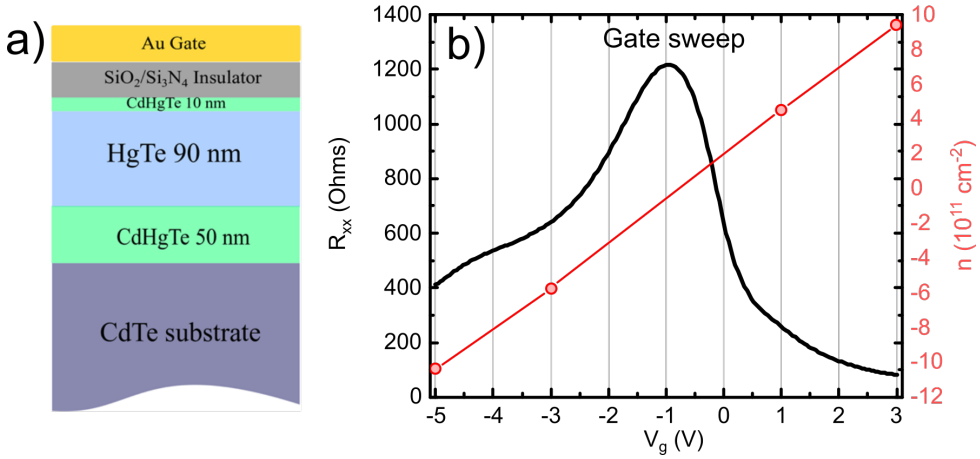

Figure 4.8: a) Schematics of device Q2671. b) Gate dependence of the longitudinal resistance R_{xx} at a magnetic field B = 0, along with the carrier densities n obtained at finite out-of-plane magnetic field.

$B_{in} \perp I$ are not performed in the same cooling cycle. Also, it is important to mention that the measurements were performed only for positive in-plane magnetic fields, hence, an evaluation of the PHE in this device is not possible.

Figure 4.9a-i shows the magnetoresistance of device Q2761 for magnetic field parallel (black lines) and perpendicular (red lines) to the electrical current at different gate voltage values. The data normalized according to Eq. (4.2) is shown in Fig. 4.10 for magnetic field a) parallel and b) perpendicular to the electrical current.

Similarly to sample Q2830, Fig. 4.9 shows that the MR of this device also oscillates with the strength of the in-plane magnetic field, with oscillations more pronounced for magnetic field parallel to the current (see the curve at $V_g = -3$ V for $B_{in} \parallel I$ as an example, where the MR shows three clear minima). Furthermore, one can also observe that the MR also changes its sign and this change has opposite behavior for magnetic field parallel and perpendicular to the current. For example, while the MR for $B_{in} \parallel I$ is initially negative when transport is dominated by electrons (see Fig. 4.9a-c), its sign changes to a positive value for all other carrier densities. In the case of the $B_{in} \perp I$, the MR is positive for all the gate voltage values, except at very high hole densities (see Figs. 4.9h and 4.9i). Figs. 4.10a and 4.10b also show that the MR amplitude reaches its maximum value at low carrier densities (between $V_g = 0$ V and -1 V) and the change in its amplitude is small for high electron or holes densities.

Another interesting feature in this data set is that a "shoulder-like" structure appears at high electron densities (at $V_g = 2$ V and 3 V) and low magnetic fields ($B_{in} \approx 4$ T). Then, this feature disappears with decreasing carrier density. At $V_g = -1$ V, when holes from the camel back band start to contribute the conduction, the shoulder-like structure appears again for $B_{in} \parallel I$, while, simultaneously, a minimum in the oscillations can be seen at $B_{in} \approx 12$ T, which

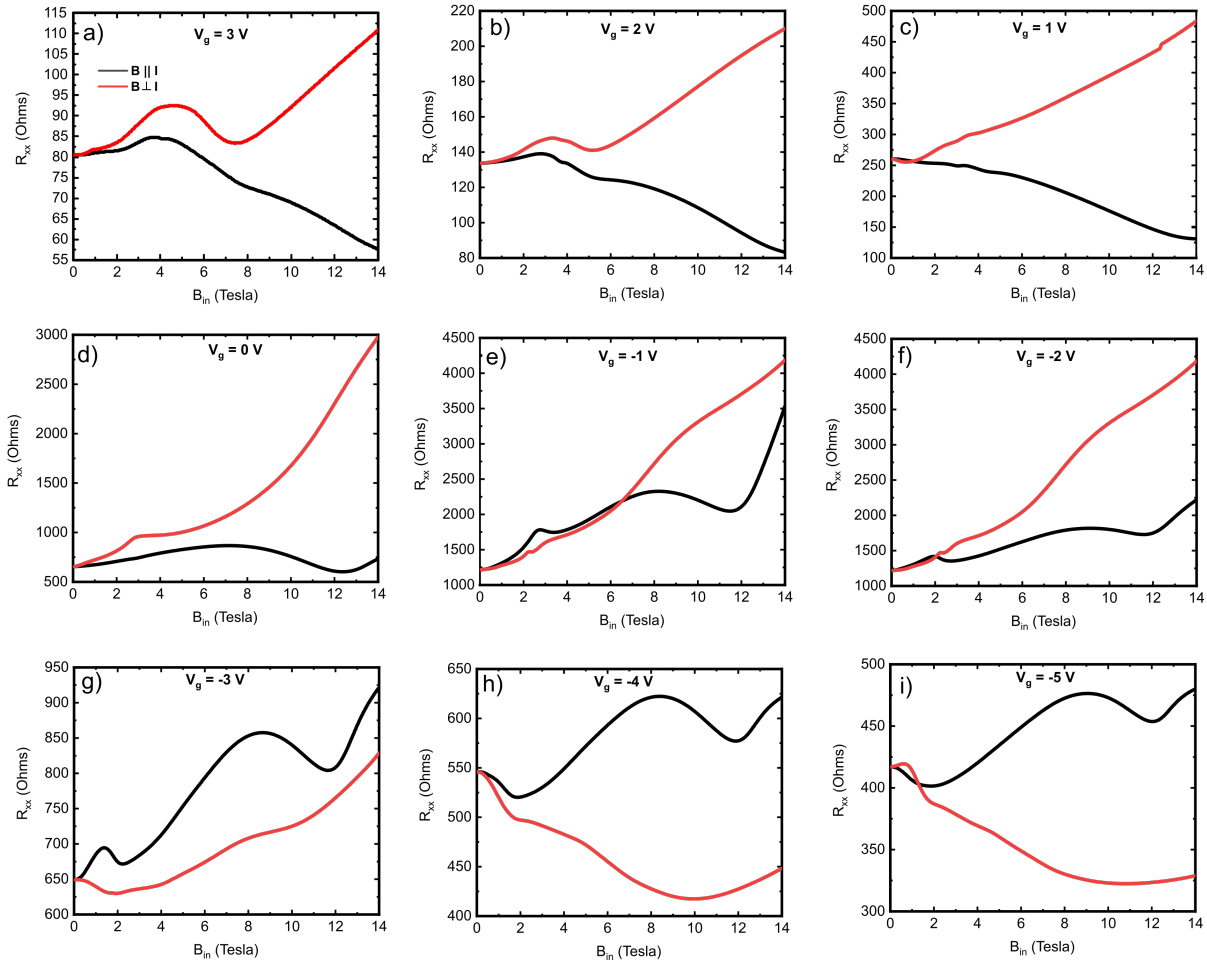

Figure 4.9: Longitudinal MR of sample Q2761 for in-plane magnetic field parallel (black curves) and perpendicular (red curves) to the electrical current from gate voltages a) $V_g = 3$ V to i) $V_g = -5$ V.

is also accompanied of a maximum at $B_{in} \approx 9$ T. These features can be clearly distinguished for magnetic field parallel to the current, however, although oscillations and/or changes in the resistance can be observed for $B_{in} \perp I$, such features are not so pronounced.

Figure 4.11 highlights the normalized MR for magnetic field parallel to the current for gate voltages $V_g = -1$ V to -5 V, i.e., when holes carriers participate in the electrical conduction. On one hand, it is clear that with increasing the hole density the MR amplitude decreases and the shoulder-like structure, initially visible at $B_{in} \approx 4$ T and $V_g = -1$ V moves to lower magnetic fields, until it is not visible anymore (at $V_g \approx -4$ V). On the other hand, the minimum in the MR oscillations located at $B_{in} \approx 12$ T (orange dashed line) almost does not shift with increasing carrier density, which might indicate that these two oscillations, the one at $B_{in} \approx 4$ T and the one at $B_{in} \approx 12$ T have different origins.

As already mentioned, this change in MR cannot be explained by the orbital MR arising from an

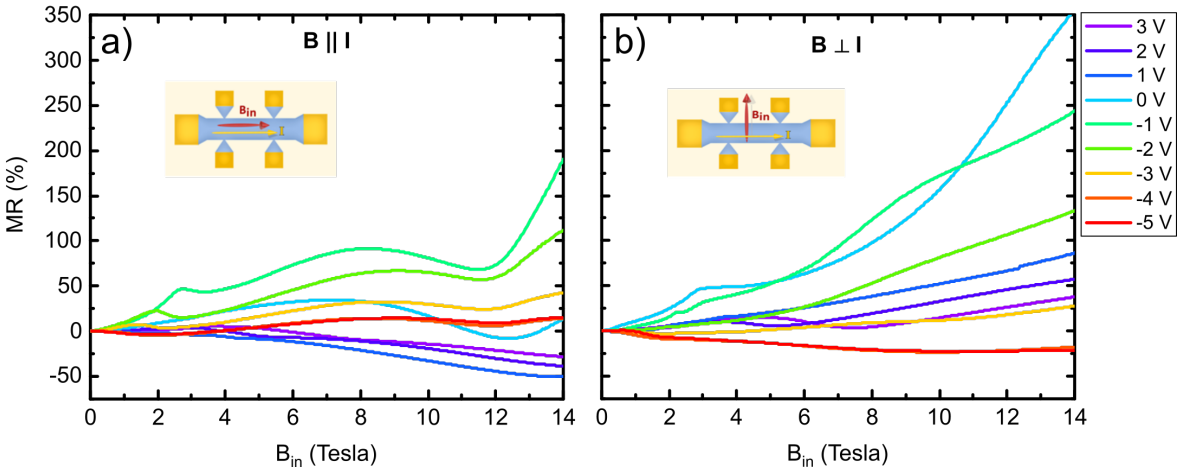

Figure 4.10: Normalized magnetoresistance of sample Q2761 shown in Figure 4.9 for in-plane magnetic field a) parallel and b) perpendicular to the electric current.

out-of-plane magnetic field component. Indeed, the orbital MR due to an out-of-plane magnetic field is positive for all carrier densities range in the HgTe topological insulators [22, 23]. Furthermore, one can also observe that the MR oscillations/features are more pronounced when hole carriers also contribute to the electrical transport. This indicates that the subtleties of the camel back might strongly influence the MR in the presence of an in-plane magnetic field. In any case, the MR oscillations and PHE observed in the 3D topological insulator HgTe are undoubtfully surprising. The reader is also made aware that such oscillations are also observed in the Weyl phase of HgTe and the interested reader is directed to Ref. [24] for further details.

Magnetoresistance oscillations in topological insulators in the presence of an in-plane magnetic field were predicted by Yakovenko et al. [25]. In that work, it is argued that for *thin* 3D TI films, the in-plane magnetic field shifts both top and bottom Dirac cones in k-space, leading to a tunneling probability between both TSS if there is an exact match between their spin and momentum directions. However, this tunneling mechanism would be responsible for only one MR extrema as a function of the in-plane magnetic field and is, therefore, not a good candidate to explain our observations.

Another mechanism, are Weiss oscillations, which happen in the electron regime for in-plane magnetic field *perpendicular* to the electrical current [26]. In this configuration, the radius of the cyclotron orbits resonates with the finite device size and generates an oscillation in the MR. For our devices, we estimate the cyclotron radius given by $R_c = \frac{m^* v_F}{eB}$, where m^* is the electron mass, e is the electron charge and v_F is the Fermi velocity of the carriers [27]. For the p-type transport regime (camel back band) $v \approx 1 \times 10^5$ m/s. With these simple estimations, one finds that the cyclotron radius at $B_{in} \approx 12$ T is $R_c \approx 50$ nm, which is in the same order of magnitude of the 3D TI HgTe typical thicknesses ($d_{HgTe} = 90$ nm). Although Weiss oscillations

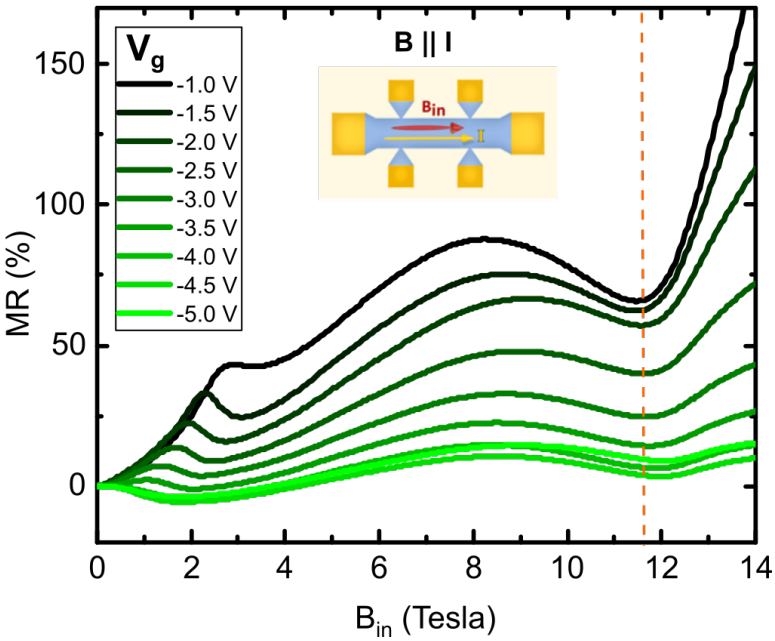

Figure 4.11: Normalized magnetoresistance of sample Q2761 shown in Figure 4.9 $B_{in} \parallel I$ and gate voltages V_g = -1 V to -5 V. The orange dashed line highlights the minimum in the MR oscillations at $B_{in} \approx 12$ T.

should occur for $B_{in} \perp I$, the 12 T feature appears for $B_{in} \parallel I$. Although in the investigations performed in this thesis the magnetic field the radius of the cyclotron orbits is comparable to the device dimensions, Weiss oscillations do not seem to be a good candidate to explain our measurements, since the oscillations studied here are more pronounced for $B_{in} \parallel I$ and more than one oscillation is observed in the p-type transport regime. On the other hand, it is quite surprising that the radius of the cyclotron orbits is comparable to the device size for $B_{in} \approx 12$ T, which could indicate that the finite device size could play a role in the MR of the 3D TI HgTe in the presence of B_{in}. Therefore, further investigations are required to acquire a better picture of the influence of finite size effects in the MR oscillations of 3D TI HgTe. A more promising mechanism, observed in 1993, involves the depopulation of spin subbands in systems exhibiting Rashba spin-orbit coupling [28]. In wide AlGaAs parabolic quantum wells MR oscillations were observed for hole-dominated transport for $B_{in} \parallel I$. The data is shown in Fig. 4.12, where one can observe several minima in the longitudinal resistance, labeled by arrows indicating the subbands E_2 and E_3. In this work, the MR oscillations were explained by the depopulation of the hole subbands, which is induced by the in-plane magnetic field. Several works by the same group have also reported changes in the slope of the MR $B_{in} \parallel I$ and $B_{in} \perp I$ [29, 30].

As the reader already concluded, there are two main phenomena observed in the 3D TI HgTe that need a clear explanation: (i) the origin of the planar Hall effect accompanied by oscillations in its amplitude and (ii) the oscillations in the longitudinal magnetoresistance. Although there

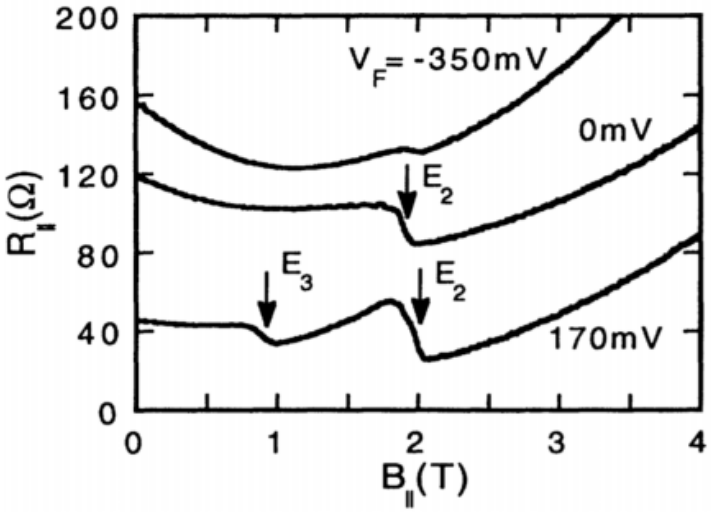

Figure 4.12: Longitudinal MR (here labelled as $R_{\parallel}$) of a remotely doped wide AlGaAs parabolic quantum well measured in function an the in-plane magnetic field $B_{\parallel}$ perpendicular to the current at different gate voltages U_g. The arrows indicate the several minima in the MR, which correspond to the depopulation of the subbands labelled as E_i. The middle trace ($U_g = 0$) is shifted up by 60 Ω for clarity. Figure taken from [28]

are several reported mechanisms aiming to explain the origin of the PHE and the MR oscillations in topological insulators, they do not provide a clear insight into the observations reported in this thesis. One can, however, make use of some of these models and modify them to explain the physical origin of the puzzling galvanomagnetic effects observed in the 3D TI HgTe. The most promising of these mechanisms involves the coupling of the in-plane magnetic field with Rashba.

However, before making use of this model and applying it into the context of topological insulators, the reader is made aware of a few new results concerning the transport properties of the 3D TI HgTe. As discussed in detail in references [4, 24], the observation of QHE in the hole transport regime (see the measurements in Refs. [3, 4]) cannot be attributed to the "hole branch" of the Dirac cone, since the Dirac point in the 3D TI HgTe is buried into the valence band [23]. The hole transport is, however, attributed to massive Volkov-Pankratov states (VPS), which are quasi-two-dimensional states arising from the localization of the hole carriers in the valence band by the gate voltage potential. In this case, the first hole subband is shifted towards the top surface, separating itself from the other subbands, thus, allowing the observation of QHE in the p-type transport regime [4]. These massive VPS are not topological, but rather than trivial surface states.

Thus, one could attempt to explain the MR oscillations in the p-type transport regime using the coupling of the in-plane magnetic field with a system exhibiting Rashba-like SOC. However, one major drawback in this direction lies in the complications of the p-type transport regime in HgTe. Although Winkler predicted that Rashba SO coupling in heavy-hole systems is $\propto \beta k_{\parallel}^3$ (see Sec. 2.2.2), Zhang et al. showed that in inverted QWs the heavy-hole-like subband H1 energy splitting

ΔE_{H1} is initially proportional to $\beta k_{\parallel}^3$, but it saturates and even decreases for large k-values [31], as shown in Fig. 4.13. The Rashba splitting in such devices can reach values up to 30 meV [31–33], which is about three times larger than the splitting in III-V narrow-gap semiconductors, where values of approximately 10 meV have been reported [34, 35]. The complicated dependence of the Rashba splitting in the hole regime of HgTe makes it difficult to make use of simple toy models based on the linear Rashba spin splitting (as the one proposed in Ref. [17]) to predict the rich and complex behavior of the PHE and MR oscillations in tensile strained HgTe. In this case, band structure calculations are the most suitable tool to make a proper assessment of the galvanomagnetic effects investigated in this thesis.

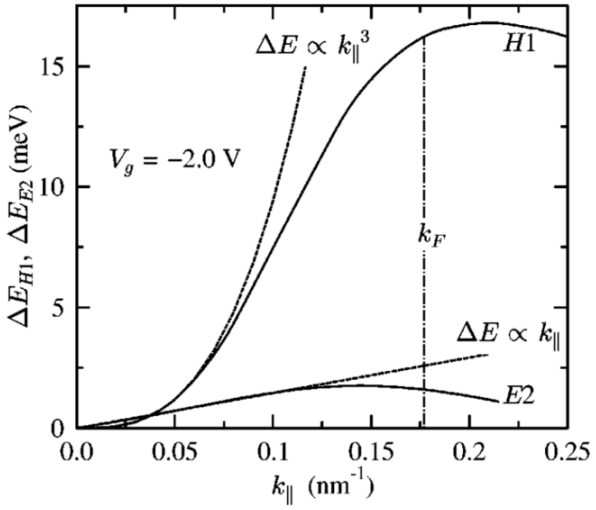

Figure 4.13: The calculated spin splitting energy of the H1 and E2 subbands (solid curves), ΔE_{H1} and ΔE_{H2} in function of the in-plane wave vector $k_{\parallel}$. The position of the Fermi wave-vector k_F is denoted by the dotted-dashed line. The dashed lines indicate that ΔE_{H1} and ΔE_{H2} are proportional to $\beta k_{\parallel}^3$ and $k_{\parallel}$ respectively, at small $k_{\parallel}$.. Figure taken from [31]

Based on the discussions above there are a few directions worth exploring:

- As pointed out by Schliemann and Loss, the interplay between Rashba and Dresselhaus in 2DEGs can lead to anisotropic Fermi contours, which in turn can lead to anisotropies in the electrical conductivity [20]. In this case, one can investigate if a combination of SIA/BIA can lead to anisotropies in the band structure of the 3D TI HgTe that could explain the planar Hall effect.

- Given that the interplay between Rashba SO coupling and in-plane magnetic field can also distort the Fermi contours and lead to anisotropies in the electrical conductivity [21], one can also explore how the interplay between in-plane magnetic field, Rashba and Dresselhaus influences the band structure of HgTe.

These directions will be explored in the next section in order to investigate in detail the origin of the PHE and the MR oscillations in the 3D TI HgTe.

4.4. Band structure effects

As already discussed in Sec. 2.4.1, in ferromagnetic systems PHE emerges due to the anisotropic scattering rates of the conduction carriers when the magnetic field is applied parallel or perpendicular to the electrical current. In paramagnetic materials, Goldberg and Davis have suggested that PHE should arise if the Fermi contours are non-spherical in k-space [5]. Schliemann and Loss have suggested that the interplay of Rashba and Dresselhaus SO couplings in 2DEGs cause the Fermi contours to be anisotropic which, in turn, leads to anisotropies in the conductivity [20]. Sablikov has proposed that the interplay of Rashba SO coupling and in-plane magnetic field also leads to anisotropies in the Fermi surface and electrical conductance [21]. When it concerns the magnetoresistance of 2DEGs, magnetoresistance oscillations in these systems were explained by the interplay of the Rashba SO coupling and in-plane magnetic field, which causes the depopulation of one of the spin subbands and, consequently, the MR shows an oscillation [28–30].

The common ingredient in the proposed explanations for PHE relies on the anisotropy of the Fermi contours, either induced by SO interactions or by an interplay of in-plane magnetic field and Rashba SO coupling. Although at present moment it is still not clear if the PHE and MR oscillations have the same origin, this section aims to look in detail into the band structure of the 3D TI HgTe to analyze if anisotropies are present in the material system. Moreover, considering the several predictions on the interplay of SOC and in-plane magnetic field to explain PHE, this section also aims to perform $\vec{k} \cdot \vec{p}$ calculations considering the HgTe band structure, BIA-, SIA-like SO couplings and in-plane magnetic field in order to assess if these interactions modify the material band structure and the energy scales necessary to observe the effect. Finally, a thorough discussion of the relevant length scales involved in our observations is provided, in order to gain insight into the potential routes that can be followed to explain PHE and MR oscillations in the 3D TI HgTe.

4.4.1. In-plane anisotropy

We consider band structure effects calculated from a $\vec{k} \cdot \vec{p}$ model in a 30 nm-thick HgTe quantum well (confined and discretized in the z direction and infinite in the (x, y) directions) using a basis of 8 orbitals [1]. Figure 4.14 shows the Fermi contours of several energy cuts for the a-b) topological surface states bands and c-d) for the camel back band. The red and blue colors represent the spin component in the z direction and the "+" and "−" labels represent both spin directions. Since both components are initially two degenerate states, a small spin splitting is added to distinguish between these two states. In this figure, $k_x \parallel [100]$ and $k_y \parallel [010]$ crystal orientations. The Hall bar devices used for the PHE and MR investigations performed in this

[1] I thank W. Beugeling for kind assistance with the calculations and for providing the plots of Figs. 4.14 and 4.15.

thesis were fabricated in the [110] or [$\bar{1}$10] directions, or in other words, 45 degrees away from k_x or k_y directions. The directions representing the orientation of the Hall bars (and, therefore, the direction of the electrical current) will be labeled as k'_x and k'_y. From the contour plots (dispersions $E(k_x, k_y)$) calculations shown in Fig. 4.14, one observes that while the topological surface states show approximately isotropic Fermi contours, the camel back band displays anisotropic Fermi contours symmetric under a rotation of 90 degrees.

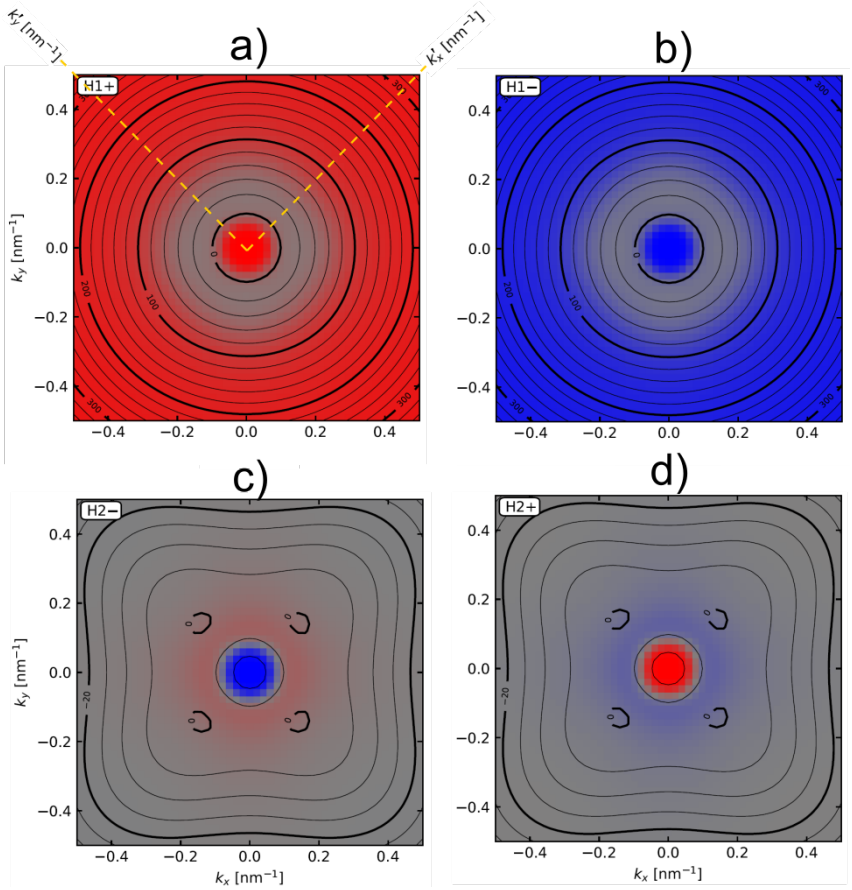

Figure 4.14: Fermi surfaces of a 30 nm-thick 3D TI HgTe obtained via $\vec{k} \cdot \vec{p}$ calculations for a-b) topological surface state and c-d) camel back bands. The red and blue colors represent the spin component in the z direction. Here, $k_x \parallel [100]$, $k_y \parallel [010]$, $k'_x \parallel [110]$ $k'_y \parallel [\bar{1}10]$.

Considering that anisotropic Fermi contours are one of the key ingredients to observe PHE in a material system [5, 7], one could conclude from the band structure of the 3D TI HgTe in Fig. 4.14 that PHE would not be observed when transport is dominated by the TSS bands since their Fermi contours are (approximately) isotropic. Similarly, although the camel back band Fermi contours are anisotropic in k-space (Fig. 4.14c-d), one also observes that these bands would also do not meet the requirement to observe PHE. The camel back band does not show an asymmetry under a rotation of 90 degrees or, in other words, does not show an anisotropy along the k'_x and k'_y crystal orientations. These calculations bring the information that the band structure of the 3D TI HgTe alone does not satisfy the conditions to observe PHE in this material system and,

thus, one needs to find mechanisms that break the 90 degrees anisotropy of the camel back band or the isotropy of the topological surface state bands.

One possibility to break the isotropy of the TSS bands or the 90 degrees anisotropy of the camel back band is to flow an electrical current along the [110] *or* [1$\bar{1}$0] directions. Using simple estimations based on the parameters used in our experiments, the asymmetry induced in the bands due to the application of an electric field is neglegible. For instance, a current density $j = 5 \times 10^{-4}$ A/m and drift velocity $v_d = \frac{j}{ne} \approx 1$ m/s, leads to a displacement of the Fermi contours in k-space of $\delta k = \frac{v_d m^*}{\hbar} \approx 1 \times 10^{-5}\,\mathrm{nm}^{-1}$. Here, $n \approx 3 \times 10^{-11}\,\mathrm{cm}^{-2}$, $m^* = 9 \times 10^{-31}\,\mathrm{kg}$ and $\hbar = 1.05 \times 10^{-34}$ Js. This δk value leads to an energy difference of $\delta E = \frac{\hbar^2 \delta k^2}{2m^*} \approx 4 \times 10^{-12}\,\mathrm{eV}$, which cannot be resolved experimentally. Therefore, one can also conclude that an electrical current does not give rise to measurable anisotropies between the k'_x and k'_y crystal directions.

Another two promising candidates for breaking the symmetry between the k'_x and k'_y crystal orientations are the interplay between SIA and BIA SO couplings [20] and the interplay between SIA SO coupling and in-plane magnetic fields [21].

In order to evaluate if linear in $k_\parallel$ SIA- and BIA-like couplings to the band structure may originate anisotropies in the Fermi contours of the TSS or camel back bands, dispersions have been calculated with similar parameters as introduced in the previous section. Here, however, the coupling of BIA-like and SIA-like SO interactions with the 3D TI HgTe band structure is also taken into consideration. The resulting Fermi contours are shown in Fig. 4.15 for a-b) topological surface state and c-d) camel back bands. The arrows in the figure represent the spin component in the (x, y) directions.

In Fig. 4.15a-b, one observes that the presence of BIA- and SIA-like couplings hardly affects the Fermi contours of the TSS bands, which remain mostly isotropic. For these bands, the spin orientations at low energies resemble the ones of linear Rashba SO coupling (see Fig. 2.2) however, at high energies the spin orientations form a complicated pattern. The fact that BIA- and SIA-like couplings hardly affect the TSS bands might be explained by the orbital character of these bands, which are mostly s-orbitals and present very small or negligible spin-orbit coupling [36] (see Sec. 2.2.2).

The situation is, however, different for the camel back band. Figures 4.15c-d, which present the Fermi contours for the camel back band for both spin directions, clearly shows that the BIA- and SIA-like couplings significantly deform the Fermi contours along the [110] and [$\bar{1}$10] crystal orientations. This deformation leads to different k-values for the Fermi contours along k'_x and k'_x directions, which breaks the 90 degrees symmetry of the camel back band and gives rise to an anisotropy of the contour with 180 degrees periodicity. The directions where the elongation of the Fermi surface occurs are consistent with directions parallel or perpendicular to the Hall bar orientation of devices ([110] *or* [1$\bar{1}$0] directions). Experimentally, the amplitude of the SIA-like

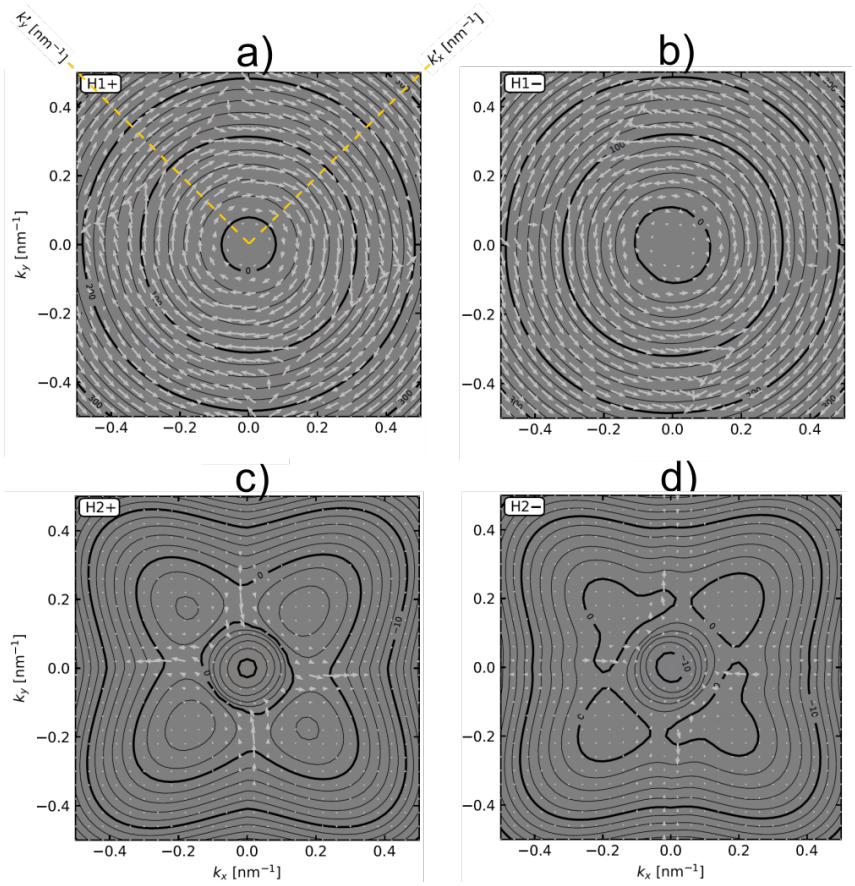

Figure 4.15: Fermi surfaces of a 30 nm thick 3D TI HgTe in the presence of BIA- and SIA-like SO interactions for a-b) topological surface state and c-d) camel back ($\Gamma_{8,HH}$) bands. The arrows in the figure represent the spin component in the (x, y) directions. Here, $k_x \parallel [100]$, $k_y \parallel [010]$, $k'_x \parallel [110]$ and $k'_y \parallel [\bar{1}10]$.

coupling can be controlled by the top gate electrode, while the BIA-like one is an intrinsic property of the material and, therefore, is constant [36]. In HgTe quantum wells, where the spin splitting is large (up to 30 meV) [32], the BIA term is considered to be negligible [37], however, a precise quantification is still lacking.

Nevertheless, the main message these considerations bring is that, in the presence of BIA and SIA SO couplings, the Fermi contours of the camel back band of the 3D TI HgTe become anisotropic. Whilst it is long known that in realistic HgTe systems the spin-splitting due to the Rashba SO coupling is not linear ($\propto k_{\|}$) [31, 32], the calculations performed above provide the motivation to further investigate the consequences that such couplings would have in the band structure.

4.4.2. Estimations of magnetic field effects

Although anisotropies in the Fermi contours are a necessary condition for the observation of PHE, the experiments are conducted in the presence of an in-plane magnetic field. Therefore, the magnetic field is another ingredient that should be added to the calculations. In the following, it

will be shown that, although the interplay between BIA, SIA and in-plane magnetic field modifies the band structure of HgTe, the in-plane magnetic field amplitudes needed to observe such effects differ up to an order of magnitude in comparison to the experiments.

The $\vec{k} \cdot \vec{p}$ calculations using the 6×6 Kane Hamiltonian[2] involve a 70 nm thick quantum well including the BIA-like term, the Hartree potential U_{gate} and the Zeeman energy splitting B_0 (in units of eV) due to an in-plane magnetic field B (in units of T). Here, $\phi = 0$ degrees for $B_0 \parallel k_x$ and $B_0 = g\mu_B B$ and $g = 20 \pm 5$ [38].

Figure 4.16a shows the energy dispersion at zero in-plane magnetic field ($B_0 = 0$ eV) at $U_{gate} = 0$ V and $\phi = 0$ degrees. The colors represent surface localization. The conduction and valence (camel back) subbands are shown in grey, while the top and bottom topological surface states are indicated in the figure by red and blue colors, respectively. At $U_{gate} = 0$ V, the top and bottom surface are degenerate, however, as shown in Fig. 4.16b, the application of a surface potential ($U_{gate} = 1$ V) breaks this degeneracy. By applying a magnetic field of amplitude $B_0 = 0.01$ eV, one does not observe many differences in the band structure for magnetic field parallel (Fig. 4.16c for $\phi = 0$ degrees) and perpendicular to the k_x-direction (Fig. 4.16d for $\phi = 90$ degrees). However, Figs. 4.17a-e) shows that a magnetic field amplitude of $B_0 = 0.05$ eV does modify the band structure. Indeed, the energy dispersion looks significantly different for $\phi = 0$ (Fig. 4.17a) and $\phi = 90$ degrees (Fig. 4.17c). For this magnetic field strength, one can observe crossings between the TSS and what it seems to be subbands from the conduction or camel back bands.

These results might indicate that the crossings observed in Figs. 4.17b-d could be a potential candidate to explain the MR oscillations previously discussed in this chapter. Depending on the position of the Fermi energy, differences in the DoS and/or depopulation of subbands could lead to the oscillations observed in the MR of our devices. Although these band structure calculations show a rich behavior that is dependent on the amplitude of the in-plane magnetic field and its direction, the magnetic field amplitudes needed for the crossings to occur are very high and do not seem to be realistic in explaining the investigations carried out in this thesis. For instance, $B_0 = 0.01$ eV corresponds to a magnetic field amplitude of $B \approx (8.6 \pm 2.2)$ T using $g = 20 \pm 5$. For $B_0 = 0.05$ eV, unrealistic magnetic fields as high as $B \approx (43 \pm 11)$ T are needed. Since oscillations in the MR can be visible for magnetic fields as low as $B_{in} = 3$ T (see Fig. 4.11), the magnetic field amplitudes required to observe effects in the band structure differ up to one order of magnitude when compared to the experiments.

Moreover, the Zeeman energy splitting observed here is in the order of a few meV and is comparable to the size of the bandgap (between 10 and 25 meV [22, 23]). Thus, to achieve an energy splitting comparable to the bandgap of the 3D TI HgTe, one would require $gB \approx 200$ T, which necessitates either high magnetic field amplitudes or high g-factors. The reader is made aware that the g-factor used here ($g = 20 \pm 5$) is the *effective* value reported in the literature [38].

[2] I thank J.-B Mayer for kind assistance with the calculations and providing the plots of Figs. 4.16 and 4.17.

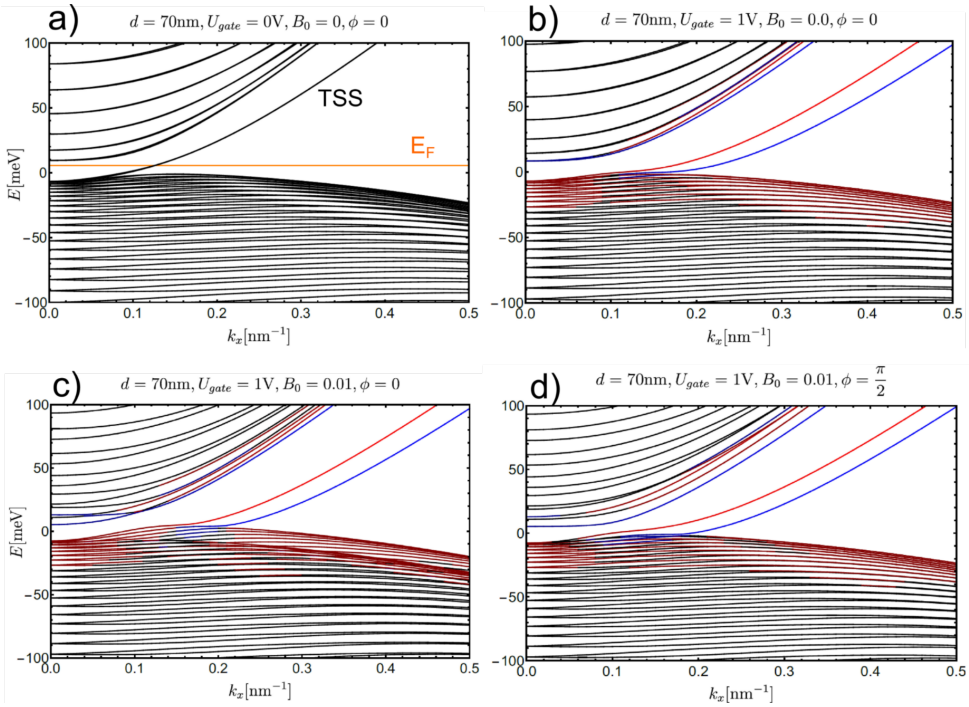

Figure 4.16: Dispersion of the 3D TI HgTe as a function of in-plane magnetic field angle a) without and b) with surface potential. The color code indicates top and bottom surface localization. c) Dispersions with surface potential ($U_{gate} = 1$ V) and in-plane magnetic field amplitude $B_0 = 0.01$ eV at $\phi = 0$ degrees and d) $\phi = \pi/2 = 90$ degrees.

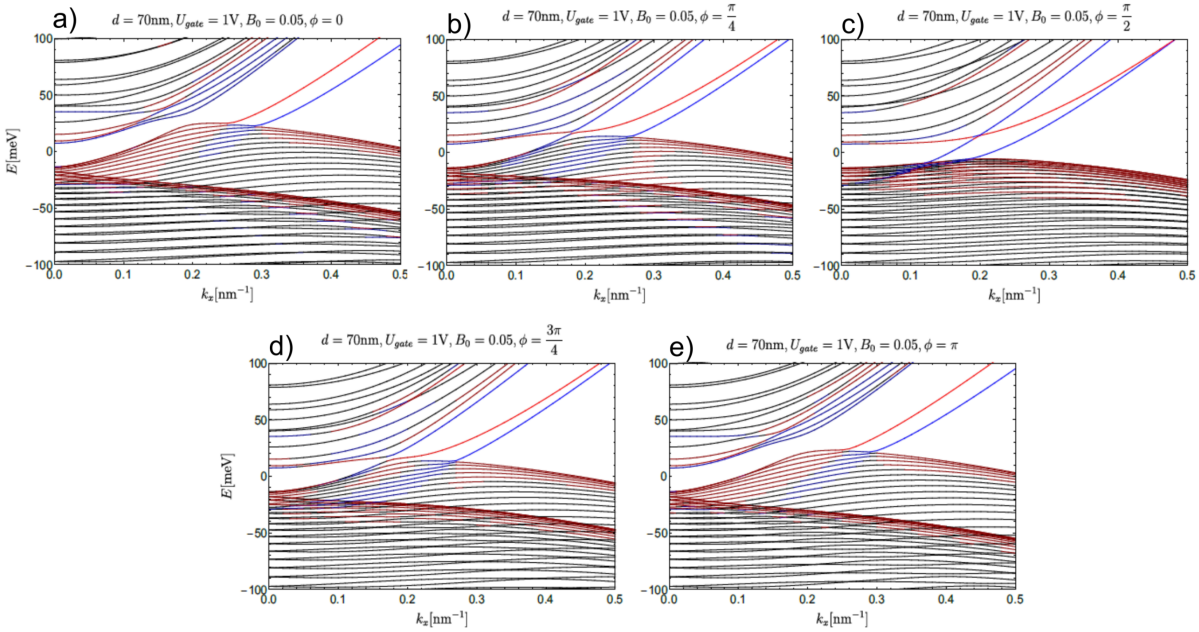

Figure 4.17: a-e) Band structure calculations in the in the 3D TI HgTe as a function of in-plane magnetic field angle ϕ with surface potential of $U_{gate} = 1$ V and field strength $B_0 = 0.05$ eV.

Hence, despite the fact that one can show from these results that an in-plane magnetic field affects the band structure of the 3D TI HgTe, the magnetic field amplitudes required to experimentally observe such effects are very high. Therefore, the Zeeman-like coupling (plus BIA and SIA) with the band structure is unlikely to explain the PHE and MR oscillations we observe in the transport measurements reported in this chapter since one can observe MR oscillations for magnetic fields as low as 2 T. Concerning the PHE, the $\vec{k} \cdot \vec{p}$ calculations already signaled that anisotropies will occur in the band structure of the camel back band in the presence of SIA and BIA SO interactions. On the other hand, although these results seem to be promising, preliminary calculations of the DoS as a function of the in-plane magnetic field amplitude and direction (not shown here) are, so far, not conclusive: such calculations do not provide strong signatures of different DoS for in-plane magnetic field parallel and perpendicular to the electrical current.

4.5. Conclusions and perspectives

In this chapter, galvanomagnetic effects in the 3D TI HgTe were investigated. The samples used for the experiments were electrically characterized and quantities, such as the mobility and the concentration of the carriers, were obtained. When it comes to measurements involving in-plane magnetic fields, the reader became aware that the alignment between the sample and the magnetic field rotation planes is a crucial parameter for the proper investigation of the magnetoresistance response of the 3D TI sample and the experimental alignment procedure was described in detail.

This chapter showed that the transversal resistance R_{xy} of the 3D TI HgTe is not constant upon rotation of the in-plane magnetic field. R_{xy} shows an anisotropy $\propto \cos\phi \sin\phi$ for a wide range of carrier densities, an effect known as planar Hall effect. The amplitude of the PHE oscillates with increasing the magnetic field. Similar behavior was also be observed for the longitudinal resistance R_{xx}, which also oscillates with increasing in-plane magnetic field for all the carrier density ranges studied here. These effects are robust, i.e., observed in several similar samples and the oscillations cannot be explained by the orbital MR from an out-of-plane magnetic field component arising from the misalignment between the sample and magnetic field rotation planes.

Several theoretical models to explain the PHE and the oscillations in the MR were discussed. In the case of PHE, the model proposed in reference [15], which attributes the origin of the PHE to the anisotropic lifting of the topological protection of the surface Dirac fermions from backscattering, needs as an ingredient the magnetization of the impurities of the sample. This model does not seem to be applicable to our devices, since the samples investigated here are non-magnetic and display high mobilities. A more promising mechanism is presented in Ref. [17], where the authors argue that PHE can originate from the interplay of the in-plane magnetic field and a modified Dirac Hamiltonian that includes the asymmetry between the electron and hole of the Dirac cone branches. Further investigations in this direction are being conducted by our collaborators.

This chapter also discussed that the interplay between BIA, SIA and in-plane magnetic field can cause anisotropies in the Fermi contours, which can lead to anisotropies in the band structure of a 2DEG [20, 21]. Band structure calculations based on 6-orbitals were able to show that, although the band structure of HgTe becomes anisotropic in the presence of BIA and SIA, the magnetic fields required to experimentally observe such anisotropies are as high as 40 T, i.e., one order of magnitude higher in comparison to the experiments reported here. Additionally, the reader is made aware that connecting simple models to the band structure calculations might be challenging. For example, the SIA terms are often assumed to be linear $\propto k$, however, as shown in Ref. [38], in the p-type transport regime of HgTe QWs the Rashba term is not linear but rather shows a $\propto k^3$ dependence that saturates at high k-values. Moreover, although not reported in this

thesis, preliminary calculations attempting to investigate if there is a difference in the DoS for magnetic field parallel or perpendicular to the electrical current were, so far, inconclusive.

For the oscillations observed in the longitudinal MR, the results showed that the effect is more pronounced for $B_{in} \parallel I$ and at low carrier densities. Calculations of cyclotron radius R_c for a magnetic field strength $B_{in} \approx 12$ T indicate that, at this field value, the cyclotron radius $R_c \approx 50$ nm, which is in the same order of magnitude as the size of the devices investigated here. Therefore, further investigations are required to acquire a better picture of the influence of finite size effects in the MR oscillations of 3D TI HgTe.

Concerning future investigations, one avenue worth exploring involves investigations of HgTe/CdTe quantum wells in the presence of in-plane magnetic fields. Although these systems are not 3D TIs, they can be 2D TIs and also present topological properties [39]. Given the fact that it is not clear if the PHE has a topological origin, measurements of the transversal resistance R_{xy} in QWs with inverted and non-inverted band alignment might provide insights into the topological origin of the PHE. Moreover, since the HgTe/CdTe QW thicknesses are about one order of magnitude smaller than in the 3D TIs, investigations in these systems might also provide information on the cyclotron radius resonating with the device size.

As the reader can conclude, the galvanomagnetic effects discussed in this chapter are rich and its intricacies are extremely puzzling. Although one can find mechanisms that explain the anisotropy in the magnetoresistance of 3D TIs [15–17], finding a mechanism that *simultaneously* explains the PHE, the gate dependence, and the oscillations in the magnetoresistance of the 3D TI HgTe as a function of the in-plane magnetic field is the hard task of these investigations and a challenge that still needs to be overcome.

References

[1] W. Thomson, "On the Electro-dynamic Qualities of Metals: Effects of Magnetization on the Electric Conductivity of Nickel and of Iron," *Proc. Royal Soc. Lond.*, vol. 8, pp. 546–550, 1857.

[2] R. C. O'Handley, *Modern magnetic materials: principles and applications.* New York: Wiley, 1999.

[3] A. Jost, M. Bendias, J. Böttcher, E. Hankiewicz, C. Brüne, H. Buhmann, L. W. Molenkamp, J. C. Maan, U. Zeitler, N. Hussey, and S. Wiedmann, "Electron-hole asymmetry of the topological surface states in strained HgTe," *Proceedings of the National Academy of Sciences of the United States of America*, vol. 114, no. 13, pp. 3381–3386, 2017.

[4] D. M. Mahler, V. L. Müller, C. Thienel, J. Wiedenmann, W. Beugeling, H. Buhmann, and L. W. Molenkamp, "Massive and topological surface states in tensile strained HgTe." 2020.

[5] C. Goldberg and R. E. Davis, "New galvanomagnetic effect," *Physical Review*, vol. 94, no. 5, pp. 1121–1125, 1954.

[6] J. P. Jan, *Solid State Physics, Vol. 5.* Academic Press Inc., New York, 1957.

[7] T. R. Mcguire and R. I. Potter, "Anisotropic Magnetoresistance in Ferromagnetic 3D Alloys," *IEEE Transactions on Magnetics*, vol. 11, no. 4, pp. 1018–1038, 1975.

[8] A. Sulaev, M. Zeng, S. Q. Shen, S. K. Cho, W. G. Zhu, Y. P. Feng, S. V. Eremeev, Y. Kawazoe, L. Shen, and L. Wang, "Electrically tunable in-plane anisotropic magnetoresistance in topological insulator $BiSbTeSe_2$ Nanodevices," *Nano Letters*, vol. 15, pp. 2061–2066, 2015.

[9] C. W. J. Beenakker and H. van Houten, "Quantum Transport in Semiconductor Nanostructures," *Solid State Physics*, vol. 44, pp. 1–228, 1991.

[10] S. Datta, *Electronic Transport in Mesoscopic Systems.* Cambridge University Press, 1995.

[11] R. Singha, S. Roy, A. Pariari, B. Satpati, and P. Mandal, "Planar Hall effect in the type-II Dirac semimetal VAl_3," *Physical Review B*, vol. 98, no. 081103(R), pp. 1–6, 2018.

[12] P. Li, C. H. Zhang, J. W. Zhang, Y. Wen, and X. X. Zhang, "Giant planar Hall effect in the Dirac semimetal $ZrTe_{5-\delta}$," *Physical Review B*, vol. 98, no. 121108, pp. 1–7, 2018.

[13] N. Kumar, S. N. Guin, C. Felser, and C. Shekhar, "Planar Hall effect in the Weyl semimetal GdPtBi," *Physical Review B*, vol. 98, no. 041103(R), pp. 1–4, 2018.

[14] H. Li, H. W. Wang, H. He, J. Wang, and S. Q. Shen, "Giant anisotropic magnetoresistance and planar Hall effect in the Dirac semimetal Cd3As2," *Physical Review B*, vol. 97, no. 201110(R), pp. 1–6, 2018.

[15] A. A. Taskin, H. F. Legg, F. Yang, S. Sasaki, Y. Kanai, K. Matsumoto, A. Rosch, and Y. Ando, "Planar Hall effect from the surface of topological insulators," *Nature Communications*, vol. 8, no. 1340, pp. 1–7, 2017.

[16] S. Nandy, A. Taraphder, and S. Tewari, "Berry phase theory of planar Hall effect in topological insulators," *Scientific Reports*, vol. 8, no. 14983, pp. 1–9, 2018.

[17] S.-H. Zheng, H.-J. Duan, J.-K. Wang, J.-Y. Li, M.-X. Deng, and R.-Q. Wang, "Origin of planar Hall effect on the surface of topological insulators: Tilt of Dirac cone by an in-plane magnetic field," *Physical Review B*, vol. 101, pp. 1–6, jan 2020.

[18] D. Culcer, E. H. Hwang, T. D. Stanescu, and S. Das Sarma, "Two-dimensional surface charge transport in topological insulators," *Physical Review B*, vol. 82, no. 155457, pp. 1–17, 2010.

[19] A. A. Taskin, Z. Ren, S. Sasaki, K. Segawa, and Y. Ando, "Observation of dirac holes and electrons in a topological insulator," *Physical Review Letters*, vol. 107, no. 016801, pp. 1–4, 2011.

[20] J. Schliemann and D. Loss, "Anisotropic transport in a two-dimensional electron gas in the presence of spin-orbit coupling," *Physical Review B*, vol. 68, no. 165311, pp. 1–9, 2003.

[21] V. A. Sablikov and Y. Y. Tkach, "Van Hove scenario of anisotropic transport in a two-dimensional spin-orbit coupled electron gas in an in-plane magnetic field," *Physical Review B*, vol. 99, no. 035436, pp. 1–8, 2019.

[22] C. Brüne, C. X. Liu, E. G. Novik, E. M. Hankiewicz, H. Buhmann, Y. L. Chen, X. L. Qi, Z. X. Shen, S. C. Zhang, and L. W. Molenkamp, "Quantum Hall effect from the topological surface states of strained bulk HgTe," *Physical Review Letters*, vol. 106, no. 126803, pp. 1–4, 2011.

[23] C. Brüne, C. Thienel, M. Stuiber, J. Böttcher, H. Buhmann, E. G. Novik, C. X. Liu, E. M. Hankiewicz, and L. W. Molenkamp, "Dirac-screening stabilized surface-state transport in a topological insulator," *Physical Review X*, vol. 4, no. 041045, pp. 1–6, 2014.

[24] D. Mahler, *Surface states of the topological insulator and Dirac semi-metal strained HgTe*. PhD thesis, Julius-Maximilians-Universität Würzburg, 2020.

[25] S. S. Pershoguba and V. M. Yakovenko, "Spin-polarized tunneling current through a thin film of a topological insulator in a parallel magnetic field," *Physical Review B*, vol. 86, no. 165404, pp. 1–5, 2012.

[26] D. Weiss, K. V. Klitzing, K. Ploog, and G. Weimann, "Magnetoresistance oscillations in a two-dimensional electron gas induced by a submicrometer periodic potential," *Europhysics Letters*, vol. 8, no. (2), pp. 179–184, 1989.

[27] T. Ihn, *Semiconductor Nanostructures: Quantum states and electronic transport*. Oxford: Oxford, 2010.

[28] J. Jo, E. A. Garcia, K. M. Abkemeier, M. B. Santos, and M. Shayegan, "Probing the subband structure of a wide electron system in a parabolic quantum well via capacitance-voltage measurements," *Physical Review B*, vol. 47, no. 7, pp. 4056–4059, 1993.

[29] S. J. Papadakis, E. P. De Poortere, M. Shayegan, and R. Winkler, "Anisotropic magnetoresistance of two-dimensional holes in GaAs," *Physical Review Letters*, vol. 84, no. 24, pp. 5592–5595, 2000.

[30] E. Tutuc, E. P. De Poortere, S. J. Papadakis, and M. Shayegan, "In-plane magnetic field-induced spin polarization and transition to insulating behavior in two-dimensional hole systems," *Physical Review Letters*, vol. 86, no. 13, pp. 2858–2861, 2001.

[31] X. C. Zhang, A. Pfeuffer-Jeschke, K. Ortner, V. Hock, H. Buhmann, C. R. Becker, and G. Landwehr, "Rashba splitting in n-type modulation-doped HgTe quantum wells with an inverted band structure," *Physical Review B*, vol. 63, no. 245305, pp. 1–8, 2001.

[32] Y. S. Gui, C. R. Becker, N. Dai, J. Liu, Z. J. Qiu, E. G. Novik, M. Schäfer, X. Z. Shu, J. H. Chu, H. Buhmann, and L. W. Molenkamp, "Giant spin-orbit splitting in a HgTe quantum well," *Physical Review B*, vol. 70, no. 115328, pp. 1–5, 2004.

[33] J. Hinz, H. Buhmann, M. Schäfer, V. Hock, C. R. Becker, and L. W. Molenkamp, "Gate control of the giant Rashba effect in HgTe quantum wells," *Semiconductor Science and Technology*, vol. 21, pp. 501–506, 2006.

[34] J. Nitta, T. Akazaki, H. Takayanagi, and T. Enoki, "Gate control of spin-orbit interaction in an inverted $In_{0.53}Ga_{0.47}As/In_{0.52}Al_{0.48}As$ heterostructure," *Physical Review Letters*, vol. 78, no. 7, pp. 1335–1338, 1997.

[35] C. M. Hu, J. Nitta, T. Akazaki, H. Takayanagi, J. Osaka, P. Pfeffer, and W. Zawadzki, "Zero-field spin splitting in an inverted $In_{0.53}Ga_{0.47}As/In_{0.52}Al_{0.48}As$ heterostructure: Band nonparabolicity influence and the subband dependence," *Physical Review B*, vol. 60, no. 11, pp. 7736–7739, 1999.

[36] R. Winkler, "Rashba spin splitting in two-dimensional electron and hole systems," *Physical Review B*, vol. 62, no. 7, pp. 4245–4248, 2000.

[37] A. Pfeuffer-Jeschke, *Bandstruktur und Landau-Niveaus quecksilberhaltiger II-VI Heterostrukturen*. PhD thesis, Universität Würzburg, 2000.

[38] X. C. Zhang, K. Ortner, A. Pfeuffer-Jeschke, C. R. Becker, and G. Landwehr, "Effective g factor of n-type $HgTe/Hg_{1-x}Cd_xTe$ single quantum wells," *Physical Review B*, vol. 69, no. 115340, pp. 1–7, 2004.

[39] M. König, S. Wiedmann, C. Brüne, A. Roth, H. Buhmann, L. W. Molenkamp, X.-l. Qi, and S.-c. Zhang, "Quantum Spin Hall Insulator State in HgTe Quantum Wells," *Science*, vol. 318, no. 5851, pp. 766–771, 2007.

5

Summary

Nature shows us only the tail of the lion. But I have no doubt that the lion belongs with it even if he cannot reveal himself all at once.

Albert Einstein

In my dissertation, I addressed the question of whether the 3D topological insulator mercury telluride (3D TI HgTe) is a suitable material for spintronics applications. This question was addressed by investigating the SOTs generated by the 3D TI HgTe in an adjacent ferromagnet (Permalloy) by using the ferromagnetic resonance technique (SOT-FMR).

In the first part of the dissertation, the reader was introduced to the mathematical description of the SOTs of a hybrid system consisting of a topological insulator (TI) and a ferromagnet (FM). Furthermore, the sample preparation and the measurement setup for the SOT-FMR measurements were discussed. Our SOT-FMR measurements showed that at low temperatures ($T = 4.2$ K) the out-of-plane component of the torque is dominant. At room temperature, both in-plane and out-of-plane components of the torque could be observed. From the symmetry of the mixing voltage (Figs. 3.14 and 3.15) we could conclude that the 3D TI HgTe may be efficient for the generation of spin torques in the permalloy [1]. The investigations reported here showed that the SOT efficiencies generated by the 3D TI HgTe are comparable with other existent topological insulators (see Fig. 3.17). We also discussed in detail the parasitic effects (such as thermovoltages) that can contribute to the correct interpretation of the spin torque efficiencies.

Although the results reported here provide several indications that the 3D TI HgTe might be

efficient in exerting spin-torques in adjacent ferromagnets [2], the reader was repeatedly made aware that parasitic effects might contaminate the correct writing and reading of the information in the ferromagnet. These effects should be taken into consideration when interpreting results in the published literature claiming high spin-orbit torque efficiencies [2–4].

The drawbacks of the SOT-FMR measurement method led to a further development of our measurement concept, in which the ferromagnet on top of the 3D TI HgTe was replaced by a spin-valve structure. In contrast with our measurements, in this measurement setup, the current flowing through the HgTe is known and changes in the spin-valve resistance can be read via the GMR effect.

Moreover, the SOT-FMR experiments required the application of an in-plane magnetic field up to 300 mT to define the magnetization direction in the ferromagnet. Motivated by this fact, we investigated the influence of an in-plane magnetic field in the magnetoresistance of the 3D TI HgTe. The surprising results of these measurements are described in the second part of the dissertation. Although the TI studied here is non-magnetic, its transversal MR (R_{xy}) showed an oscillating behavior that depended on the angle ϕ between the in-plane magnetic field and the electrical current. This effect is a typical property of ferromagnetic materials and is called planar Hall effect (PHE) [5, 6]. Moreover, it was also shown that the PHE amplitude (R_{xy}) and the longitudinal resistance (R_{xx}) oscillate as a function of the in-plane magnetic field amplitude for a wide range of carrier densities of the topological insulator.

The PHE was already described in another TI material ($Bi_{2-x}Sb_xTe_3$) [7]. The authors suggested as a possible mechanism the scattering of the electron off impurities that are polarized by an in-plane magnetic field. We critically discussed this and other theoretical proposed mechanisms existent in the literature [8, 9].

In this thesis, we attempted to explain the origin of the PHE in the 3D TI HgTe by anisotropies in the band structure of this material. The $\vec{k} \cdot \vec{p}$ calculations based on 6-orbitals were able to demonstrate that an interplay between Rashba, Dresselhaus, and in-plane magnetic field deforms the Fermi contours of the camel back band of the 3D TI HgTe, which could lead to anisotropies in its conductivity. However, the magnetic fields needed to experimentally observe this effect are as high as 40 T, i.e., one order of magnitude higher than reported in our experiments. Additionally, calculations of the DoS to assess if there is a difference in the states for $B_{in} \parallel I$ and $B_{in} \perp I$ were, so far, inconclusive. Moreover, the complicated dependence of Rashba in the p-conducting regime of HgTe [10] makes it not straightforward the inclusion of this term in the band structure calculations.

Despite the extensive efforts to understand the origin of the galvanomagnetic effects in the 3D TI HgTe, we could not determine a clear mechanism for the origin of the PHE and the MR oscillations studied in this thesis. However, our work clarifies and excludes a few mechanisms

reported in the literature as the origin of these effects in the 3D TI HgTe. The major challenge, which still needs to be overcome, is to find a model that *simultaneously* explains the PHE, the gate dependence, and the oscillations in the magnetoresistance of the 3D TI HgTe as a function of the in-plane magnetic field.

To conclude, the author would like to express her hope to have brought the reader closer to the complexity of the questions addressed in this thesis and to have initiated them into the art of *properly* conducting electrical transport measurements on topological insulators with in-plane magnetic fields.

References

[1] P. B. Ndiaye, C. A. Akosa, M. H. Fischer, A. Vaezi, E. A. Kim, and A. Manchon, "Dirac spin-orbit torques and charge pumping at the surface of topological insulators," *Physical Review B*, vol. 96, no. 014408, pp. 1–8, 2017.

[2] Y. Wang, R. Ramaswamy, and H. Yang, "FMR-related phenomena in spintronic devices," *Journal of Physics D: Applied Physics*, vol. 51, jun 2018.

[3] A. R. Mellnik, J. S. Lee, A. Richardella, J. L. Grab, P. J. Mintun, M. H. Fischer, A. Vaezi, A. Manchon, E. A. Kim, N. Samarth, and D. C. Ralph, "Spin-transfer torque generated by a topological insulator," *Nature*, vol. 511, pp. 449–451, 2014.

[4] A. Manchon, J. Železný, I. M. Miron, T. Jungwirth, J. Sinova, A. Thiaville, K. Garello, and P. Gambardella, "Current-induced spin-orbit torques in ferromagnetic and antiferromagnetic systems," *Reviews of Modern Physics*, vol. 91, no. 035004, 2019.

[5] C. Goldberg and R. E. Davis, "New galvanomagnetic effect," *Physical Review*, vol. 94, no. 5, pp. 1121–1125, 1954.

[6] J. P. Jan, *Solid State Physics, Vol. 5.* Academic Press Inc., New York, 1957.

[7] A. A. Taskin, H. F. Legg, F. Yang, S. Sasaki, Y. Kanai, K. Matsumoto, A. Rosch, and Y. Ando, "Planar Hall effect from the surface of topological insulators," *Nature Communications*, vol. 8, no. 1340, pp. 1–7, 2017.

[8] S. Nandy, A. Taraphder, and S. Tewari, "Berry phase theory of planar Hall effect in topological insulators," *Scientific Reports*, vol. 8, no. 14983, pp. 1–9, 2018.

[9] S.-H. Zheng, H.-J. Duan, J.-K. Wang, J.-Y. Li, M.-X. Deng, and R.-Q. Wang, "Origin of planar Hall effect on the surface of topological insulators: Tilt of Dirac cone by an in-plane magnetic field," *Physical Review B*, vol. 101, pp. 1–6, jan 2020.

[10] X. C. Zhang, K. Ortner, A. Pfeuffer-Jeschke, C. R. Becker, and G. Landwehr, "Effective g factor of n-type $HgTe/Hg_{1-x}Cd_xTe$ single quantum wells," *Physical Review B*, vol. 69, no. 115340, pp. 1–7, 2004.

6

Zusammenfassung

In meiner Dissertation beschäftigte ich mich mit der Frage, ob der 3D topologische Isolator Quecksilbertellurid (3D TI HgTe) ein geeignetes Material für Spintronik-Anwendungen ist. Wir untersuchten Spin-Bahn-Drehmomente, die auf Elektronen beim Tunneln zwischen HgTe und einem angrenzenden Ferromagneten (Permalloy) einwirken. Zunächst setzten wir die Methode der Ferromagnetresonanz (SOT-FMR) für diese Untersuchungen ein.

Im ersten Teil der Dissertation werden die Leser in die mathematische Beschreibung von Spin-Bahn-Drehmomenten in einem Hybridsystem bestehend aus topologischem Isolator (TI) und Ferromagnet (FM) eingeführt. Des Weiteren werden die Probenherstellung und der Messaufbau für SOT-FMR Messungen besprochen. Unsere SOT-FMR Messungen ergaben, dass bei tiefen Temperaturen ($T = 4.2$ K) die Normalkomponente (bezogen auf der TI-Oberfläche) des Drehmoments groß war. Bei Raumtemperatur konnten im Signal beide Komponenten (parallel und normal zur TI-Oberfläche) beobachtet werden. Aus der Symmetrie der Mixing-Spannung (Abbildungen 3.14 und 3.15) schlossen wir, dass 3D TI HgTe ein Spin-Bahn-Drehmoment auf das Elektronensystem des Permalloys überträgt. Unsere Untersuchungen zeigten darüber hinaus, dass die Effizienz dieser Übertragung mit der anderer vorhandener topologischen Isolatoren vergleichbar ist (siehe Abb. 3.17). Abschließend wurden parasitäre Effekte bei der Abschätzung des Spin-Bahn-Drehmoments bzw. andere Interpretationen des Messsignals und seiner Komponenten (z.B., Thermospannungen) ausführlich diskutiert.

Obwohl die hier gezeigten Ergebnisse vermehrt darauf hinweisen, dass der 3D TI HgTe möglicherweise effizient für die Anwendung von Spin-Drehmomenten in angrezenden Ferromagneten ist [1], wird dem Leser weiderholt klargemacht, dass parasitäre Effekte eventuelle das korrekte Schreiben und Lesen der Information in Ferromagneten verunreignigt. Diese sollten auch bei der Interpretation von publizierten Resultaten besonders hohen Spin-Bahn-Drehmomentübertragungen in

der Literatur berücksichtigt werden [1–3].

Die Nachteile der SOT-FMR-Messmethode führten zu einer Weiterentwicklung unseres Messkonzepts, bei dem der Ferromagnet durch eine Spin-Valve-Struktur ersetzt wurde. In dieser Messanordnung ist der Stromfluss durch den 3D TI im Gegensatz zu den vorangegangenen Messungen bekannt und die Widerstandsänderung der Spin-Valve-Struktur kann durch den GMR-Effekt ausgelesen werden.

Die Ausrichtung der Magnetisierung des Ferromagneten in den SOT-FMR-Experimenten erforderte es, ein magnetisches Feld von bis zu 300 mT parallel zur TI-Oberfläche anzulegen. Motiviert durch diesen Umstand, untersuchten wir den Einfluss eines parallelen Magnetfelds auf den Magnetowiderstand in 3D TI HgTe. Die überraschenden Resultate dieser Messungen werden im zweiten Teil der Dissertation beschrieben. Obwohl nichtmagnetisches Quecksilbertellurid untersucht wurde, oszillierte der transversale Magnetowiderstand (R_{xy}) mit dem Winkel ϕ zwischen der Magnetfeldrichtung (parallel zur Oberfläche) und der elektrischen Stromflussrichtung im topologischen Isolator. Dieser Effekt ist eine typische Eigenschaft von ferromagnetischen Materialien und wird planarer Hall-Effekt (PHE) genannt[4, 5]. Magnetowiderstands- (MR-)Oszillationen wurden ebenfalls sowohl im Längswiderstand (R_{xx}) und im transversalen Widerstand (R_{xy}) über einen weiten Bereich von magnetischen Feldstärken und Ladungsträgerdichten des topologischen Isolators beobachtet. Der PHE wurde bereits zuvor in einem anderen TI-Material ($Bi_{2-x}Sb_xTe_3$) beschrieben [6]. Als physikalischer Mechanismus wurde von den Autoren Elektronenstreuung an magnetisch polarisierten Streuzentren vorgeschlagen. Wir diskutierten sowohl diesen Erklärungsansatz als auch andere Theorievorschläge in der Literatur [7, 8] kritisch.

In dieser Doktorarbeit haben wir versucht, der PHE des 3D TI HgTe durch die Asymmetrie in der Bandstruktur dieses Materials zu erklären. In $\vec{k} \cdot \vec{p}$- Bandstrukturrechnungen mit einer 6-Orbital-Basis zeigten wir, dass das Zwischenspiel von Rashba- und Dresselhaus-Spin-Bahn-Wechselwirkung mit dem magnetischen Feld parallel zur TI-Oberfläche zu einer Verformung der Fermikontur des Valenzbands von 3D TI-HgTe führt, welche ihrerseits eine Anisotropie des Leitfähigkeit bedingt. Die benötigten Magnetfeldstärken in diesem Modell waren mit bis zu 40 T jedoch etwa eine Größenordnung größer als jene in unseren Experimenten. Des Weiteren lieferte eine direkte Berechnung der Zustandsdichten für $B_{in} \parallel I$ und $B_{in} \perp I$ bisher keine klaren Resultate. Die komplizierte Abhängigkeit der Rashba-Spin-Bahn-Kopplung für p-leitendes HgTe [9] machte es außerdem schwierig, diesen Term in die Bandstrukturrechnung zu inkludieren.

Trotz umfangreicher Bemühungen, den Ursprung der galvanomagnetischen Effekte im 3D TI HgTe zu verstehen, konnte in dieser Arbeit der Mechanismus des PHE und der MR-Oszillationen nicht eindeutig bestimmt werden. Es gelang jedoch, einige aus der Literatur bekannte Theorien für den PHE und die MR-Oszillationseffekte in topologischen Isolatoren auszuschließen. Die Herausforderung, eine vollständige theoretische Beschreibung zu entwickeln, die allen experimentellen Aspekten (PHE, Gatespannungsabhängigkeit und MR-Oszillationen) gerecht wird, bleibt weiter

bestehen. Abschließend möchte die Autorin ihre Hoffnung ausdrücken, den Lesern die Komplexität der Fragestellung näher gebracht zu haben und sie in die Kunst elektrischer Messungen an topologischen Isolatoren bei angelegtem parallelem Magnetfeld initiiert zu haben.

References

[1] Y. Wang, R. Ramaswamy, and H. Yang, "FMR-related phenomena in spintronic devices," *Journal of Physics D: Applied Physics*, vol. 51, jun 2018.

[2] A. R. Mellnik, J. S. Lee, A. Richardella, J. L. Grab, P. J. Mintun, M. H. Fischer, A. Vaezi, A. Manchon, E. A. Kim, N. Samarth, and D. C. Ralph, "Spin-transfer torque generated by a topological insulator," *Nature*, vol. 511, pp. 449–451, 2014.

[3] A. Manchon, J. Železný, I. M. Miron, T. Jungwirth, J. Sinova, A. Thiaville, K. Garello, and P. Gambardella, "Current-induced spin-orbit torques in ferromagnetic and antiferromagnetic systems," *Reviews of Modern Physics*, vol. 91, no. 035004, 2019.

[4] C. Goldberg and R. E. Davis, "New galvanomagnetic effect," *Physical Review*, vol. 94, no. 5, pp. 1121–1125, 1954.

[5] J. P. Jan, *Solid State Physics, Vol. 5.* Academic Press Inc., New York, 1957.

[6] A. A. Taskin, H. F. Legg, F. Yang, S. Sasaki, Y. Kanai, K. Matsumoto, A. Rosch, and Y. Ando, "Planar Hall effect from the surface of topological insulators," *Nature Communications*, vol. 8, no. 1340, pp. 1–7, 2017.

[7] S. Nandy, A. Taraphder, and S. Tewari, "Berry phase theory of planar Hall effect in topological insulators," *Scientific Reports*, vol. 8, no. 14983, pp. 1–9, 2018.

[8] S.-H. Zheng, H.-J. Duan, J.-K. Wang, J.-Y. Li, M.-X. Deng, and R.-Q. Wang, "Origin of planar Hall effect on the surface of topological insulators: Tilt of Dirac cone by an in-plane magnetic field," *Physical Review B*, vol. 101, pp. 1–6, jan 2020.

[9] X. C. Zhang, K. Ortner, A. Pfeuffer-Jeschke, C. R. Becker, and G. Landwehr, "Effective g factor of n-type HgTe/$Hg_{1-x}Cd_xTe$ single quantum wells," *Physical Review B*, vol. 69, no. 115340, pp. 1–7, 2004.

Appendix

A

Recipe for SOT-FMR devices

Mesa

- cleaving:
  Minimum size of sample: (3 × 3) mm^2
  Maximum size of sample: (4.5 × 4.5) mm^2
- cleaning: 5 min in Acetone in ultrasonic bath, Isopropanol, H_2O
- spin coating: ECI 3027 (20 sec., 6000 rpm), 2 min soft bake on hot plate at 80° C
- mask aligner:
  exposure time: 6 sec.
  clearance exposure with the square of Hall bar mask: 20 sec.
- development: developer AZ 726 MIF
  development time: 23 sec.
- rinse in H_2O
- check under the microscope
- Ion beam etch
- stripping:
  – 5 min in Acetone in US 37 Hz/100% at 45° C
  – 25 min in Acetone on HP at 50° C
  – Isopropanol, H_2O
  – 2 min TS P1316 in US 37 Hz/100% at 45° C

– 5 min TS P1316 on HP at 50° C
– Isopropanol, H_2O

Diffusion Barrier

- spin coating: ECI 3027 (20 sec., 6000 rpm), 2 min softbake on hot plate at 80° C
- mask aligner:
  exposure time: 6 sec.
- development: developer AZ 726 MIF, development time: 23 sec.
- rinse in H_2O
- ALD: 12 cycles (1.21 nm) of HfO at ≈ 35° C
- Lift Off: 4 min in Acetone in US 37 Hz/100%, Isopropanol, H_2O

Ferromagnet

- spin coating: ARN 4340 (20 sec., 6000 rpm), 2 min softbake on hot plate at 80° C
- mask aligner:
  exposure time: 20 sec.
- post-exposure bake: 6 min at 80° C
- development: developer AR 300-47
  development time: 30 sec.
- sputter: – 25 nm NiFe (250 sec., 50 W) – 10 nm Ru (50 sec., 50 W)
- Lift Off: 2 min in Acetone, Isopropanol, H_2O

Insulator for Gate

- spin coating: spin coating: ARN 4340 (20 sec., 6000 rpm), 2 min softbake on hot plate at 80° C
- mask aligner:
  exposure time: 20 sec.
- post-exposure bake: 6 min at 80° C
- development: developer AR 300-47
  development time: 45 sec.

- rinse in H_2O
- ALD (at $\approx 35°$ C) – 20 cycles (2 nm) of ZrO
  – 250 cycles (27.5 nm) of AlO
  – 40 cycles (4 nm) of HfO
- Lift Off: 8 min in Acetone in US 37 Hz/100%, Isopropanol, H_2O

Metallization of waveguides and HB contacts

- spin coating: ARN 4340 (20 sec., 6000 rpm), 2 min softbake on hot plate at 80° C
- mask aligner: exposure time: 20 sec.
- post-exposure bake: 6 min at 80° C
- development: developer AR 300-47
  development time: 30 sec.
- metallization: – 60 nm of AuGe
  – 120 nm of Au
- Lift Off: 5 min in Acetone and squeezing, Isopropanol, H_2O
- glue sample into the sample holder with PMMA 950K 5%

Acknowledgements

The completion of this thesis would not have been possible without the support of many people.

First, I would like to thank Prof. Dr. Laurens Molenkamp for the unique opportunity to work in EP3! Laurens, you built a paradise for any physicist doing transport measurements and I am very proud and grateful you gave me the opportunity to have been part of your group! Moreover, thanks for your understanding in the hard times, for signing tons of documents in Portuguese (!!) and for always being open for discussions!

Prof. Dr. Charles Gould for the supervision of my Ph.D. projects, for the discussions and for the support concerning any paperwork related to my visa and grant renewal.

Dr. Erwann Bocquillon for the supervision of my first Ph.D. year. Erwann, your motivation, honesty and expertise are inspiring and I am glad I had the opportunity to work with you. It was short but very rewarding! Moreover, thanks for correcting the FMR chapter of this thesis so promptly! I wish you and Ramla a bright time together in France!

Dr. Hartmut Buhmann for the expertise in topological insulators, transport measurements and openness in discussing physics. Hartmut, thanks for your support during the several dilemmas in making a Ph.D. and for the physics discussions!

Dr. Saquib Shamin for his patience and expertise in guiding me into cooling my first dilution refrigerator. Thank you for the several nights and weekends that you were selflessly available for helping me troubleshooting problems with the fridge and for reading and correcting parts of my thesis! Moreover, thanks for building and keeping a positive atmosphere in our group! I wish you all the best in your endeavors!

Dr. Wouter Beugeling, not only for the infinite patience in helping me to deal with calculations in Matlab but also for making the "kdotpi" program accessible for everyone in our group. Moreover, thanks for the thorough corrections of the theoretical part of this thesis and for always helping me to improve my texts! Wouter, I am very glad you joined our chair - I guess this makes you almost an experimentalist now, oder?

Dr. Oleksiy Kashuba for the intense physics discussions fuelled with coffee. Alex, thanks for all the patience in discussing "all those calculations" with me, for never laughing at my questions and, moreover, for bringing your precious dark humor to every discussion! I am truly going to

miss you! I wish you the best of success with your robots and the beautiful twins!

To the team of collaborators in the theory department, who provided help in the understanding of several aspects of my work: Prof. Dr. Björn Trauzettel, Prof. Dr. Ewelina Hankiewicz, Dr. Oleksiy Kashuba, Dr. Wouter Beugeling and Julian-Benedikt Mayer.

I also would like to thank Dr. Tanja Borzenko for helping me with optical and e-beam lithography challenges and for sharing with me her substantial experience and knowledge. Moreover, thanks for promptly driving me to the pharmacy on that terrible day, Tanja! I really appreciate it!

The devices produced in this thesis would never come to reality without the insights of Dr. Johannes Kleinlein. Whenever I faced challenges, he always offered time in his (tight) schedule to help me. Joe, thanks for your guidance and for also showing me how to properly organize my work.

Dr. Kalle Bendias, not only for the friendship and the fun moments but also for being the person introducing me to the realm of optical lithography. Thanks for being patient, for correcting my mistakes and for helping me to improve my devices and lithography recipes.

The work at the cleanroom would never have been possible without the competence, experience, expertise and dark humor of Volkmar Hock. Volkmar, you were a fundamental stone of my PhD! Thank you for keeping our cleanroom running perfectly (and safe!), for the discussions about optical lithography and for saving my fallen molyblocks into the cluster! Many thanks also go to the other members of the cleanroom staff: Petra Wolf-Müller, Carmen Bundschuh und Martin Zipf.

Many thanks also to the cryogenics team, Roland Ebert and Cornelius Zigga! Thank you for the friendly conversations and for allowing me the possibility to learn from you! Roland, thanks for also showing me how a proper work calendar should look like! I will start mine soon! Cornelius, thanks for teaching me new words in German and for always giving me a full Helium can for Sunday afternoon refills! I wish you all the best for you and your beloved family!

A big thanks to the mechanical and electrical workshop teams for promptly providing me with the help I needed for my setups.

Dr. Claus Schumacher, for making sure we all work safe, for helping me with sw-related issues, for guiding me into German bureaucracy and for having a delightful dry humor!

Niklas Krainovic and Jan Donges for their contribution to the SOT project as bachelor students.

Konstantin Martin, for all the help with Matlab, measurements, and for the physics and life-related discussions.

Prof. Dr. Grzegorz Karczewski, for always being open to discuss physics and for being the reason I went often for dinner with the MBE team.

Dr. Tobias Kiessling for helping me to deal with any trouble related to university and visa paperwork.

Dr. Martin Stehno, for the physics discussions and for the great walks back home where we discussed every kind of subject! Moreover, thanks for helping me with the Zusammenfassung section of this thesis! I will miss you!

Dr. Evaldo Ribeiro, my bachelor supervisor for introducing me to experimental physics and for being supportive in all my career endeavors. You are a big source of inspiration to me, Evaldo!

Thanks to the C116 office for the great atmosphere and physics discussions, initially with Jonas Wiedenmann, Simon Hartinger, Raimund Schreleth, then with Sandeep Upadhyay, Dr. Taisiia Romanova and Johannes Baumann.

The several colleagues in the Physics Faculty who were always open and ready to physics discussions and/or to offer me good coffee!

My Würzburg first family: Dr. Jonas Wiedenmann, David Mahler, Martin Baussenwein, Dr. Kalle Bendias, Dr. Phillip Leubner, Simon Hartinger, Dr. Mirko Trabel, Dr. Maximilian Kassel, Andreas Budewitz, Dr. Holger Thierschmann, Dr. Raimund Schreleth, Dr. Cornelius Thienel. When I arrived in EP3, I and Erwann were the only (young) foreigners in the group. Giving all the new challenges of moving to a new country and immersing in a new culture, the “guys”, as I call them, were simply my family here. They introduced me to every “Rebsort” in the region, every beer, every famous “Frängische” dish... Some of them invited me to spend my first Christmas away from my family with their families. Guys, you helped me to integrate, made me speak German “voluntarily”, helped me with paperwork, helped me to change my political views (thank you so much for that!!), and, most importantly, got used to my hugs every day. Wow! Time goes by very fast, but the great and crazy moments we spent together will always be deeply crafted in my heart! Thanks for being a safe harbor in the tempest that is starting a new life abroad! Thanks for taking good care of me, for being patient. If I became “Germanized” and could integrate into the German culture, it is all because of you! Ich hab euch gern!

The other members of EP3, who always helped to build and keep building a very pleasant working atmosphere: Dr. Mohamed Abdelghani (thanks for the help with measurements in the 10 T cryostat!), Jimena Siepe (thanks for reading my intro, querida!), Lena Fürst, Jan Hajer, Lukas Lunczer, Dr. Stephan Schreyeck (thanks for introducing me to Mercado Mexicano!), Eva Liebhaber, Kristina Kletzel, Diptanu Roy, Pankaj Mandal, Dr. Lixian Wang, Dr. Felicitas Brüne, Pragya Shekar, Valentin Müller (thanks for bonding my sensitive samples and for the physics

discussions, Vale!), Johannes Brehm (thanks for the introductory German cookbook and for teaching me how to bake Zwiebelkuchen - all the best in the new job!), Diptanu Roy (it seems our cooking competition will have to be in Eindhoven!), Florian Bayer, Leonid Bovkun and the other members of the AG Kiessling, Konstantin Martin, Bobby Chrisol, Alwin Antony, Dr. Luis Maier and so many others which I had the pleasure to work with.

I am also very grateful to the **Science without Borders** Brazilian scholarship program and the **Elitenetzwerk Bayern** for the financial support.

Angelika Berger, for always providing help with paperwork related to my Ph.D and also for helping me with the Zusammenfassung section of this thesis. On the personal side, thanks for your beautiful friendship which grew stronger over the years! You are a hidden treasure I am so glad that the time in Würzburg gifted me with such an amazing friend like you! I am looking forward with excitement to sharing time with you, it does not matter where we will be in the future! Ich hab dich lieb!

Marco Blam, my second husband: thanks for your support, for the beautiful bond we created, for the friendship, for being there in the good and bad times and, most importantly, for always being in the mood to have a great time together - Huttenstraße 19!!! I love you, my dear!

Rory and Merle Arrowsmith, for their beautiful and steadfast friendship! The time spent with you, either baking cookies or discussing the dichotomy between rationale and faith was precious and it felt like family! Thanks for always supporting me in my (hairpin turn) path towards Christ and for helping me do discovery that, when it comes to faith, my safe place is not on an island, but in the sea of struggle! I love you! Also, a big thanks to everyone from the Bibel Hauskreis from their support and prayers!

The great friends I met in Germany, who contributed to make this journey lighter: Anastasia Schmidt, Thomas van Dijk, Pauline Polka, Nikolai Bunzmann, Thiago Ribeiro, Carolina Attademo, Celso Fornieri, Daniel Almeida Blam, Irene da Cruz.

My beloved Dutch family, the Oostingas: Greet, Wim, Edwin, Annemieke, Marjan, Addy, Flo, Lola, Boaz and Tim, thanks for being so supportive and receiving me in your family with open arms! I am looking forward to living closer and enjoying more time together with all of you!

My lovely Brazilian family, my dad Nerveton, my mom Edna and my sister Patricia. Here, I want to mention a few things about my family: I did not come from a rich Brazilian family. My parents were very poor and we almost starved when I was a kid. My parents did not finish primary school. My dad worked in the sugarcane plantation since a young age and, many times, his payment was simply a plate of rice and beans. University was a reality very distant from us. Despite his very humble background and his lack of formal education, my father has always believed in education and has made many financial sacrifices - a terrible burden in a 3rd world

country - so that I and my sister could study. That is why finishing my Ph.D. and becoming the first doctor in my family feels not only like a victory to me but to my parents and sister! I am very proud of where I came from and also very proud of my parents for understanding the value of education, despite not having had the opportunity to one. Pai, mãe, bocó - muito obrigada pelo apoio, por correrem com burocracia enquanto eu estava aqui, pelo carinho, preocupação e compreensão durante todos esses anos que eu estou longe de casa. Sosseguem o coração. As asas que vocês me deram pra voar me ajudaram a entender que o mundo é meu lar! Papito, muito obrigada por seu apoio e sacrifícios, por sempre acreditar que eu poderia chegar lá. Só de imaginar por tudo o que você passou e que eu, finalmente, serei uma doutora enche meu coração de alegria que eu posso te dar esse orgulho. Esse título também é seu! Eu amo vocês!

I also would like to acknowledge a few sources of continuous inspiration during my Ph.D.: Michael Foley, thanks for, through "The age of absurdity", helping me to understand that "the Simorgh is *me*"! Ibrahim Maalouf, thanks for the great "Kalthoum" album! I could always concentrate and find joy in my work while listening to your music. I hope to see you again soon! The Bony King of Nowhere, thanks for making "Going Out" - I could always resonate with this song at the end of my Ph.D.! Snarky Puppy, thanks for creating "Gretel", a song as robust as spin-momentum locking! Sixto Rodriguez, for creating "Cause" - it accompanied me in many good and bad moments of my Ph.D.

Finally, Jeroen Oostinga, for being the "rock upon which I stand", my safe harbor, my home. Thanks for your support in good and bad times, dedication to our long-distance relationship, for pretending interest in my thesis (hahaha) and for teaching me how amazing is to share life with someone who complements you! I am looking forward to our bright future in The Netherlands with excitement and joy! Ik hou van jou!

"This is the existentialist triumph, the preservation of a secret self and personal freedom by rendering Caesar only the things that are Caeser's"

Michael Foley